

MAGNETIC PROPERTIES OF COBALT NANOSTRUCTURES GROWN USING POROUS ANODIC ALUMINA MEMBRANE

Thesis

Submitted in partial fulfilment of the requirements for the degree of
DOCTOR OF PHILOSOPHY

by

BOOMINATHASELLARAJAN S.



**DEPARTMENT OF PHYSICS
NATIONAL INSTITUTE OF TECHNOLOGY KARNATAKA
SURATHKAL, MANGALORE -575025**

May, 2016

DECLARATION

by the Ph.D. Research Scholar

I hereby *declare* that the Research Thesis entitled “**Magnetic Properties of Cobalt Nanostructures Grown Using Porous Anodic Alumina Membrane**” which is being submitted to the National Institute of Technology Karnataka, Surathkal in partial fulfilment of the requirements for the award of the Degree of Doctor of Philosophy in Physics is a *bonafide report of the research work carried out by me*. The material contained in this Research Thesis has not been submitted to any University or Institution for the award of any degree.

Boominathasellarajan S.

(Register Number: 123008PH12P01)

Department of Physics

Place: NITK-Surathkal

Date:

CERTIFICATE

This is to *certify* that the Research Thesis entitled “**Magnetic Properties of Cobalt Nanostructures Grown Using Porous Anodic Alumina Membrane**” submitted by Boominatha sellarajan S. (Register Number: 123008PH12P01) as the record of the research work carried out by him, is *accepted as the Research Thesis submission* in partial fulfilment of the requirements for the award of degree of Doctor of Philosophy.

Research Guide(s)

Dr. H. S. Nagaraja
Assistant Professor,
Dept of Physics,
NITK, Surathkal.
Date:

Dr. Prasanta Chowdhury
Senior Scientist,
Surface Engineering Division,
CSIR-NAL, Bangalore
Date:

Chairman – DRPC

Prof. H. D. Shashikala
Professor and Head of the Department
(Signature with Date and Seal)

*** ... *To My Beloved Family* ... ***

--- *** ---

Who Love ...me... ***Mother***

Who Actuate ...me... ***Father***

Who Consecrate ...me... ***Grand Parent's***

Who Fascinate ...me... ***Sister's***

Who Encourage ...me... ***Brother-in-law's***

Who Need ...me... ***Niece's, Nephew, and Son***

Who I'm in Love ... ***Wife***

--- *** ---

ACKNOWLEDGEMENTS

I knew that I am remembering people who grab me into this level in my life!

I begin with my parents, Amutha & Sellakumar for their affection, love and keenness towards my ambitions.

I would like to thank Dr. Prasanta Chowdhury, my supervisor, for his many suggestions and constant support during this research.

I am also thankful to Dr. Gargi Raina for her guidance through the early years of chaos and confusion.

I express my sincere gratitude to Assistant Professor Dr. H. S. Nagaraja to his interest towards my work and support, to enroll my Doctoral Degree at Department of Physics in National Institute of Technology Karnataka (NITK), Surathkal, India.

I should also mention that the financial support assisted by the Council of Scientific and Industrial Research (CSIR) through Senior Research Fellowship (SRF) for the period of 2012-2015, is crucial to the successful completion of Ph.D.

I am very grateful and sincerely thank Shri. Shyam Chetty, Director National Aerospace Laboratories (NAL-CSIR), Bangalore for the support to carry out my research work at Surface Engineering Division (SED) and to utilize their facilities throughout the work.

I express my sincere gratitude to Prof. Swapan Bhattacharya, Director, National Institute of Technology Karnataka (NITK), Surathkal, India, for the support of my doctoral degree registration in Department of Physics.

I am very grateful and sincerely thank Head of the Department Dr. Bharathibai J. Basu (time of registration), Dr. C. Anandan (time of submission), Dr. Harish C. Barshilia (time of viva-voce), at SED, NAL (CSIR), Bangalore, and Prof. N. K. Udayashankar (time of registration) and Prof. Shashikala (time of submission) at Department of Physics, NITK, Surathkal for the support till the completion of my work.

Mr. Selvakumar and Dr. Deepthi share with me their knowledge of convex analysis and provided many useful references and friendly encouragement.

I sincerely thank Mr. Siju (for FESEM), Mr. Praveen (for scanning probe), Mr. Srinivas (for XRD and technical assistance) and Mr. Jaheer Khan (for vacuum techniques) in SED, NAL-CSIR for their valuable support.

Acknowledgements

I am thankful to all my Professors and ex- and present research scholars and technical staffs of the department of Physics in NITK, Surathkal for their valuable support.

I should also mention that friends, teachers, and relatives, who supported me during graduate studies in Tamilnadu to encourage my Research attitude to bring into the present situation.

Of course, I am grateful to my parents for their patience and *love*. Without them, this work would never have come into existence (literally).

Finally, I wish to thank the following: Murali Krishnan, Prabhanjan Dilip Kulkarni (for his friendship and help me a lot in magnetic characterizations and micromagnetic simulations); Nischita (for changing my life from worse to bad); Gopi, Saravanan, Prabhu, Suresh and Tejpal... (for the remembrance in the art of football); Mohan, Yoganandan, Rajaguru, Jothi ... (for their friendship), Manoj and Arun (for helping room issues.. roommate and friends), Shashidhara, Soumalya Bhattacharya, Manepalli Raveendra Kiran, Kiran Pedanaboyina, Hidayath Ulla, Shourie Ranjana, Subhashini, Sreejesh, Bindu, Venkateshwara Rao, Santhosh, Vinay, Santhosh, Nivish, Praveen malik and other friends at NITK for the support during the residential period, Senthilnathan, Rajeshkumar, Naveen Kumar Reddy, Sakthi swarrup, Mangaiyarkarasi, Sasikala (for all the good and bad times we had together); Bhuvana my wife (for special effects); my mother Amutha-The Rolling Stones (and she know why); *and* my family members and *kids* (because I am here for them).

I remain thankful to all those who helped me directly/indirectly in carrying out this work. Finally, I salute and thank the Almighty for always being with us giving us the required strength, energy, patience, knowledge, and resources which lead into *Success in Life*.

NAL-CSIR, Bangalore

Boominathasellarajan S.

May 2016

ABSTRACT

In this report, the magnetic nanostructure of Co were grown through the nanopores of Anodic aluminum oxide (AAO) template using both electrochemical and physical vapor deposition (PVD) techniques. Detailed investigations on the fabrication of highly ordered nanoporous AAO template in different electrolyte baths were presented. Ordered domain structure with pore diameter of 40 ± 5 nm was achieved in an oxalic acid electrolyte bath at a temperature of $10\text{ }^{\circ}\text{C}$ and potential of 40 V. Whereas, in H_2SO_4 electrolyte bath, the optimized pore diameter was obtained as 22 ± 4 nm while anodizing at a temperature around $3\text{ }^{\circ}\text{C}$ and at a potential of 25 V. As grown membranes were further processed to vary pore diameters without modifying the interpore separation from 40 to 100 ± 10 nm, and 22 to 45 ± 4 nm through a wet chemical route. Structural investigations revealed that Co nanowires have different crystallographic texture while growing them in different conditions: such as pore diameter of the template, the length of the nanowire, pH of the electrolyte, and electrodeposition modes. These changes in crystallographic structure in Co nanowire were reflected while studied their magnetic properties. Both of these structural and magnetic properties were then correlated with a micromagnetic simulation using OOMMF package and detailed understanding of magnetization reversal processes were presented. These studies were further extended by reducing the aspect ratio between the length to wire diameter less than unity and entered into a nanodot array regime through PVD techniques using attached ultrathin AAO membrane. The magnetic properties of fabricated both soft and hard magnetic nanodot arrays were studied and the experimental results were presented.

Keywords: Porous anodic alumina membrane, nanowires, nanorods, nanodots, magnetic anisotropy, magnetocrystalline anisotropy, magnetostatic interactions.

Contents

Chapter	Page No.
1 INTRODUCTION	1
1.1 MAGNETIC NANOSTRUCTURES AND 1D MAGNETIC Co NANOWIRE ARRAYS	1
1.2 MAGNETIC PROPERTIES OF 1D NANOWIRES	3
1.2.1 Magnetic anisotropy	3
1.2.2 Coercive magnetic field	4
1.2.3 Angular dependence of coercivity	7
1.2.3.1 Coherent rotation (C)	7
1.2.3.2 Transverse rotation (T_r)	8
1.3 SCOPES AND OBJECTIVES	9
1.4 THESIS OUTLINE	10
2 EXPERIMENTAL PARTS	11
2.1 TEMPLATE ASSISTED GROWTH OF MAGNETIC NANOSTRUC- TURES	11
2.2 SELF-ORDER HEXAGON ARRAYS OF AAO MEMBRANE	12
2.2.1 Experimental set-up for anodization	12
2.2.2 Steps followed in anodization	12
2.3 FABRICATION OF NANOSTRUCTURES	14
2.3.1 Nanowire arrays	14
2.3.1.1 Electro-deposition	14
2.3.2 Nanodot arrays	18
2.3.2.1 Physical Vapour Deposition (PVD)	18
2.4 CHARACTERIZATION TECHNIQUES	19
2.4.1 Analysis of elemental structure and composition	19
2.4.2 Surface topography	20
2.4.3 Scanning Probe Measurement	22
2.4.4 Magnetometry Studies:	22
2.4.5 Micro-magnetic simulation	23

3	FABRICATION OF POROUS ALUMINA MEMBRANE: OPTIMUM CONDITIONS FOR SELF-ORDERED PORES	25
3.1	SELF-ORDERED POROUS ALUMINA MEMBRANE	25
3.1.1	Anodization of Al	25
3.1.2	Electro-chemical mechanism of pore formation	27
3.2	ANODIZATION CONDITIONS	28
3.2.1	Effect of applied Potential	29
3.2.2	Effect of bath Temperature	31
3.3	PORE PARAMETERS	32
3.3.1	Pore diameter (D_p) and inter-pore distance (I_p)	32
3.3.2	Porosity	34
3.3.3	Pore Growth Kinetics	35
3.4	FAST FOURIER TRANSFORM (FFT) BASED ANALYSIS OF PORE REGULARITY	37
3.4.1	Effect of anodization potential	38
3.4.2	Effect of Temperature	40
3.5	SURFACE ROUGHNESS OF SELF-ORDERED POROUS AAO MEMBRANE	42
3.6	BARRIER LAYER REMOVAL AND TUNING THE PORE WALL THICKNESS	45
3.7	ANODIZATION UNDER OXALIC ACID BATH	45
3.7.1	Optimum conditions and discussions	46
3.8	SUMMARY	48
4	FABRICATION, STRUCTURAL AND MAGNETIC PROPERTIES OF COBALT NANOWIRE ARRAYS	49
4.1	MAGNETIC Co NANOWIRE ARRAYS	49
4.2	MECHANISM OF Co DEPOSITION INSIDE NANOPOROUS MEMBRANE	53
4.3	PULSE DEPOSITION	55
4.3.1	Magnetic properties as a function of nanowire length	56
4.3.1.1	Magnetic properties of bilayer crystalline texture of Co hcp (002) and hcp (100) structures	58
4.3.1.2	Angular dependence of magnetic coercivity based re-magnetization process in bi-layered Co nanowire arrays	58
4.3.2	Magnetic properties as a function of nanowire diameter	61
4.3.2.1	Effective magnetic anisotropy	63

4.4	CONTINUOUS DEPOSITION	66
4.4.1	Effect of magnetostatic interaction in hcp Co (002) phase	66
4.4.1.1	Magnetic properties as a function of nanowire geometry (both inter-wire separation and diameter)	67
4.5	SUMMARY	73
5	PREPARATION AND MAGNETIC PROPERTIES OF NANODOT ARRAYS	75
5.1	SURFACE PATTERNING OF MAGNETIC NANODOT ARRAYS	75
5.2	CONDITION OPTIMIZATION OF UTAM	77
5.3	FABRICATION OF NANODOT ARRAYS VIA SPUTTERING TECHNIQUE	78
5.3.1	Co ₉₀ Fe ₁₀ Nanodot arrays	78
5.3.2	Magnetic properties of NanoDot arrays	79
5.3.2.1	Vibrating sample magnetometry	79
5.3.3	First order reversal curve (FORC)	82
5.4	SmCo ₅ NANODOT ARRAYS	84
5.4.1	Surface Morphology	85
5.4.2	Magnetic properties of SmCo nanoDot arrays	86
5.4.2.1	Vibrating sample magnetometry	86
5.4.2.2	Magnetic force microscopy	87
5.5	Summary	89
6	MICROMAGNETIC MODELING OF MAGNETIZATION REVERSAL IN MAGNETIC CO NANOWIRES	91
6.1	MICROMAGNETISM	91
6.2	BACKGROUND THEORY:	92
6.3	MAGNETO-CRYSTALLINE ANISOTROPY	95
6.3.1	Effect of crystalline phases in Co Nanowires	96
6.3.2	Magnetic domain structure of hcp Co (002) phase	96
6.3.2.1	Angular variation of H_{ext}	98
6.3.3	Magnetic domain structure of hcp Co (100) phase	99
6.4	COMPARISON WITH EXPERIMENTAL RESULTS	100
6.4.1	Mixed state with both hcp (002) and hcp (100)	100
6.4.1.1	Energy density contributions	103
6.4.2	Magnetic domain structure of fcc Co (111) phase	104

6.4.2.1	External magnetic field applied perpendicular to nanorod axis	106
6.4.2.2	External magnetic field applied parallel to nanorod axis	109
6.5	SIZE DEPENDENT STUDY ON MAGNETOSTATIC INTERACTION IN hcp (002) PHASE	112
6.5.1	Effect of inter-wire spacing	114
6.5.2	Effect of filling factor in array of nanowires	115
6.6	SUMMARY	116
7	CONCLUSIONS	119
7.1	FUTURE DIRECTIONS	120
	References	121

*

Abbreviations

<i>AAO</i>	<i>Anodic Aluminum Membrane,</i>
<i>Al</i>	<i>Aluminum,</i>
<i>AFM</i>	<i>Atomic Force Microscopy,</i>
<i>bcc</i>	<i>Body center cubic,</i>
<i>Co</i>	<i>Cobalt,</i>
<i>EDS</i>	<i>Energy Dispersive Spectroscopy,</i>
<i>Fe</i>	<i>Iron,</i>
<i>FESEM</i>	<i>Field Emission Scanning Electron Microscopy,</i>
<i>FWHM</i>	<i>Full width half maximum,</i>
<i>fcc</i>	<i>Face center cubic,</i>
<i>hcp</i>	<i>Hexagonal close packed,</i>
<i>MFM</i>	<i>Magnetic Force Microscopy,</i>
<i>OOMMF</i>	<i>Object Oriented Micromagnetic Framework,</i>
<i>NA</i>	<i>Numerical aperture,</i>
<i>Ni</i>	<i>Nickel,</i>
<i>NDs</i>	<i>Nanodots,</i>
<i>nN</i>	<i>nanonewton,</i>
<i>NSs</i>	<i>Nanostructures,</i>
<i>NTs</i>	<i>Nanotubes,</i>
<i>NWs</i>	<i>Nanowires,</i>
<i>Para</i>	<i>Parallel to nanowire axis,</i>
<i>Per</i>	<i>Perpendicular to nanowire axis,</i>
<i>PMMA</i>	<i>Polymethyle methacrylate,</i>
<i>SPM</i>	<i>Scanning Probe Microscopy,</i>
<i>S – W</i>	<i>Stoner – Wohlfarth,</i>
<i>UTAM</i>	<i>Ultra thin alumina membrane,</i>
<i>UHV</i>	<i>Ultra high vacuum,</i>
<i>VSM</i>	<i>Vibrating Sample Magnetometry,</i>
<i>XRD</i>	<i>X – ray diffractometry.</i>

Nomenclature

A	Exchange constant,	L_{ex}	Exchange length,
a	Inner diameter(nm),	m	Mass,
B	Temperature dependent parameter,	μm	micrometer,
C	Coherent rotation,	M_r	Remanence Magnetization (emu),
η_j	Current efficiency,	M_s	Saturation Magnetization (emu),
D	Diameter (nm),	M_r/M_s	Remanence ratio or squareness,
D_c	Critical diameter,	n	Pore density,
d_{hkl}	distance between lattice planes,	N_d	Demagnetization factor,
D_p	Pore size or diameter,	ω_t	Transverse domain wall width,
E	Electric field,	π	constant (3.14),
h	Planck constant (6.6026×10^{-34} J),	P	Porosity,
H_a	Intrinsic anisotropy field,		Parallel to nanowire axis,
H_c	Coercive field or Coercivity(Oe),	⊥	Perpendicular to nanowire axis,
H_d	Demagnetization field,	q	Geometrical parameter,
H_{dp}	Dipole interaction field,	r	Radius of the nanowire,
H_k	Effective anisotropy field,	S	Inter – wire separation (nm),
H_{ma}	Magnetocrystalline anisotropy field,	T_r	Transverse rotation,
H_n	Nucleation field,	t	Time,
I_p	Inter – pore distance/ cell size,	T	Temperature
		θ	Angle between the applied field and the nanowire axis,
j	Current density,	τ	Aspect ratio(L/D),
K_a	Magnetic anisotropy,	TC	Transition coefficient,
K_{eff}	Effective anisotropy,	t_w	Wall thickness (nm),
$K_{elastic}$	Magnetoelastic anisotropy,	V	Vortex or curling rotation,
K_{ma}	Magnetocrystalline anisotropy,	v	Velocity,
K_{shape}	Shape anisotropy,	λ	Wavelength,
L	Length (nm),	x, y, and z	Geometrical axis.

Chapter 1

INTRODUCTION

1.1 MAGNETIC NANOSTRUCTURES AND 1D MAGNETIC Co NANOWIRE ARRAYS

Magnetic nanowires, nanotubes, and nanodots are an important class of nanostructured magnetic materials. Due to size confinement in nanometer scale, individual nanoparticle shows unusual magnetic anisotropic behavior depending on their shapes and crystallographic orientations. This anisotropic behavior gets more complicated in arrays of periodic nanostructures due to the presence of magnetostatic interaction among them. Therefore, it is interesting to understand the physics behind reversal processes of nanostructured arrays with varying shape, structure and crystallographic orientation of magnetic materials. These studies are very important for their technological applications in the area of spintronics, where they have used as data storage media, nano-switching devices etc.

Nanowires, nanorods, and nanotubes have a cylindrical shape and described by three geometrical parameters: length, L , outer diameter, D and inner diameter, a . To define them in nanoscale, the value of D usually was restricted between 1 nm to 100 nm. To differentiate between nanowires and nanorods, they were classified by the value of aspect ratio ($\tau = L/D$). With $\tau > 5$, nanostructured materials were categorized as nanowires (NWs), whereas with $3 < \tau < 5$, the structures were termed as nanorods. Furthermore, nanodots (NDs) can be generalized when $\tau < 3$, i.e., 0D nanostructures. In addition to these nanostructures, the structure of nanotube is well separated from the nanowires/nanorods with the presence of cylindrical hollow core at the center. Most commonly, nanotubes (NTs) were defined by an additional parameter, wall thickness (t_w), i.e., nothing but the difference between the value of D and a . As the magnetic spins arrangement within these nanostructures is strongly influenced by their shape, it affects the magnetization reversal mechanisms and thereby overall magnetic behavior.

Two different approaches have been made to develop these nanostructures, such as top-down and bottom-up processes. Top-down approaches were performed by various lithographic techniques such as electron beam lithography, X-ray lithography, laser interference lithography, etc. In principle, it works by the etching process which reduces the size from bulk to nanometer scale. Additionally, it requires expensive and

specialized equipment. In general, the processing time and the cost are higher than the bottom-up techniques. There were two classified methods in bottom-up approach such as, dry process (i.e., includes physical vapor deposition, chemical vapor deposition, molecular beam epitaxy, pulse laser deposition, etc) and wet process (i.e., includes sol-gel, hydrothermal, electro-less and electrodeposition), respectively. Dry processes also required sophisticated equipment to grow these nanostructured materials in a gas phase environment. However, the wet process or the liquid phase methods were easy to prepare nanostructures with lower cost and for a short span of time.

Among these techniques, electrodeposition is a very simple and cost effective bottom-up technique which allows fabrication of ordered arrays of magnetic NWs, NTs and ND structures (Yin et al. 2001, Schlorb et al. 2010, Han et al. 2010). In this technique, the ordered array structure is grown through nanoporous templates such as polymer membrane (track etched polycarbonate or polyester membrane), anodic alumina membrane, porous silica membrane, etc. Recently, the template technique utilizing porous anodic Aluminum oxide (AAO) membrane was an elegant approach for the fabrication of nanostructures (see Fig. 1.1), in particular, to grow different kinds of nanowires (NWs), nanotubes (NTs) and nanodot (NDs) arrays (Henry et al. 2001, Darques et al. 2004, Franklin et al. 2007, Lei et al. 2007). The main advantages in this template approach are (Keller et al. 1953, Li et al. 1998, Masuda et al. 2002, Nielsch et al. 2002): AAO template can be fabricated with varying i) pore diameter, ii) length and iii) periodicity, by simple changing the processing parameters, such as anodizing voltage, electrolyte and electrolyte temperature. The magnetic properties of the NSs can also be tuned by varying the other parameters such as i) material, ii) crystallinity (polycrystalline, single crystal, amorphous), iii) structure (single layer, multilayer, etc), and iv) array geometry, etc. For such systems, it is important to understand how the magnetic properties depend on the fabrication parameters and thus on the geometrical and structural properties of the nanoarrays. The crystalline properties of fabricated NSs can be tuned by adjusting the electroplating conditions, such as pH, plating current, deposition time and bath

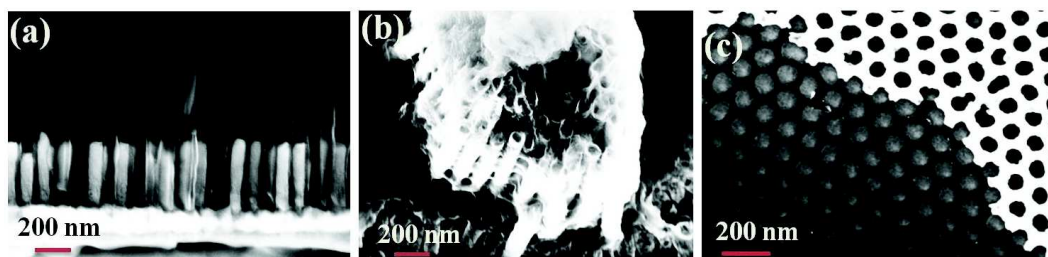


Figure 1.1: Template assisted magnetic nanostructure arrays: a) Co nanowires, b) Co nanotubes, and c) CoPt nanodot arrays, respectively.

temperature which results in arrays of NSs with different intrinsic magnetic properties.

1.2 MAGNETIC PROPERTIES OF 1D NANOWIRES

The last couple of decades, investigations on magnetic nanowire arrays (Fe, Co, Ni and their alloys) were focused on the fundamental magnetic properties such as the magnetic anisotropy (K_a), coercivity (H_c) and remanence ratio (M_r/M_s ; where M_r is the remanence (magnetization at zero fields), and M_s is the saturation magnetization of the material) as a function of both wire geometry (shape, size and the separation) and the crystalline phases (either for polycrystal or textured growth). These investigations lead to understanding the physics behind the magnetic nanowire arrays, such as domain wall motion (coherent, transverse and vortex), critical limit for switching the anisotropy (in-plane to out-of- plane or vice versa), and the magnetostatic interaction between the wires.

In 1-D nanowire system, the significant contribution in K_a comes from the shape anisotropy. Most preferable orientation of easy axis in these system lies along the wire axis for Fe (bcc), Ni (fcc) and Co (fcc), whereas in hcp Co phase, the c-axes of hcp determines the effective anisotropy, either enhancing the shape anisotropy when the hcp c-axis lies along the wire axis or compensating the shape anisotropy if it lies perpendicular to the wire axis. Other than intrinsic property (K_a), the quantification on external properties, such as H_c and M_r/M_s are mainly determined by the size and the magnetostatic interaction among the wires. However, this behavior is also determined by the intrinsic magnetic character of individual nanowires together with their magnetostatic interactions, which are related to diameter and length of nanowires and to the porosity of the membrane.

1.2.1 Magnetic anisotropy

As mentioned above, in 2-D arrays, the strong shape anisotropy of the nanowires favor longitudinal magnetic anisotropy. An analytical formula was derived to quantify the effective longitudinal anisotropy, which includes the magnetostatic interactions term arising from the dipole-dipole field (i.e., along with length (L), diameter (D), and inter-wire separation (S)), self-demagnetization term from the geometry (i.e., N_z depends on the second order term of the type $(D/L)^2$ for long axis and $N_x=1-N_z$, respectively) for shape effect, and the magnetocrystalline term from the crystalline orientation. This analytical study predicts the critical value of the nanowire length (L_c) at which a crossover of the magnetic easy axis changes from parallel to perpendicular one. Strijkers et al. (1999) was investigated the crossover phenomena for arrays of poly-crystalline Co

nanowires with $D = 100$ nm, and $S = 320$ nm, respectively and were found that it occurs at a length of $1 \mu\text{m}$. Whereas, different L_c values were reported for different materials and these values were found to be a function of both diameter and inter-wire distances (Han et al. 2002, Srivastava et al 2007). With a nanowire diameter of 45 nm and $S = 65$ nm, we observed a crossover for Co fcc(111) phase at $L_c \sim 80$ nm. The details of our observations are discussed in chapter 4 and 6.

1.2.2 Coercive magnetic field

Investigations on the values of experimental coercive field, H_c lead to distinguish the rotational modes of magnetization reversal processes in nanowires. In general, an infinitely long wire exhibits the square hysteresis loop with finite H_c value for an applied external field parallel to the wire axis, H_{ext}^{\parallel} , and $H_c = 0$ for field applied along perpendicular direction (H_{ext}^{\perp}), as shown in Fig. 1.2. Theoretically, Stoner-Wohlfarth (S-W) model (Stoner et al. 1948) has been well explained the H_c characteristics for magnetic materials with prolate spheroid ($z > x = y$) in geometry. If the ellipsoid is uniformly magnetized, then the magnetic field inside the ellipsoid depends directly on the demagnetization factor, i.e., $\vec{H}_d \sim -N_d \vec{M}$. The negative sign indicates that the self-induced H_d is opposite to the applied field and N_d is a function of the shape of the magnetic body which is expressed as $N_x + N_y + N_z = 4\pi$ (cgs unit). Moreover, analytical calculation of the demagnetization factors are related with a hypergeometric function for cylindrical nanowires in which N_z approaches 0 when $L \rightarrow \infty$ (Landeros et al. 2007, Escrig et al. 2007, Lavin et al. 2009, Sellarajan et al. 2013). Since $\vec{H}_c \sim \vec{H}_a - N \vec{M}$, this leads to the following expectation for the coercive field: $\vec{H}_c = \vec{H}_a$ when $N \rightarrow 0$, where H_a is the intrinsic anisotropy field. Therefore, a system with $D \sim L$ exhibits a finite N_z ($N_z \neq 0$) as in the case of nanowires.

However, the S-W model (Stoner et al. 1948) is assumed for coherent rotation of the magnetization for non-interacting and randomly oriented grains. These assumptions limit the use of SW model in the case of arrays of nanowires. Here, H_a is always smaller than the H_c (i.e., $H_a \ll H_c$), and this is mainly due to the presence of both magnetocrystalline anisotropy and the magnetostatic interaction among the nanowires as explained below. The magnetic properties of H_a depends on the direction of the applied field with respect to the crystal lattice. For example, Fe has a bcc structure with the highest density of atoms in the (111) direction, which leads to being the hard magnetic axis. In contrast, the atomic density is lower in (100) direction and become the easy axis (Spaldin 2011). Similarly, for fcc Ni, the (111) direction is the easy axis, and the hard axis lies along (100) direction. In the case of hcp Co, the lowest packed direction (perpendicular to the close-packed plane) is (0001) and is the easy axis, and then

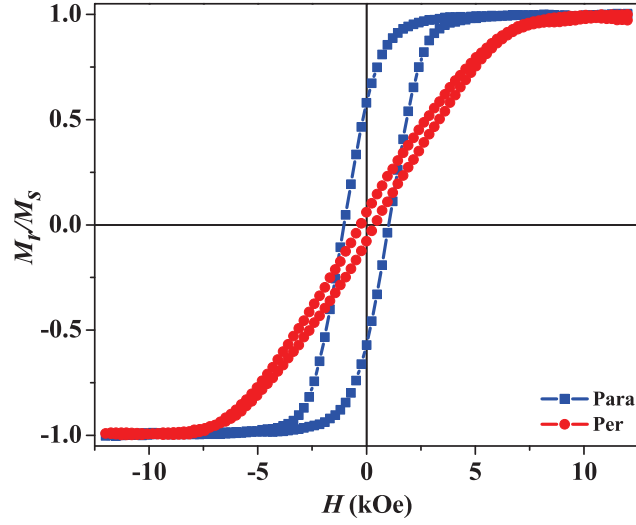


Figure 1.2: Magnetic hysteresis loops for an array of Co nanowire ($D = 70$ nm, and $L = 2$ μm) with the applied field parallel (filled square) and perpendicular (filled circle) to the wire axis.

the corresponding hard axis is the (1000) close-packed direction. On the other hand, in hcp Co, the magnetization easy axis lies along the direction of crystallographic c-axis. Therefore, in Co NWs grown with hcp (002) phase, the magnetocrystalline anisotropy enhances the longitudinal anisotropy, whereas, in the case of hcp (100), this reduces the effective anisotropy. It is to be mentioned that the one of the most anisotropic materials is the hcp structure of Co among the three transition metals. Therefore, for, Co nanowire arrays, the magnetocrystalline term, and the static interaction should be included along with the shape anisotropy in the overall anisotropy (i.e., $H_k = H_a$).

For arrays of nanowires, magnetostatic interactions among nanowires play an important role as reported in a number of previous studies. This static interaction has been derived from a simple mean field approximation theory, in which the linear dependence of the dipolar coupling on package density (P , i.e., the filling factor of the nanowires inside the membrane or the porosity of the porous membrane used) was estimated and the effective uniaxial anisotropy field for the arrays of infinite long cylinders can be expressed as (Encinas-Oropesa et al. 2001),

$$H_k = (N_x - N_z)M_s(1 - 3P) \pm H_{ma}, \quad (1.2.1)$$

where the first term on the right-hand side denotes contribution from the shape anisotropy modified by magnetostatic interactions, which depend only on the filling factor, P or density of nanowires. The filling factor to be estimated by simple porosity calculation

of the AAO membrane, that is given by (Nielsch et al. 2002):

$$P = \frac{\pi}{2\sqrt{3}} \left(\frac{D}{S}\right)^2 \quad (1.2.2)$$

where D and S are the diameters and the inter-wire separation (i.e., center-center) of the nanowires. Independently, Strijkers et al. (1999) had shown that the length of the nanowire plays an important role in defining the magnetostatic interaction term and the equation for H_k was derived as (Strijkers et al. 1999, Han et al. 2003, Ahmad et al. 2011),

$$H_k = (N_x - N_z)M_s - 6.3\pi M_s r^2 L / S^3 \pm H_{ma}, \quad (1.2.3)$$

where, r , L and S are the radius, length and the interwire separation of the wire, respectively. H_{ma} is the magnetocrystalline anisotropy field, which takes either positive or negative when the corresponding magnetization easy axis is \parallel or \perp to wire axis. With effective magnetic anisotropy field derived in Eqn. 1.2.3, H_c can be considered in both \parallel and \perp directions are (Sánchez-Barriga et al. 2009),

$$H_c^{\parallel} = \frac{2K_{eff}}{\mu_0 M_s} |\cos\theta|, \quad H_c^{\perp} = \frac{2K_{eff}}{\mu_0 M_s} |\sin\theta|, \quad (1.2.4)$$

here, $K_{eff}(= H_k M_s / 2)$ is the effective anisotropy constant of the ferromagnetic nanowires, M_s is the saturation magnetization of the magnetic material, for example, Co = 1400 emu/cc, and θ is the angle between the applied field and the anisotropy axis of the system, respectively.

Furthermore, the magnetization reversal in nanowires were discussed by the magnetization rotation, and the formation and motion of domain wall with respect to D . For the field applied parallel to wire axis, two major magnetization rotation modes were discussed. These modes were (i) homogeneous or coherent rotation, and (ii) magnetization curling. There were several reports evaluating these reversal processes with and without considering the magnetostatic interaction term. Among them, recently, Vivas et al. (2011), were evaluated the formula for K_{eff} by considering the static interaction, and can be expressed as,

$$K_{eff} = \begin{cases} K_{ma} - \frac{(1-3N_z)\mu_0 M_s^2}{2} (1-3P) & \text{if } D \leq D_c, \\ K_{ma} - \frac{N_z \mu_0 M_s^2}{2} (1-3P) + \frac{8Aq^2}{D^2 M_s} & \text{if } D \geq D_c, \end{cases} \quad (1.2.5)$$

Here, the third term of the second Eqn. 1.2.5 in the right-hand side represents the field necessary to overcome exchange force. Here, q is a geometrical parameter and is

given by the relation: $q^2 = 1.08\pi$ for a cylinder. A is the exchange stiffness constant ($A=1.3 \times 10^{-11}$ J/m for Co) and $D_c (=2q/M_s \sqrt{A/N_x})$ is the critical coherence diameter of the wire. The theoretical value of D_c was around 30 nm, whereas, experimentally this values was found to be 50 nm (Sánchez-Barriga et al. 2009, Henry et al. 2001). If $D \leq D_c$, then the exchange interaction leads to coherent rotation in nanowires. Whereas, for $D \geq D_c$, magnetostatic interactions is responsible for curling rotation. However, the presence of different magnetocrystalline anisotropy in Eqn. 1.2.5 may lead to increase or decrease the D_c value especially for Co materials.

1.2.3 Angular dependence of coercivity

The understanding of reversal mechanism is a challenge for researchers towards the application point of view, in nanowire arrays. It is to be mentioned that different magnetization reversal mechanisms would give a different angular dependence of the coercivity H_c . Theoretically, the magnetization reversal process of an NW with given anisotropy have been explained by three different modes, namely: coherent rotation (C) in which all the spins rotate simultaneously; transverse rotation (T_r) in which spins the rotation takes place via propagation of transverse domain wall; and curling or vortex rotation (V), in which spins are reversing their directions via propagation of vortex domain wall (Escrig et al. 2007, Lavin et al. 2009, Kulkarni et al. 2013).

1.2.3.1 Coherent rotation (C)

Analytical formula of each mechanism for single NW was well established through the angular dependence of the nucleation field, H_n , as this field is directly co-related with the reversal mechanism has been derived by S-W model, and can be written as (Lavin et al. 2009, Vivas et al. 2012):

$$H_n^C(\theta) = -\frac{2[K_{sh}(L) + K_{ma}]\sqrt{1-t^2+t^4}}{\mu_o M_s^2(1+t^2)} M_s. \quad (1.2.6)$$

Here $t = \tan^{1/3}(\theta)$, with θ is the angle between the field and NW cylindrical axis, M_s is the saturation magnetization, $K_{sh}(L)$ is the shape anisotropy constant and K_{ma} is magnetocrystalline anisotropy constant. Further $K_{sh}(L)$ can be written as:

$$K_{sh}(L) = \frac{1}{4} \mu_o M_s^2 [1 - 3N_z(L)], \quad (1.2.7)$$

where $N_z(L)$ is a demagnetization factor along the z-axis.

1.2.3.2 Transverse rotation (T_r)

For NWs with higher lengths, the coherent rotation is found to be energetically less favorable. In such cases, Landeros et al. (2007) proposed that the energy minimization can be achieved through a reversal mechanism via transverse mode, in which the width of domain wall, ω_T and hence the effective volume, $\pi(D/2)^2\omega_T$ reverses its magnetization by coherent rotation. Escrig et al. (2008) had then calculated the equation for nucleation field, $H_n^{T_r}$, as:

$$H_n^{T_r}(\theta) = -\frac{2[K_{sh}(\omega_T) + K_{ma}]\sqrt{1-t^2+t^4}}{\mu_o M_s^2(1+t^2)} M_s, \quad (1.2.8)$$

where

$$K_{sh}(\omega_T) = \frac{1}{4}\mu_o M_s^2[1 - 3N_z(\omega_T)], \quad (1.2.9)$$

In general, ω_T is taken to be 50 nm more than NW diameter (Lavin et al. 2007, Lavin et al. 2009). Hence, for NWs with length $L \gg \omega_T$, the reversal takes place by transverse mode, whereas in case of $L \sim \omega_T$, the coherent rotation was found to be energetically favorable. Additionally, Vivas et al. (2012) also had reported with the resultant behavior of transverse mode for large aspect ratio (> 50), without considering the NW crystallographic structure in the analytical form. In contrast to this, in this work, the experimental study of the angular dependence of H_c exhibit coherent rotation mode for hcp Co (002) with the dimension of $L=400$ nm, $D=70$ nm.

From Eqns. 1.2.6 and 1.2.8, both $H_n^C(\theta)$ and $H_n^{T_r}(\theta)$ are distinguished by the coherent reversal length, i.e., for $H_n^C(\theta)$ mode L is representing the entire length of the nanowire, whereas in $H_n^{T_r}(\theta)$ mode the coherent length (ω_T) is independent to the wire length ($H_n^{T_r} = H_n^{C(L=\omega_T)}$). Therefore, it is to be mentioned that the H_c is dependent on L and θ for coherent mode and independent to L and θ for transverse mode, respectively. Therefore, the value of H_c for both coherent and transverse mode can be expressed by the S-W model as a function of nucleation field as (Lavin et al. 2009):

$$H_c^{C(T_r)}(\theta) = \begin{cases} |H_n^C(\theta)| & 0 \leq \theta \leq \pi/4, \\ 2|H_n^{C(T_r)}(\pi/4)| - |H_n^{C(T)}(\theta)| & \pi/4 \leq \theta \leq \pi/2 \end{cases} \quad (1.2.10)$$

However, the models discussed above are used to determine the reversal the magnetization of isolated nanowires. For arrays of nanowires, the magnetostatic interaction term plays an important role along with the crystalline anisotropy energy. Therefore, the classical micromagnetic simulations are very much useful to study the role of shape anisotropy and the magnetostatic interactions in many aspects. Still, it is not fully a

closed issue and the influence of the crystalline structure has not been sufficiently addressed. Moreover, recent modifications in the analytical expressions have led into the inclusion of the magnetocrystalline anisotropy for the calculation of H_c in coherent and transverse reversal modes, it could not be useful to investigate for complicated structures of bi-layer textured or the combined different crystalline phases (multi-layered) of nanowires.

On the other hand, micromagnetic simulation provides useful information based on the understanding towards the reversal mechanism on complicated structures such as, for the bi-layered structures of different crystallographic orientations in the same material or for the different material (multi-segmented nanowires). The structure and the geometry can be designed such a way that to elucidate the reversal processes within the cylindrical nanowires / nanowire arrays. Interestingly, this leads to ruled out the applicability of the above-mentioned models for NW arrays and used to unveil the actual magnetization reversal process of our experimental nano-structures.

1.3 SCOPES AND OBJECTIVES

In this work, we were focused on the fabrication of 1D magnetic Co nanowire array with different (hcp/fcc) crystalline phases via electrodeposition processes through the pores of porous alumina membrane. Both pulse and continuous depositions under chronoamperometry condition were performed to grow different crystalline phases and textured Co nanowire arrays as a function of length and diameter. The whole thesis report deals with the understanding of the effective magnetic anisotropy of the nanowires with the presence of the crystallographic phases. In addition to this, a longitudinal magnetic anisotropy of hcp Co (002) phase is mainly used to estimate the effective magnetostatic interaction between the nanowires within denser ($\sim 3 \times 10^{10}$ no. of wires/cm²) and less denser ($\sim 1 \times 10^{10}$ no. of wires/cm²), arrays respectively. The micromagnetic simulations are utilized to reveal the magnetization reversal processes of such crystalline phases and their geometry effect using OOMMF package. Furthermore, we have investigated the properties of 0D magnetic nanodot arrays which were fabricated using physical vapor deposition technique using UTAM as shadow mask.

- Fabrication of highly ordered AAO membrane with pore diameter in the range of 25 nm to 100 nm in two-step anodization process with different electrolytes.
- Fabrication of magnetic Co nanowire arrays via electro-deposition.
- To fabricate patterned magnetic nanodot arrays on the silicon substrate through ultra thin Alumina membrane (~ 100 nm) by physical vapour deposition.

- To characterize the magnetic properties of the magnetic nanowire arrays, which will help to understand the fundamental physics behind the magneto crystalline anisotropy and shape anisotropy.
- To simulate the results using micromagnetic simulation with same geometrical parameters as observed in experiments and correlate them with both structural and magnetic data.

1.4 THESIS OUTLINE

After the detailed survey on the state of the art in magnetic nanostructure arrays (Chapter 1), we describe the experimental techniques in chapter 2, those are used throughout this work: i) Experimental setup, preparation steps on the formation of self-ordered hexagonal alumina pore arrays, ii) deposition techniques those are used to grow nanowires / nanodots using electrochemical techniques and nanodots using sputtering methods. In chapter 3, particular attention is paid on the growth optimization of ordered AAO templates in two different electrolytes; sulphuric and oxalic acids. Using these AAO templates, magnetic nanowires are grown through electrochemical routes with a variation of pH and their morphology and structural characterization are presented in Chapter 4. In this chapter, special emphasis is given on the magnetic properties of the highly ordered Co nanowire arrays as a function of length, diameter, inter-wire spacings, and crystalline phases and their co-relation with structural data. Chapter 5 deals with the surface patterning of magnetic nanodot arrays of $\text{Co}_{90}\text{Fe}_{10}$, and SmCo_5 and their magnetic properties as a function of thickness. Chapter 6 begins with the basic understanding of micromagnetic simulation and their tools to nanomagnetism. In this chapter, micromagnetic simulation data are presented for the Co nanowire arrays. In these simulation, the physical parameters of the wire i.e., diameter, length and interwire separation are taken from the experimental results. Emphasis was given to understand the magnetic reversal processes of Co nanowires including different crystalline structures, such as hcp (002), hcp (100) and fcc (111) phases, along with the shape and the magnetostatic phenomenon. In this case, the magnetostatic interaction between the neighboring wires were established by comparing the no. of wires such as; single, hexagonal arrays (i.e., a single wire positioned at the middle is surrounded by six nanowires hexagonally) of nanowires. In Chapter 7, the overall summary of the results was highlighted with justification described in the previous Chapters. Moreover, the outline of the future studies also discussed for real-time applications.

Chapter 2

EXPERIMENTAL PARTS

In this chapter, we present the details of the experimental techniques used throughout this work. Mention briefly the techniques-Electrodeposition, pulse deposition, FESEM, VSM, MFM etc.

2.1 TEMPLATE ASSISTED GROWTH OF MAGNETIC NANOSTRUCTURES

A non-lithographic approach has been used to grow magnetic nanostructures (nanowire and nanodot) array using the porous anodic alumina (AAO) membrane. The synthesis procedure of nanoporous AAO membrane involves two-step anodization process of high purity (99.99%) aluminium foils in different acidic electrolytes (Masuda et al. 1995, Masuda et al. 1997, Masuda et al. 1997, Masuda et al. 1998, Li et al. 1998, Nielsch et al. 2002, Hwang et al. 2002). The porous structures are well defined and arranged in a self-ordered regular hexagonal array with densities as high as 10^{11} pores/cm² with optimized conditions. In this case, the hexagonal arrays contain a closed-packet cells with a cylindrical central pore which are grown normal to the surface of underlying Al foil, as shown in figure 2.1. The pore size, the interspacing distance between adjacent pores and the local self-ordered domain size can be controlled by changing the anodization conditions, such as anodization potential, electrolyte, bath temperature, and the first anodization time (Masuda et al. 1995, Masuda et al. 1997, Masuda et al. 1997, Masuda et al. 1998, Li et al. 1998, Nielsch et al. 2002, Hwang et al. 2002).

Additionally, apart from the structural effects (i.e., confined by the nano-channels of the membrane), the magnetic properties of deposited Co nanowires are highly influenced by the crystalline phase (fcc/hcp) of Co while growing them, such as polycrystalline, textured, bi-layered texture. These changes in crystalline phases were obtained by tuning the electrochemical deposition conditions, i.e., mode of deposition, reduction potential, pH of the electrolyte, bath temperature, and the presence of magnetic field while deposition, etc., (Darques et al. 2004, Wang et al. 2007, Han et al. 2009, Ren et al. 2011).

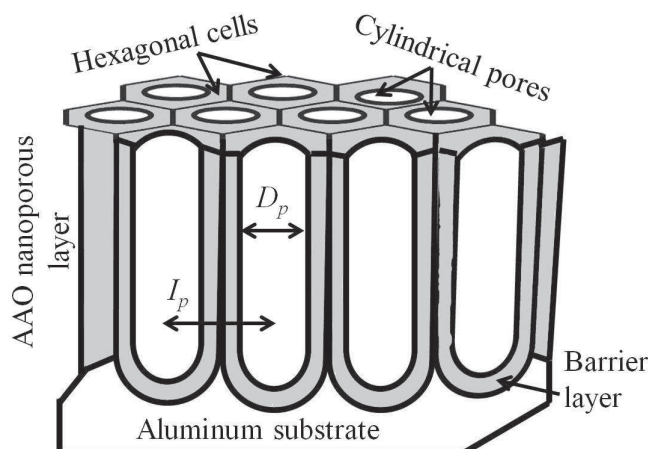


Figure 2.1: Schematic view of porous alumina membrane, note: D_p is the diameter of the pores and I_p is the inter-pore distances measured from centre to center of the neighbouring pores

2.2 SELF-ORDER HEXAGON ARRAYS OF AAO MEMBRANE

2.2.1 Experimental set-up for anodization

When a high purity Al foils is oxidized under anodic process in an acidic electrolyte, a porous oxide film is formed. A two-step anodization process was adopted to synthesize highly ordered AAO templates under two different acidic electrolytes. The experimental setup for anodization is shown in figure 2.2 and used for anodizing Al samples in this work. It consists of a source meter (Keithley 2400) and a refrigerated circulator (Poly-Science, USA) with temperature stability of ± 0.1 °C in the temperature range of -50 to +80 °C. At low temperatures, especially below 5 °C, a mixture of water and ethylene glycol with 40:60 ratio was used as a coolant. During our anodization experiment, a borosil beaker (250 ml) covered with a Teflon lid was used as an anodization cell (inset in Fig. 2.2). The lead was designed with clamps to hold two electrodes i.e. anode (Al foil) and cathode (Pt wire) at 30 mm apart. It also provides the electrical feedthrough to connect the power supply. The whole arrangement was kept partially dipped inside the circulator bath to have thermal stability at the set temperature. A LabView program was developed for automation and recording the data.

2.2.2 Steps followed in anodization

Hexagonally arranged well ordered porous AAO membranes were fabricated by taking a high purity Al (99.99 %, sigma Aldrich) foil with dimension of 40 mm x 10 mm x 0.13 mm. Prior to anodization, surface cleaning of Al was done by using ultrasonication in acetone for 30 min, followed by rinsing the foil with deionized water (Milli-Q) and

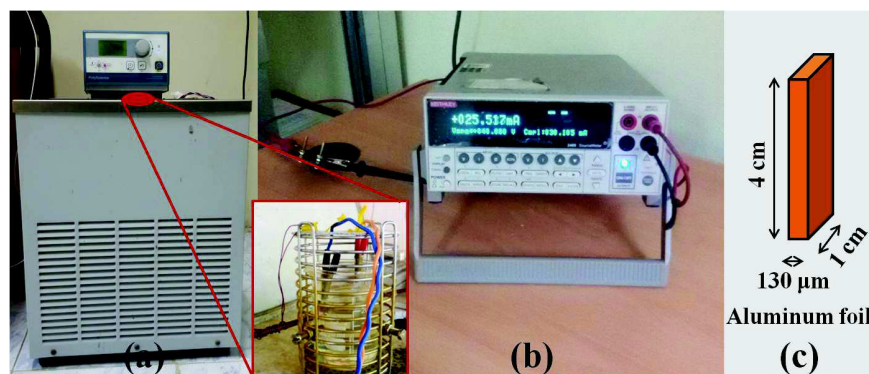


Figure 2.2: Experimental setup of anodization cell: a) Water bath with thermal controller ($\pm 0.1^\circ\text{C}$), b) Keithley source meter, and c) dimension of Al used. Inset show the beaker kept inside the water bath which contain weak acid as well as both the anode (Al) and cathode (Pt) electrodes.

then dried. The cleaned Al foil was then anodised at a constant voltage in the voltage range from 15-30 V in an electrolyte bath with 0.3 M sulphuric acid concentration and 30-60 V in a bath with 0.3 M oxalic acid concentration. For fixed anodising voltage, experiments were performed at different set temperatures in the range from 0 to 15 $^\circ\text{C}$.

During the 1st anodization, the rearrangement of pore ordering towards a hexagon array is observed due to the merging of neighboring incipient pores. As this ordering is a slow process, in this work, 1st anodization was continued for a duration of 10 hrs. This leads to increase the ordered domain size up to $\sim 1\text{-}2 \mu\text{m}^2$ at self-ordering voltage. The optimum self-ordering voltage depends on the electrolyte, i.e, 25 V in the sulphuric acid bath and 40 V in an oxalic acid bath. At the end of the 1st anodization, the oxide (AAO) film was removed by wet-chemical etchant (i.e., mixture of 1.8 wt% chromic and 6 wt% of phosphoric acid) at 60 $^\circ\text{C}$ for a duration of 45 mins. Thereby, the resultant surface of the unreacted aluminium foil contains arrays of ordered concave nano-hemisphere structures, which assist as nucleation sites during the subsequent anodization.

Prior to subsequent anodization, an acrylic polymer (PMMA: polymethyl methacrylate) was applied on one surface of unreacted Al foil, obtained after the completion of 1st step of anodization and subsequent etching of the oxide layer. When this foil kept under subsequent anodization keeping same parameters as the 1st one, the PMMA layer protects the coated Al surface and the anodic reaction with the uncoated surface initiates with a highly ordered pore structure even at the beginning of the 2nd anodization. Through the 2nd step of anodization provides unique size nano-dimensional cells with a constant pore diameter, however, further enhancement in pore diameter within the restricted cell dimension was tuned to the desired value by post-etching treatment in an appropriate etching solution. The length of the cylindrical pore or the thickness of

the membrane was controlled by the duration of second anodization with respect to the growth rate of the porous film. The growth rate depends on the electrolyte (i.e., the concentration of anionic species O^{2-} and OH^-), applied voltage, and the bath temperature. For example, the growth rate was observed to be ~ 2.5 nm/s in 0.3 M sulphuric acid at 25 V, 3 °C, and ~ 1 nm/s in 0.3 M oxalic acid at 40 V, 10 °C. In this work, the prepared membrane thicknesses were varied from 100 nm to few μm with varying the anodization duration from 20 sec to 2 hrs respectively.

After completion of the second anodization, the sample was rinsed with distilled water followed by the removal of PMMA (i.e., coated back side of Al surface) using acetone. To obtain a free standing alumina membrane, the following steps were followed: (i) a thick layer of PMMA was coated on the top of AAO film (i.e., the anodized surface of Al) and then attached to a substrate as a supporting base, (ii) subjected to CuCl_2 solution until unreacted Al was completely removed, (iii) removal of the barrier layer at the pore bottom and subsequently the pore widening in phosphoric acid solution, and (iv) dissolved the PMMA in acetone and rinsed with water, and (v) then the membrane was heated up to 150 °C to remove the content of water/acid which are trapped inside the nanochannel arrays during the fabrication processes. Figure 2.3 shows the schematic representation of these process steps including the membrane preparation.

2.3 FABRICATION OF NANOSTRUCTURES

Free standing and large aspect ratio membranes with variable pore diameters (D_p) and the inter-pore distances (I_p) were used to grow magnetic Co nanowire arrays via electro-deposition process. In addition to this, the small aspect ratio membranes, UTAM (i.e., thickness ≤ 100 nm) were used to fabricate highly ordered arrays of nanodot (Lei et al. 2007) by serving as shadow masks in sputtering or physical vapour deposition techniques. The detailed description of these techniques are given below:

2.3.1 Nanowire arrays

2.3.1.1 Electro-deposition

Electro-deposition is most commonly used technique to grow nanowires due to higher and uniform filling rate inside the nanopores of an alumina membrane. In this work, three-terminal electrochemical workstation (SP150-Bio-Logic Instruments) was used to carry the electrodeposition and the deposition potential was controlled with respect to the reference electrode ($\text{Ag}/\text{AgCl} \sim 0.198$ V). Both potentiostatic and pulsed techniques were used to grow nanowires and their structural and magnetic properties were

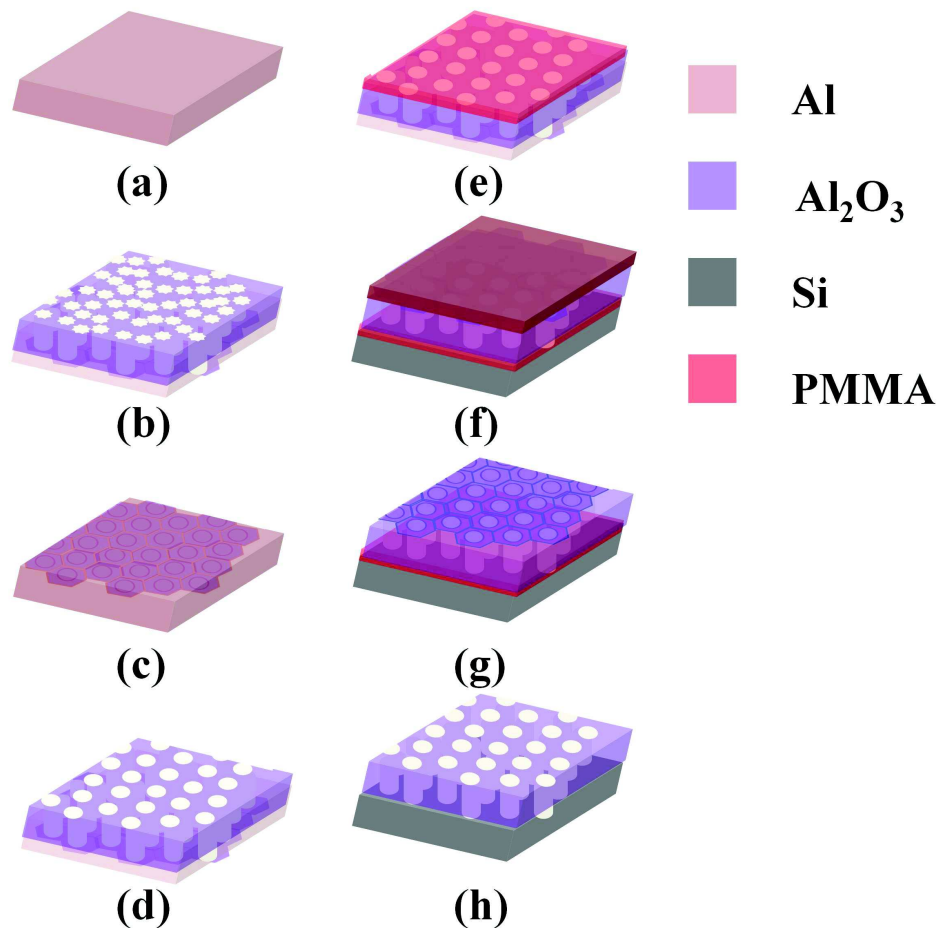


Figure 2.3: (a) High purity Al foil, (b) irregular top pore structures is shown after the 1st step anodization, (c) the ordered arrays of textured Al surface is shown by removing the grown Alumina using Phosphoric and chromic acid solution, (d) highly ordered porous Alumina is prepared on Al by doing the 2nd step anodization, (e) PMMA is coated on Alumina side, (f) PMMA is used as a glue to stick to the substrate (Si or Glass) which illustrate the Al on top for further etching, (g) the hexagonal barrier layer is shown after removing the residual Al by using CuCl_2 , (h) Barrier layer is etched using Phosphoric acid, and then PMMA also removed by acetone, illustrate the through hole free standing AAO / UTAM on substrate.

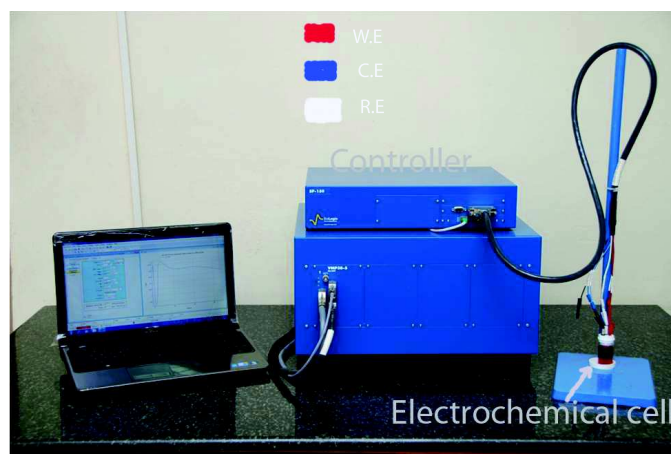


Figure 2.4: The Electro-deposition unit

compared. During the experiment, Ag-coated AAO membrane was used as a cathode/working electrode and Pt wire severed as an anode/auxiliary electrode in the electrolyte containing metal salt to provide ion species during deposition. Figure 2.4 shows the deposition unit, i.e., electrochemical workstation used in this work. The schematic representation of template assisted electro-deposition was shown in Fig. 2.5 for the preparation of nanowire arrays. The required parameters are:

Electrolyte: Electrodeposition was carried out using an aqueous electrolyte containing 120 g/l CoSO_4 and 30 g/l H_3BO_3 at room temperature with pH ~ 4 . The pH of the final electrolyte was adjusted to 2 with H_2SO_4 and 6.7 with NaOH.

Working electrode: The metal (Au or Ag) coated AAO membrane was served as a working electrode for the preparation of NWs. Figure 2.6 show the top view of Ag NSs morphology at the pore bottom of the AAO membrane for two different pore diameters. The thickness of the Ag-coated film was around 300 nm. From this figure, it is clear that the Ag NSs are uniform in size and the tip of each Ag NS provides an active surface area to grow individual nanowire within the nanochannel through electrodeposition process.

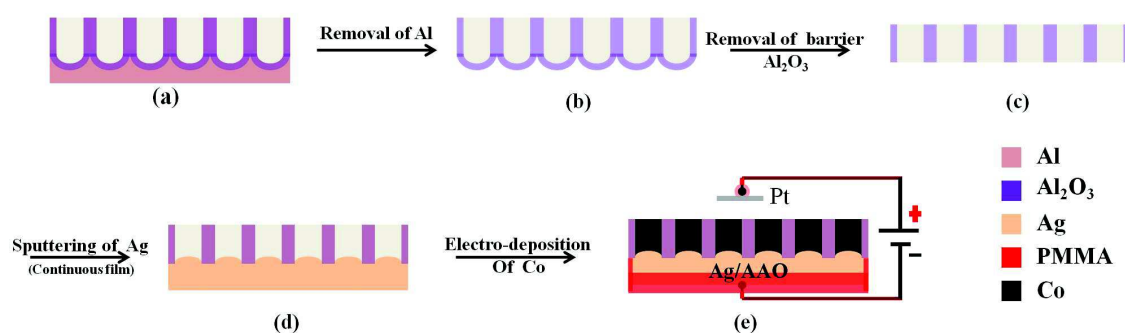


Figure 2.5: Scheme of the process for template assisted electro-deposition.

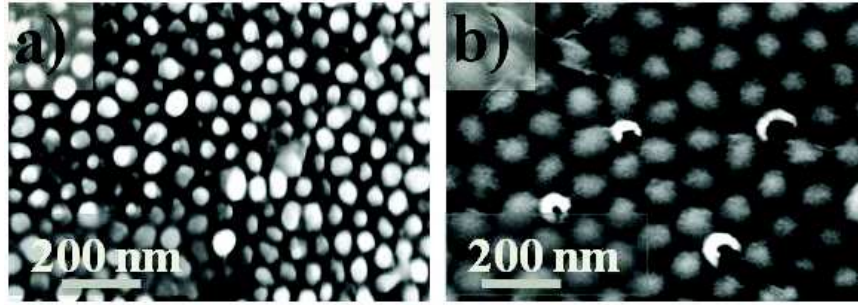


Figure 2.6: Surface morphology of hemi-spherical Ag nanostructures via sputtering which is formed inside the pore bottom of AAO membrane: a) $D_p = 45$ nm and $I_p = 65$ nm (H_2SO_4 , 25 V, 3 °C), and b) $D_p = 85$ nm, $I_p = 105$ nm ($\text{C}_2\text{H}_2\text{O}_4$, 40 V, 10 °C), respectively. The AAO membrane was removed by using 5 M of NaOH solution.

To provide the electrical connection, the Ag-coated membrane was glued with a Cu lead using silver paint. Then, the exposed surface area of Ag film was painted by a thick layer of PMMA and subsequently dried under the lamp. This ensures that the measured current during the electrodeposition process arises due to the diffusion of Co^{2+} ions through the nanochannels and hence the 1D growth of Co nanowires (see Fig. 2.5(e)).

Under potentiostat condition, two different modes i.e., pulse and continuous modes were used to grow nanowires which are discussed below. Under these modes of operations, the growth parameters are tabulated in table 2.1.

Pulse deposition: A single polarity was maintained throughout the voltage cycle with a pulse height of -2 V and constant pulse ratio (=1, i.e., the ratio of pulse duty (T_{ON}) and relaxation time (T_{OFF})) (Zhang et al. 2007). In this work, the pulse frequency was kept constant at 25 Hz with 50 % duty cycle with $T_{on} = T_{off} = 20$ ms. Figure 2.7(a) shows the pulse duty cycle and the corresponding current transits vs time. The uniform current transits show the growth of Co NWs inside the pore channels. Whereas, the resultant +ve current during the relaxation time may signify for the depletion and rearrangement of Co ions near the working electrode.

Continuous deposition using CA mode: The deposition potential was maintained

Table 2.1: Electrochemical deposition modes and their conditions for the synthesis of Co nanowires

Electrodeposition parameter → mode of deposition ↓	Potential applied (V)	Bath temperature (°C)	T_{ON} (ms)	T_{OFF} (ms)	Growth rate (nm/s)
Pulsed	-2	25	20	20	100
Continuous	-1.1	40	15 k	-	30

constant at -1.1 V. The filling of the pores was monitored by measuring the deposition current. The current transits *vs* time indicates two different growths of Co nanowires: homogeneous and non-homogeneous filling, as shown in Fig. 2.7(b). The whole filling mechanism can be divided into three regions: (i) the initial nucleation, (ii) steady state growth inside the pores, and (iii) for the overfilling of the pores that emerging the wires into a continuous film. In this work, the samples of Co NWs were considered when the steady state filling (homogeneous) has occurred to produce straight wires (i.e., the length of wires \ll the membrane thickness). The length of the wire was determined by the deposition time. One of advantage in CA mode that the bulk pH of the electrolyte affects the crystallographic structure of the nanowire with identical growth conditions. So in this work, we have grown nanowire with different crystallographic structures by varying the pH from 2 to 6.7 and utilized only for hcp Co (002) phase to compare their structural and magnetic properties in different pore geometries, as discussed in Chapter 4.

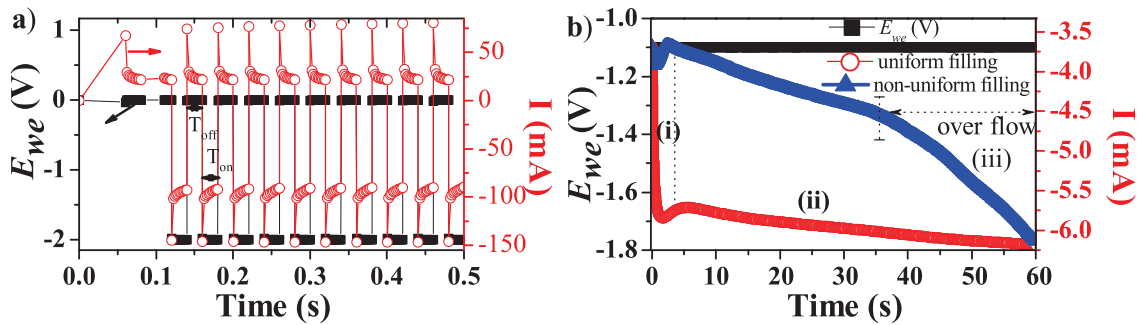


Figure 2.7: The voltage (E_{we}), current (I) transits *vs* time for Co electro-deposition: a) pulse mode with pulse height of -2 V [freq=25 Hz, for $T_{on} = T_{off} = 20$ ms], and b) continuous mode at -1.1 V with two different filling rates: uniform (open circle) and non-uniform (filled triangle), i) nucleation time, ii) filling inside the pores, and iii) over-flow of the pores, respectively.

2.3.2 Nanodot arrays

In this work, we prepared Co nanodot arrays by using physical Vapour Deposition. The experimental details are provided below:

2.3.2.1 Physical Vapour Deposition (PVD)

Fabrications of high-quality magnetic nanodot array of different materials were carried out using sputtering techniques. An ultra high vacuum (UHV) compatible dc magnetron

sputtering system with a base pressure of 10^{-8} mbar was used to carry out this deposition. Prior to sputtering process, UTAM was transferred on the top of ultrasonicated clean Si substrate, which acts as a shadow mask. Here, the adhesion between the substrate and the attached UTAM layer was improved by fast evaporation of acetone and it is believed that this adhesion is due to the presence of weak van der Waal's force. The Si substrate with attached mask was then further heated at ~ 150 - 200 °C for more than 1 hr to remove water/chemical contents inside the pore walls. These substrates were then used to grow nanodot arrays of Co and Co alloys ($\text{Co}_{90}\text{Fe}_{10}$, and SmCo_5) using sputtering technique. The schematic presentation of process steps to fabricate ordered nanodot arrays via vapour phase deposition is shown in Figure 2.8.

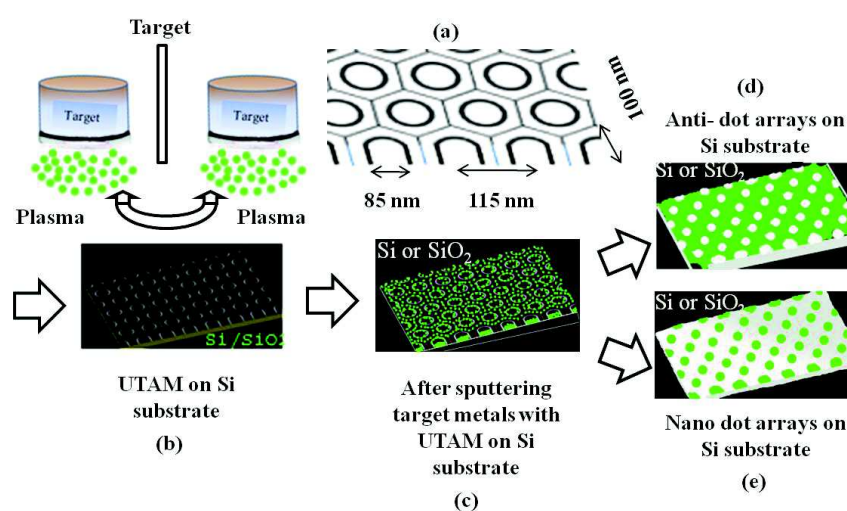


Figure 2.8: Scheme of synthesis of dot arrays via vapor phase deposition.

During the deposition process, the sputtered materials were entered through nanopores of the mask and formed nanodot arrays. At the same time, the coated materials on the top of the membrane formed an antidot arrays. Therefore, Si substrate with only nanodot arrays were achieved by removing the membrane in acetone/NaOH solution through ultrasonication. As the deposited film thickness increases, the aperture size of the nanopore decreases due to shadow effect. This shadow effect modifies the shape of the nanodot array from disk to hemisphere to hemi-elliptical to hemi-conical as a function of film thicknesses (Lei et al. 2005, Lei et al. 2007).

2.4 CHARACTERIZATION TECHNIQUES

2.4.1 Analysis of elemental structure and composition

X-ray diffraction (XRD) is used to determine the crystal structure of the Co NSs. It is one of the most frequently applied techniques in material characterizations. It has

a wavelength in the angstrom range, that are sufficiently energetic to penetrate solids, and are well suited to probe their internal structure. Here, It has been used to identify crystalline phases of Co NSs by means of lattice structural parameters and to obtain an indication of nanosize effect. In general, XRD is the elastic scattering of X-ray photons by atoms in a periodic lattice. The scattered monochromatic X-rays that are in phase give constructive interference. This allows to derive the fingerprint of the crystalline plane from the unique d_{hkl} value (i.e., lattice spacings) of the material by using the Bragg relation:

$$n\lambda = 2d_{hkl}\sin\theta; \quad n = 1, 2, \dots \quad (2.4.1)$$

where, λ is the wavelength of the X-rays, d_{hkl} is the distance between two lattice planes, θ is the angle between the incoming X-rays and the normal to the reflecting lattice plane and n is the integer called the order of the reflection.

In this work, the XRD pattern of Co NSs is measured with a stationary X-ray source of Cu $K\alpha$ with an energy of 8.04 keV and a wavelength of 0.154 nm, and a movable detector, which scans the intensity of the diffracted radiation as a function of the angle 2θ between the incoming and the diffracted beams [D8 Advanced Bruker X-ray diffractometer]. For Co NSs embedded inside alumina membrane, an image of diffraction lines occurs because a small fraction of the Co NSs will be oriented such that by chance a certain crystal plane is at the right angle θ with the incident beam for constructive interference.

X-ray diffraction has an important limitation: clear diffraction peaks are only observed when the sample possesses sufficient long-range order. The advantage of this limitation is that the width (or rather the shape) of diffraction peaks carries information on the dimensions of the reflecting planes. Diffraction lines from perfect crystals are very narrow, whereas, in our case for crystallite sizes below 100 nm, however, line broadening occurs due to incomplete destructive interference in scattering directions where the X-rays are out of phase. The resultant characteristics behaviour are discussed in Chapter 4.

2.4.2 Surface topography

Electron Microscopy: It yields remarkable surface images preferably in atomic details. Unfortunately, optical microscopy is of no use for achieving this, due to the light source of long range wavelength (λ is in the range of visible region, i.e., few 100 nm) which limits the image resolution ($=\alpha\lambda/NA$, where NA is the numerical aperture). Moreover, the diffraction effect and the aberration effect of the lens also contribute in the formation

of image processing. However, electron microscopes could routinely achieve magnifications in the order of one million times and reveal details with a resolution of about 0.1 nm. Since, the sample surfaces are examined with accelerated electron beam, the associated wave function of each electron has a wavelength of $\lambda = h/mv = h/\sqrt{2mE}$, where m is the mass, v is the velocity of the electron, and h is the Planck constant, that can be derived by the de Broglie relation. With the increase of the kinetic energy (E in eV), the decrease in λ will be achieved (\sim less than 0.1 nm) under the ordinary conditions of operation in electron microscopy. In addition to this, optical lenses are replaced by the electromagnetic lenses that have been used to focus the electron beam on the specimen surface. This assist to provide two major benefits in electron microscopes; (i) range of magnification and (ii) depth of field of the sample surface. Therefore, it is possible to achieve an extremely small electron beam diameter and angular aperture, that results for much higher resolving power and field depth than those obtained with light microscopy. In order to generate and propagate the electron beam, the system requires high-vacuum chambers that impose some restrictions on the characteristics of the samples for observation. Moreover, there are several methods of electron microscopy that classified by (i) depending on the characteristics of the lighting system (the incident electron beam generation and guidance control), (ii) the mode to detect radiation emerging from the sample (under the electron beam impact), and (iii) the image construction.

In this work, the morphology of the AAO template and the Co NSs are studied by using Field Emission Scanning Electron Microscopy (FESEM, ZEISS Supra 40V). In general, it is different from the generation of electron beams that produced by field emission principle than the ordinary scanning electron microscope (SEM). However, SEM is carried out by rastering a narrow electron beam over the surface and detecting the yield of either secondary or backscattered electrons as a function of the position of the primary beam. Contrast is caused by the orientation, parts of the surface facing the detector appearing brighter than parts of the surface with their surface normal pointing away from the detector. The secondary electrons have mostly low energies (\sim 5-50 eV) and originate from the surface region of the sample. Backscattered electrons come from deeper regions and carry information on the composition of the sample because heavy elements are more efficient scatters and appear bright in the image.

Energy Dispersive X-Ray Spectroscopy (EDS): As the electron beam of the FESEM is scanned across the sample surface, it generates X-ray fluorescence from the atoms in its path. The energy of each X-ray photon is characteristic of the element that produced it. The EDS microanalysis system collects the X-rays, sorts and plots them by energy, and automatically identifies and labels the elements responsible for the peaks in

this energy distribution. EDS identifies the elemental composition of materials imaged in FESEM for all elements with an atomic number greater than boron. Most elements are detected at concentrations on the order of 0.1%.

2.4.3 Scanning Probe Measurement

One of the non-destructive approach in the recent developments for determining the surface structure is the Scanning Probe Microscopy (SPM). Atomic Force Microscope (AFM) is one of the SPM technique. It is capable of imaging the local surface topography with atomic resolution. In principle, a sharp tip is a raster across a surface by piezoelectric transducers, while a certain property reflecting the interaction between the tip and the surface is monitored and yields local information. For AFM, the detectable forces are the van der Waal's forces in the order of magnitude nano-Newtons (nN), which acts between the sharp tip and the atoms in the surface. The tip is mounted on a flexible arm called cantilever and is positioned at a subnanometer distance from the surface. If the sample is scanned under the tip in the $x - y$ plane, it feels the attractive or repulsive force from the surface atoms and hence is deflected in the z direction. Therefore, the topographic images are generated by variation in the van der Waals forces that associated with the tip-sample distance. Various forces have been utilized between the tip and the sample surfaces. In order to measure the magnetic stray field on the surface of our samples, magnetic force microscopy (MFM) is used to measure the magnetic force between the magnetized tip and magnetic sample of Co NSs. During the MFM measurements, there are two forces acting on the tip; magnetic and Van der Waals forces. The dominating force depends on the distance between the tip and the sample surface, since the inter-atomic magnetic force persists for greater tip-to-sample separations than the van der Waals force, a lift-off process in non-contact AFM mode is operated. This yields a local magnetization state or the magnetic domain distribution on the sample surface.

2.4.4 Magnetometry Studies:

Vibrating Sample Magnetometry (VSM): The magnetic characterization of materials is usually made by measuring a hysteresis loop, from $+M_s$ to $-M_s$ and vice versa at a particular temperature. In this work, a high sensitive VSM (LakeShore) is used to characterize the magnetic properties of the Co NSs at room temperature as a function of magnetic field (~ 10 kOe) and time. The basic principle of VSM is based on the Faraday's law of electromagnetic induction, which states that the voltage $V(t)$ induced in an electrical circuit is proportional to the rate of change of magnetic flux linking the

circuit ($d\phi/dt$),

$$V(t) = -C \frac{d\phi}{dt} \quad (2.4.2)$$

In this case, a sample is attached to a vibrating rod and allowed to vibrate in a magnetic field produced by electromagnets. With an increase in the magnitude of the applied magnetic field increases in the magnetization of the samples, which cause a change in magnetic flux to induce a net voltage signal. This signal can be measured by the induction coils located near the samples. It is usually small and is measured by a lock-in amplifier at a frequency specified by the signal from the sample vibrator. The signal measured by the induction coils is directly proportional to the magnetization of the sample and independent of the external field intensity. While plotting the Magnetization (M) vs applied magnetic field intensity (H) results in a hysteresis curve representative of the samples magnetization. In this work, the $M(H)$ loops are measured in both parallel and perpendicular to nanowire axis, (i.e., out-of-plane and in-plane to the substrate). However, the low temperature $M(H)$ loops of Co NSs are characterized by using superconducting quantum interference device (SQUID) magnetometry.

2.4.5 Micro-magnetic simulation

Micromagnetic simulations are also used to understand the nano-magnetism with a clear image of magnetic spin configurations. The simulations were performed using object-oriented micromagnetic simulation software (OOMMF: Donahue et al. 2012). The parameters used for the calculations are taken from bulk Co, for the exchange constant, the saturation magnetization, and K_1 for the cubic or uniaxial anisotropy. In these calculations, the cell size is selected to be $2 \times 2 \times 2 \text{ nm}^3$ and mentioned that wherever is required, which is much smaller than the exchange length $L_{ex} = \sqrt{8\pi A/\mu_0 M_s^2}$ ($\approx 7 \text{ nm}$ for Co) with μ_0 being the permeability of vacuum. We then compute the equilibrium magnetization patterns for our magnetic NSs. The dynamics of magnetization are discussed in Chapter 6.

Chapter 3

FABRICATION OF POROUS ALUMINA MEMBRANE: OPTIMUM CONDITIONS FOR SELF-ORDERED PORES

In this chapter, fabrication of anodic Aluminum Oxide (AAO) templates/membrane using sulfuric and oxalic acid as electrolytes are discussed. Influence of varying anodization voltage and bath temperature on pore morphology is discussed

3.1 SELF-ORDERED POROUS ALUMINA MEMBRANE

3.1.1 Anodization of Al

A century-old industrial process, anodization of Al exists with two different oxide layers, (i) non-porous or barrier alumina, and (ii) porous alumina film in aqueous electrolytes (Li et al. 1998, Zhu et al. 2009). The nature of oxide layer is determined by pH of the electrolyte (Li et al. 1998, Sulka et al. 2008, Zhu et al. 2009). For example, non-porous barrier oxide film can be formed in neutral and non-aggressive solutions, (i.e., pH 5-7) such as borate, oxalate, citrate, phosphate, tungstate solution, etc., in which the anodic oxide is practically insoluble. Whereas, the porous alumina film is formed in weak acid electrolytes, such as selenic, sulfuric, oxalic, phosphoric, chromic, malonic, tartaric, citric acid, etc. It is also well known that the growth kinetics of these two different types of oxide layers are different. In the case of barrier alumina, under potentiostatic anodization, the current density decreases exponentially with time as the thickness of the barrier AAO film increases. Hence under this condition, the thickness of the barrier layer is determined by the applied voltage. Whereas, in case of porous alumina film, the initial formation of oxide layers reduces current density to a constant value with a short span of time when subjected to anodization under potentiometric condition and maintains this value as the anodization progresses.

In general, the alumina film is formed due to the movement of Al^{3+} ions from the metal across the metal/oxide interface and $\text{O}^{2-}/\text{OH}^-$ ions are formed from water at the oxide/electrolyte interface and migrate into metal/oxide interface, respectively (Li et al. 1998). Non-porous barrier-type AAO film is formed on two interfaces with the highest forming efficiency of the oxide, i.e., current efficiency ($\eta_j = 100\%$) in neutral solution. Whereas, in porous AAO film, the forming efficiency is much lower ($\eta_j = 53.5\%$) than the barrier film, because the egress of Al^{3+} cations do not contribute to the

oxide growth at oxide/electrolyte interface in acid solutions, i.e., the oxide formation occurs only at metal/oxide interface at initial phase of the growth (Sulka et al. 2008, Lee et al. 2014). On the other hand, the current efficiency (η_j) can be represented by the Pilling-Bedworth ratio (PBR), i.e., the ratio of the molar volume of the grown oxide to molar volume of the consumed metal in oxide formation process. It is suggested that the barrier-type AAO has a value of PBR ~ 1.7 , for the growth of highly uniform oxides on Al surface, maintaining flat metal/oxide and oxide/electrolyte interfaces. Meanwhile, low PBR ~ 0.9 is reported at the initial barrier oxide formation in porous AAO, whereas highly ordered porous alumina has been reported in the range of 1.22 to 1.45 (Jessensky et al. 1998, Li et al. 1998, Nielsch et al. 2002), irrespective of the electrolyte. This leads to increase the tensile stress on the initial growth of barrier AAO, which causes the formation of some flaws and embryo voids on the surface. The generated defects are considered to be local paths for electrolyte penetration, causing non-uniform local thickening of the initial barrier oxide. Therefore, different growth features of the initial barrier oxide, such as non-uniform thickening or flat anodic oxide layers can distinctly differentiate the porous- and barrier-type AAO films as reported by Shimizu et al. (2011). Further discussion is for porous AAO film, which is particularly focused as part of this Ph.D. work.

Thus, the non-uniform thickening of anodic oxide arises to local increase in the electric field, E caused by the concentration and redistribution of the current lines into the relatively thin oxide regions between the protrusions. Further reactions in acidic electrolyte result with the development of regular pores with concentrated E at the pore bases. During the process the steady-state pore growth (i.e., almost constant current density) is established and the thickness of the barrier oxide layer is maintained by the dynamic rate balance between the two processes: (i) oxide formation and (ii) oxide dissolution, occurring at the oxide electrolyte interface. The oxide formation is mainly due to the reaction between O^{2-} ions and Al^{3+} ions migrated at the metal/oxide interface, as in the formation of barrier-type oxide and the oxide dissolution is the outward migrating of Al^{3+} ions which exclusively ejected to the electrolyte under the enhanced electric field at the pore bases (i.e., oxide/electrolyte interface). Therefore, unlike barrier-type AAO, the pore growth and development of AAO film has been explained by the field assisted dissolution (FAD) model at the pore bottom.

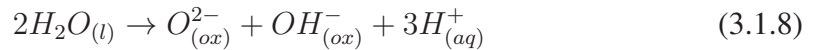
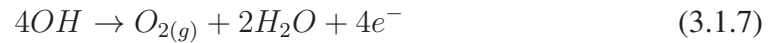
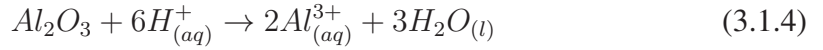
3.1.2 Electro-chemical mechanism of pore formation

For anodization of Al, migration of both anion (O^{2-} and OH^-) and cation (Al^{3+}) are involved at metal/oxide and oxide/electrolyte interfaces. As mentioned above, the steady-state equilibrium condition leads to porous AAO growth via oxide formation and dissolution at oxide electrolyte interfaces. Therefore, chemical reactions at the two interfaces are considered, and the possible reactions are (Li et al. 1998, Zhu et al. 2009, Lee et al. 2014):

(i) At the metal/oxide interface:



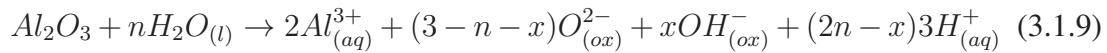
(ii) At the oxide/electrolyte interface:



The balance between the rate of oxide formation and dissolution is determining the steady-state pore deepening process. In this case, the formation of anodic oxide at the metal/oxide and oxide/electrolyte interfaces correspond to reactions 3.1.2 and 3.1.3, respectively. Whereas, the oxide dissolution is described in reaction 3.1.4 and it can be stimulated by two factors, such as Joule's heating- and/or field-assisted oxide dissolutions. However, direct ejection of Al^{3+} ions also occur from the metal/oxide interface to the electrolyte through oxide, by field-assisted mechanism in reaction 3.1.5. Therefore, the net current efficiency (η_j) associated with the anodic oxide formation is decreased

by reactions 3.1.4-3.1.6 for porous-type AAO. In addition to this, the heterolytic dissociation of water molecules at the oxide/electrolyte interface also supply oxygen anions to the metal/oxide interface to form an anodic oxide, in reaction 3.1.7.

Su et al. (2009) were proposed the overall reaction at oxide/electrolyte interface, by assuming the possible oxide anion formations: such as (i) from the dissolution of Al_2O_3 at the oxide/electrolyte interface may reform the oxide at the metal/oxide interface, and (ii) from the dissociation of water may contribute to the oxide formation. The overall reaction at oxide/electrolyte interface is:



where the ratio of produced O^{2-} and OH^- cannot be determined, while n is used to indicate the molar ratio of dissociation water and the dissolution of Al_2O_3 at the same time. In addition to this, the relative dissociation rate of water is also demonstrated for AAO film with disordered pores. In a simple relation, the heterolytic dissociation of water at the oxide/electrolyte interface is proposed for the key factor for governing the porosity (P = ratio of the pore size to the cell dimension) of ordered AAO films, rather than the position of the pores. In this regard, Su et al. (2009) claimed the field dependent nature of the heterolytic dissociation, which accounts for the decreasing porosity with increasing applied field.

$$P = \frac{\pi}{2\sqrt{3}} \left(\frac{D_p}{I_p} \right)^2 = \frac{3}{(n + 3)} \quad (3.1.10)$$

However, the attainment of long-range regular porous structure and the control over the pore size and the cell size is determined by the anodization parameters, such as applied potential or current density, nature of electrolyte, pH, and bath temperature. In this regard, self-ordered pore arrangements are prepared by two-step anodization process, as described in Chapter 2. Moreover, perfectly ordered alumina structures are also achieved in a single-step anodizing by Al pre-nanoindentation via various techniques (Masuda et al. 1998, Masuda et al. 2002, Masuda et al. 2004). In this work, a simple two-step anodization is considered and the conditions for the preparation of self-ordered porous AAO membrane is described below:

3.2 ANODIZATION CONDITIONS

The self-assembled pore formation in alumina film in 0.3 M H_2SO_4 electrolyte was carried out at different anodization potentials in the range from 15 to 25 V while keeping the bath temperature at different set values from 1 to 15 °C. In order to understand

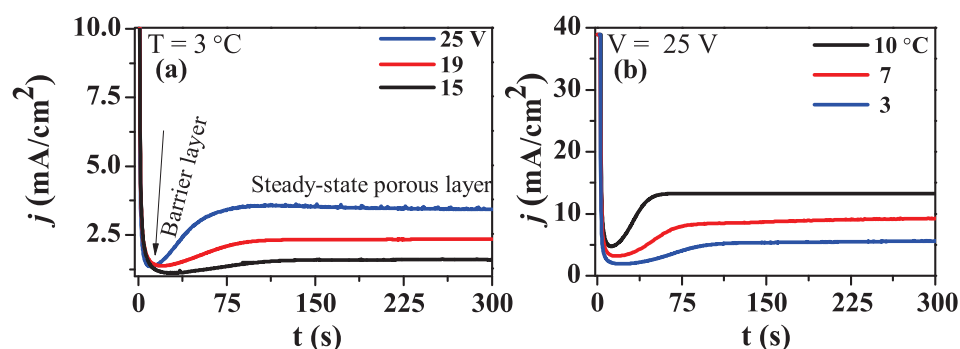


Figure 3.1: Current density vs time characteristics of Al anodization: a) for different anodization potential at constant temperature (3 °C), and b) for different anodization temperature at constant potential (25 V).

the behavior of anodization process, a real-time current evolution was monitored to evaluate the steady state anodization, i.e., from the current density (j) vs time (t) transit. Figure 3.1(a) presents the plot of j vs t curves for three different values of anodizing potential 15, 19, and 25 V where the electrolyte bath temperature was kept at 3 °C. Figure 3.1(b) presents the similar plots for three different temperatures, 3, 7 and 10 °C with a constant anodizing potentials of 25 V. Irrespective of the anodizing potential or the bath temperature, at the beginning, j decreases rapidly and then maintain at a steady-state value. The drop in j indicates the increase in resistance i.e., barrier layer formation and then j increases slowly towards a saturated value. This is due to the dissolution of alumina at the oxide/electrolyte interface. As j reaches to a saturated value, the anodization process reaches an equilibrium stage where the rate of oxide formation at metal/oxide interface becomes equal to the rate of dissolution at oxide/electrolyte) around the pore bottom. From this figure, it is clear that the stable anodizing process can be achieved under various anodization conditions. However, the highly ordered pore geometry was attained in a small window of anodization which are influenced by the effect of electrolyte temperatures and applied potentials. The anodic voltage and the temperature of electrolyte affect both the growth rate and nanopore geometry.

3.2.1 Effect of applied Potential

As shown in figure 3.1, the observed value of j is low while anodization was carried out at 15 V and 3 °C. This indicates that the formation of oxide layer occurs at lower growth rate, which may induce more stress on Al_2O_3 layer (i.e., for a very small value of PBR $\ll 1$ due to the smaller expansion of volume during oxide formation). This may result in a number of small voids or disordered pores. The top surface morphology of porous membranes were shown in Figure 3.2 after second anodization at various

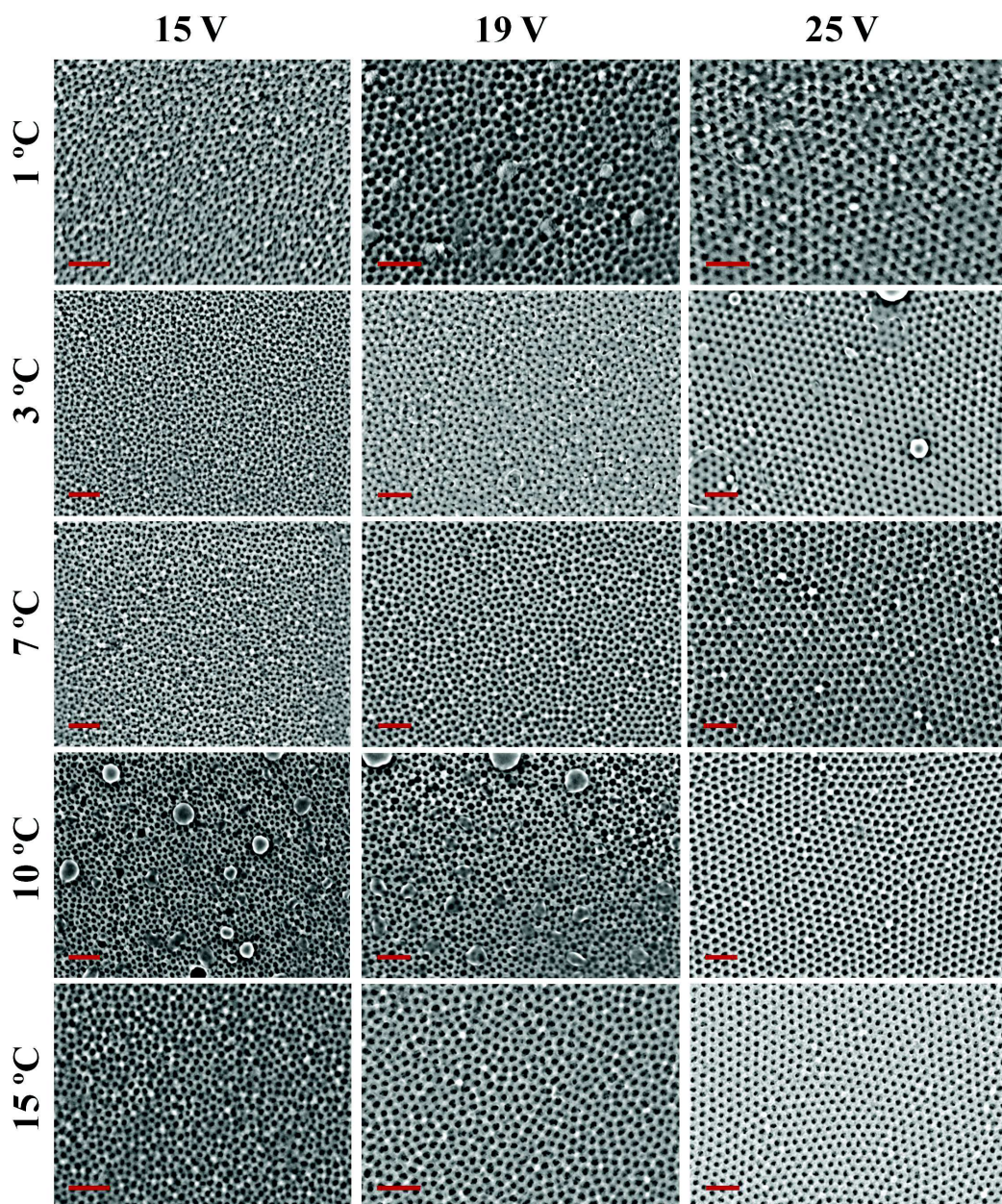


Figure 3.2: Top view of pore arrays grown at different voltages and temperatures. The scale bar is 200 nm.

voltages and temperatures. It can be seen that the pore density (n) was decreasing with increase in applied voltage due to the enhancement in the interpore distance as well as the pore diameter, such as $15\text{ V} > 19\text{ V} > 25\text{ V}$. For higher applied potential, the diffusion of Al^{3+} or $\text{O}^{2-}/\text{OH}^-$ may increase in the oxide electrolyte interface which results higher j values in Figure 3.1. This leads to thickening the alumina film with higher growth rate, i.e., the oxide dissolution rate at pore bottom (oxide/electrolyte interface) was induced by the enhanced electric field strength or by increase in the local temperature (i.e., joule heating) during the steady-state anodization. However, the mechanical stresses and rates of heat dissipation become nonuniform at pore bottom which may affect the pore ordering (Li et al. 1998, Li et al. 1999, Li et al. 2000). According to Jessensky et al. (1998), PBR value is increased with the increase in anodization potential, meanwhile a moderate expansion of Al will offer the highly ordered AAO (PBR ~ 1.22) (Jessensky et al. 1998). In this view, it is suggested that for a fixed volume, the pores were rearranged in a lateral direction to attain hexagonal close packing when the Al_2O_3 layer is expanding freely only in the vertical direction. Therefore, it is clear that the determining factor for adjacent pore distance is the applied potential with respect to the volume expansion of Al.

3.2.2 Effect of bath Temperature

The electrolyte temperature is also influenced in the diffusion rate and the oxide dissolution during the anodization process. Figure. 3.1 (b) indicates that the increase in j as a function of temperature for a constant applied potential of 25 V. Most importantly, the effect of electrolyte temperature was reported for the etching of pore walls wider at top AAO surfaces than at the bottom of pores while doing anodization process for a prolonged time (Aerts et al. 2007). Therefore, here the optimization process was restricted for a short duration (~ 5 min) during the second anodization. In the optimized condition, the influence of electrolyte temperature on the self-ordered porous structure are investigated, and the variations in the pore diameters, inter-pore distances, pore growth rate, and top surface roughnesses as a function of temperature are presented. Here, the first and the second anodizing times are maintained constant throughout the study as 10 hours and 5 minutes. The first anodization time may reflect in the pore arrangement and the domain size. Whereas, the second anodization time only influences in the pore length (i.e., thickness). The set temperature of the electrolyte was maintained with an accuracy of $\pm 1\text{ }^\circ\text{C}$ during each anodization. The average pore parameters, such as pore diameter, inter-pore distance and the porosity of the porous membrane for the given anodization conditions are calculated and tabulated in table 3.1.

Table 3.1: Condition optimization of self-ordered AAO membrane using 0.3 M sulphuric acid.

Anodization \Rightarrow voltage Bath \downarrow temperature	15 V			19 V			25 V		
	D_p (nm)	I_p (nm)	P (%)	D_p (nm)	I_p (nm)	P (%)	D_p (nm)	I_p (nm)	P (%)
1 °C	22 \pm 3	42 \pm 3	0.24	25 \pm 2	46 \pm 4	0.26	33 \pm 3	61 \pm 3	0.26
3 °C	25 \pm 2	44 \pm 2	0.29	29 \pm 3	52 \pm 2	0.28	35 \pm 2	64 \pm 4	0.27
7 °C	28 \pm 4	43 \pm 4	0.38	30 \pm 4	48 \pm 3	0.38	37 \pm 4	63 \pm 5	0.3
10 °C	30 \pm 5	44 \pm 3	0.42	34 \pm 4	50 \pm 4	0.41	38 \pm 2	63 \pm 2	0.32
15 °C	31 \pm 6	45 \pm 2	0.43	35 \pm 5	52 \pm 3	0.41	39 \pm 5	64 \pm 3	0.33

3.3 PORE PARAMETERS

3.3.1 Pore diameter (D_p) and inter-pore distance (I_p)

Figure 3.3 (a,b) shows the variation of inter-pore distance and pore diameter, respectively, with increase in temperature from 1 to 15 °C of the electrolyte at three different anodization potentials in 0.3 M H₂SO₄. It is seen that for a constant anodization potential, the average inter-pore distance remains unchanged with the variation of temperature. However, the inter-pore distance increases with an increase in the anodization potential from 15 to 25 V at a given temperature and supports literature results (Li et al. 1998, Sulka et al. 2002, Sulka et al 2009). The average inter-pore distance varies with anodization potential from 42 \pm 3 nm at 15 V to 64 \pm 3 nm at 25 V in the studied temperature range.

On the other hand, it can be seen that the pore diameter increases with increasing electrolyte temperature and ultimately saturates at a higher temperature for a given anodization potential. This kind of observation is reported for the first time since earlier literature (Aerts et al. 2007, Sulka et al. 2009) mentioned about the monotonous enlargement of pore diameter with the rise in temperature. Basically, a high temperature favors ionic diffusion and reactivity which enhances the chemical dissolution of the formed oxide layer on Al. This dissolution process leads to selective etching of the inside wall of the pore due to the availability of large surface area rather than the pore base resulting into a larger pore diameter. It is also noticed that at a given temperature, the

pore diameter increases with increase in anodizing potential. Therefore, as mentioned above, the inter-pore distance is related with pore nucleation density, and influenced by the function of anodizing potential; whereas the pore diameter is strongly dependent on electrolyte temperature as well as anodizing potential. Indirectly, we can say that the applied anodizing potential essentially patterns the pore arrangement on the Al surface and the combined effect of potential and temperature help unidirectional pores to propagate via dissolution.

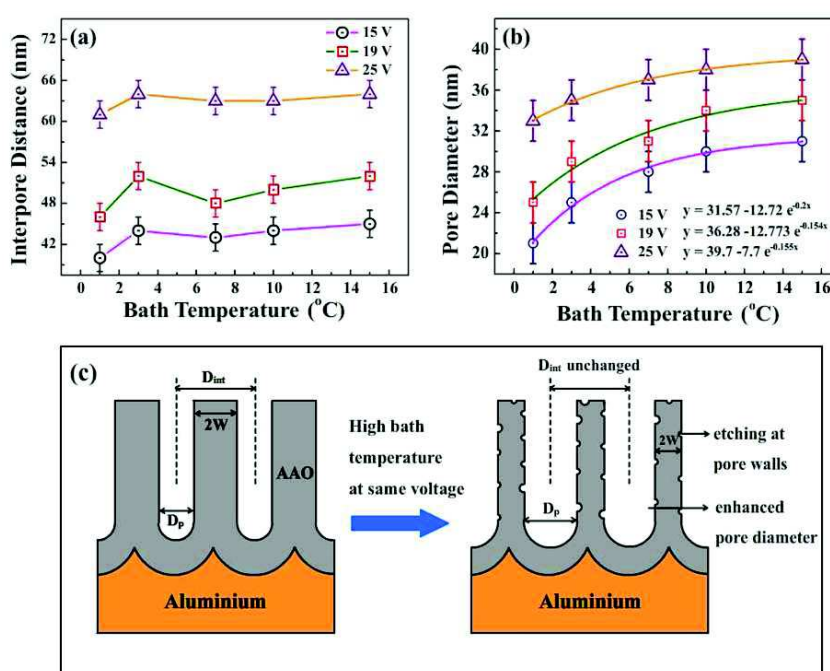


Figure 3.3: (a) Variation of inter-pore distance with bath temperature. (b) Variation of pore diameter with bath temperature. (c) Schematic showing influences of bath temperature on inter-pore distance and pore diameter when the voltage is constant.

In Figure 3.3(c), we show a schematic representation of the temperature effect on inter-pore distance and pore diameter where it is seen that at constant potential, the inter-pore distance is not influenced by enhanced rate of dissolution at various temperatures (see Fig. 3.3(a)), but it helps to assume that only the pore walls are etched to widen the pore size. This enhanced dissolution clarifies the resultant etched surface topography of porous alumina film prepared at elevated temperature (15 °C at 25 V). Further increase in temperature may lead to more opening the pore and declining the wall thickness, supporting the observations made by Aerts et al. (2007).

3.3.2 Porosity

Eventually, at very high temperature the walls between the neighboring pores dissolve merging them together and enlarge the pore size. This also contributes in the porosity calculation of the porous alumina membrane. The porosity of the hexagonal pore structure is given by the relation in Eqn 3.1 that the ratio of D_p/I_p determines the film porosity.

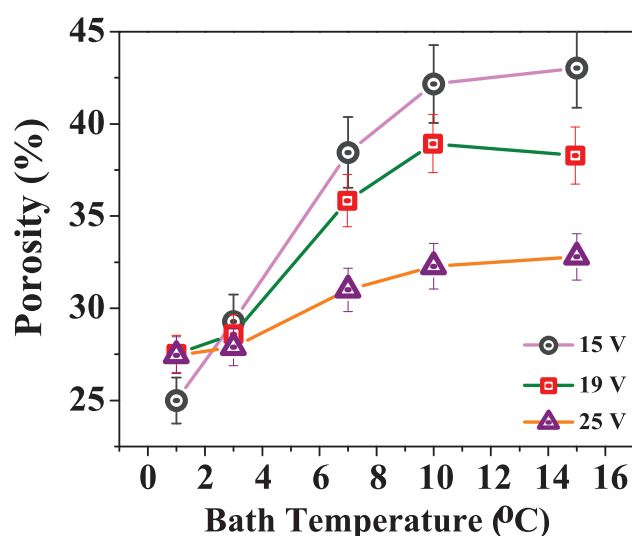


Figure 3.4: Porosity of ordered nanostructures formed by anodizing of aluminium at electrolyte temperatures between 1 °C to 15 °C for three different potentials 15, 19 and 25 V.

Figure 3.4 shows the variation in porosity as a function of temperature for given anodization potential. Irrespective of the anodization potential, the porosity, P , was $\sim 28\%$ at lower electrolyte temperatures i.e., from 1 to 3 °C. With further increasing the electrolyte temperature till 10 °C, the value of P increases from 28% to 42% while anodizing at 15 V and then saturated at higher electrolyte temperatures. The rate of increment in P in the temperature window of 3-10 °C reduces as the anodizing potential increases from 15 to 25 V. This is explained above in terms of the oxide dissolution at the pore walls at higher temperatures. This causes to enlarge D_p without affecting I_p as supported by the literature (Ono et al. 2003). Hence, our porosity calculation also confirms that the higher rate of pore wall etching at lower applied potentials (15 and 19 V) than at 25 V with elevated temperatures. Moreover, D_p/I_p has been reported as a constant factor for the well defined self-ordered porous structure and requires a porosity about 10% independent to anodizing conditions (Nielsch et al. 2002, Ono et al. 2004). Here, the well-ordered porous nanostructure forms at 25 V with a porosity value of $28 \pm 3\%$.

3.3.3 Pore Growth Kinetics

Self-ordering of nanoporous alumina membrane is known to be controlled by current density and high electric field apart from anodizing potential, temperature and bath composition (Ono et al. 2004). At constant anodizing potential, the analysis of transient current density variation with time at different temperatures appears to be very important. Since for heterogeneous processes like electrode/electrolyte interface reactions, the current density (j) is directly proportional to the rate of reaction (k)

$$j = zF.k \quad (3.3.1)$$

where z is valency and F is Faraday's constant. Assuming a first order reaction from the Arrhenius equation (Patermarakis et al. 1991), the reaction rate (k) is related to temperature (T) as:

$$k = A.exp\frac{-E_a}{RT} \quad (3.3.2)$$

where A is a constant and E_a is activation energy and R is universal gas constant. By combining equation (3.3.1) and (3.3.2) one can get a relation between current density and temperature as

$$j = zFA.exp\frac{-E_a}{RT} \quad (3.3.3)$$

which shows an exponential variation of current density with temperature for a given potential and electrolytic condition.

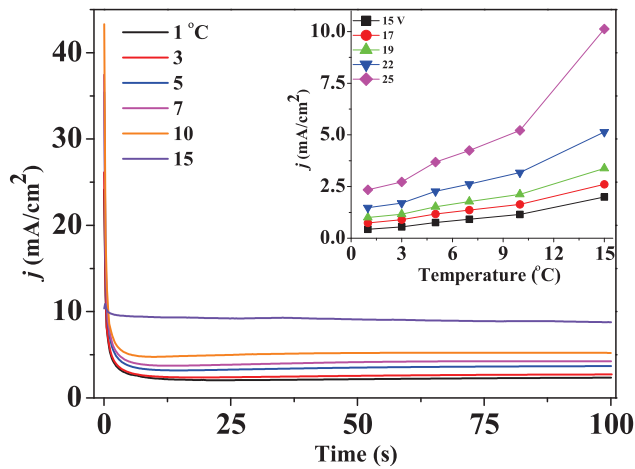


Figure 3.5: Current density vs time characteristics during second anodization of Al at 25 V and inset shows the evolution of steady state current density as a function of temperature at different anodizing potentials.

In order to find out the relation between current density and temperature experimentally, the transient current density behavior was recorded for first 100 s during second-step anodization at different temperatures and potentials as shown in Fig. 3.5. One can see a rapid stabilization of very high current density to a lower steady state value within 5 seconds of starting the experiment. The high beginning current density arises due to the absence of oxide layer and once oxide layer starts forming it reduces drastically. But with an increase in temperature the steady state current density is found to increase obeying the Arrhenius equation (3.3.4). It is also noticed that the variation in steady-state current density is gradual till 10 °C, but it becomes drastic at 15 °C due to the exponential relationship between current density and temperature. Importantly, we also observe that the steady state anodization is attained faster by increasing bath temperature and initiates the growth of porous alumina layer. This behavior is the result of enhanced oxide formation and dissolution rate at the metal-oxide and oxide-electrolyte interface, respectively. Inset of Fig. 3.5 shows the variation of steady current density with the temperature at different anodizing potentials. It is evident that the current density increases with increase in anodizing potential and temperature. This signifies a steady increase in pore growth rate with anodizing potential and temperature. Moreover, within the studied temperature range (1 to 15 °C), the exponential variation of current density with temperature is reflected only at higher potential (22 V and 25 V). A better picture could be visible if one conducts experiments in a wider temperature range.

We have carried out a detailed analysis of the growth rate of AAO films prepared in H₂SO₄ electrolyte at 15, 19 and 25 V to correlate the steady current density data. The bath temperature was varied from 1 to 15 °C. Growth rate, r (nm/s), was obtained by dividing the thickness of membrane (t) by duration of anodization (Han and Shen 2011). The thickness of AAO membrane is measured by a 3D surface profilometer. Duration of anodization was kept in the range of 60-300 s to ensure that the membrane thickness is in the range of 100-400 nm. The thin AAO membrane is placed on a silicon substrate. Since the membrane is very thin, it sticks on the silicon surface. Figure 8 shows the variation of growth rate with bath temperature at different potentials. The growth rate of alumina membrane increases exponentially with bath temperature for all the anodizing potentials. We note that the influence of bath temperature is greater at higher voltages. This is because at higher anodizing potential, enhanced anodizing current influences the growth kinetics as evidenced in Fig. 3.5.

From the detailed analyzes of the effect of temperature on pore diameter, inter-pore distance, current density behavior and growth rate, it is now confirmed that the temperature alone has a significant influence on the pore growth rate apart from the

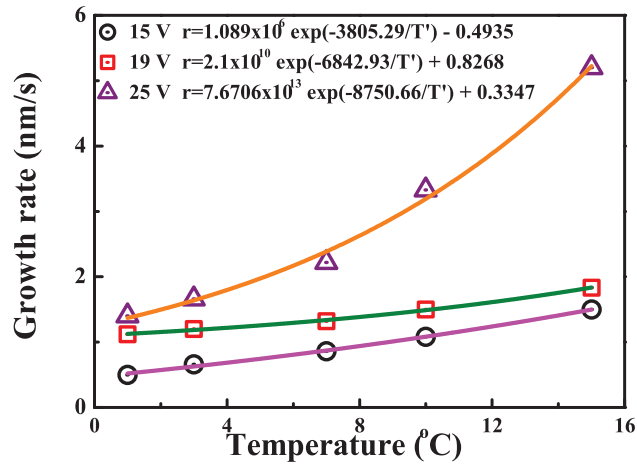


Figure 3.6: Shows the variation of growth rate as a function of temperature for anodizing potentials of 15, 19 and 25 V.

effects of anodizing potential and kind of electrolyte. Higher temperature not only enhances the pore diameter but also it contributes to pore lengthening. Therefore, the increase in resultant growth rate increases the overall thickness of AAO layer. The resultant growth rate (r) vs. temperature curves (Fig. 3.6) of AAO nanopores can be fitted with a modified Arrhenius equation (Patermarakis et al. 1991) as

$$r = A \cdot \exp\left(\frac{-E_a}{RT'}\right) + c, \quad (3.3.4)$$

where, E_a is the activation energy, R is the gas constant (8.314 J/mol.K), T' ($= T+273.15$) is the bath temperature in K , c is constant and A is a field dependent coefficient. The estimated E_a values are 31.6, 56.9, and 72.8 kJ/mol for the given applied potentials 15, 19, and 25 V, respectively in H_2SO_4 medium. These results agree with the previous analysis done by Han and Shen (2011) with the reported value of E_a (75.2 kJ/mol) in H_3PO_4 medium at 140 V. A slight difference in activation energy value could be due to the difference in medium and anodizing voltage.

3.4 FAST FOURIER TRANSFORM (FFT) BASED ANALYSIS OF PORE REGULARITY

Recently, the regularity or the ordering of nanopore arrays in the porous AAO membrane is quantitatively investigated by using 2D or 3D FFT pattern of the FESEM images. This is very helpful to show the effect of anodization conditions towards the symmetry of pore distributions. FFT images are generated from the image software using WSxM (<http://www.nanotec.es>), which works for the structure periodicity in the

inverse space to show the lattice points for the corresponding FESEM images. It reflects the periodicity of the pore distribution, such as, (i) disc shape is for disordered pore structure, (ii) ring is for ordered periodicity with non-uniform pore size, and (iii) six distinct points or six-fold symmetry for the highly ordered pore distributions. According to Sulka et al., (2002), that the higher magnified FESEM image ($0.25\mu\text{m}^2$) can have a better degree of ordering in the FFT pattern to show short-distance ordering in AAO i.e., for the existing smaller domains in AAO surface. Therefore, the limitations of measuring pore regularity by FFT are, the size of the FESEM image, no. of domain (edge may have non-uniform pore distribution) presents, and surface defects in the AAO membrane. In this case, the sample area of FESEM images is kept constant for taking FFT pattern, $1.16\mu\text{m}^2$. The effect of anodization conditions based on their regularity profile is shown below:

3.4.1 Effect of anodization potential

The effect of anodizing potential on the regularity of nanopores was analyzed by varying the anodizing potential in the range of 15-25 V keeping the temperature constant at 3°C . The top surface FESEM images of AAO films at 3°C are presented in Fig. 3.7 whose anodization was carried out at 15, 19 and 25 V. It is evident that the pores formed at 15 V are irregular in shape. We note that such irregular pore shape is maintained at 15 V at other bath temperatures (see Fig. 3.2). An improvement in pore ordering was visible upon elevating the anodizing potential to 19 V. Keeping other parameters constant, the further increase in potential to 25 V, almost perfectly ordered hexagonal arrays are observed. With the increase in potential, the pore ordering and the interpore spacing were found to increase, whereas, the pore density showed descending order. The calculated pore size and the spacings were 18 nm (44 nm), 23 nm (52 nm) and 29 nm (64 nm), at 15, 19 and 25 V respectively. The pore regularity, periodicity, and correlations among pores were further ascertained from the 3D FFT analysis of FESEM images of AAOs. For these 3D-FFT analyzes, an area of $1.16\mu\text{m}^2$ was selected.

Figures 3.7 (b),(d) and (f) represent the 3-D FFT plots of AAO films corresponding to Fig. 3.7 (a), (c), and (e), respectively prepared at different anodizing potentials. It can be seen from Fig. 3.7 (b) and (d) that a ring structure is formed at 15 and 19 V. This ring structure is a representation of poor ordering (Li et al. 1999) among pores. The domains are of short range with non-sharp boundaries. This is consistent with the analysis done by Sulka et al. (2002) where the ring structure has appeared at 17 and 21 V. The inverse of the ring diameter represents the inter-pore distance between two nanopores. It is also seen in Fig. 3.7 that the ring diameter is decreasing with increasing anodizing potentials. It corroborates with the fact that the inter-pore distance increases

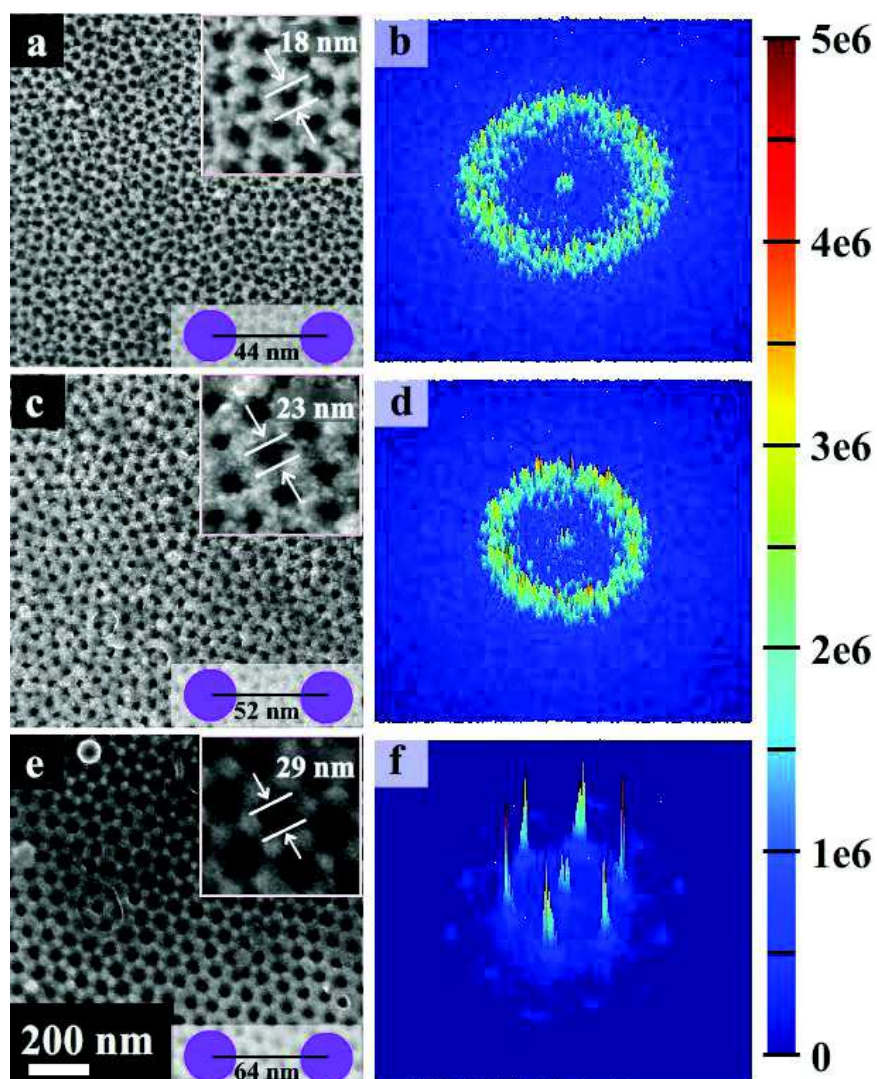


Figure 3.7: FESEM micrographs and 3D FFT images of AAO thin membranes prepared at 3 °C for voltages of (a,b) 15 V, (c,d) 19 V and (e,f) 25 V.

with increasing anodizing potential which corroborates previous investigations (Jessen-sky et al. 1998, Belwalkar et al. 2008). It can also be seen from Fig. 3.7 that the peaks in the ring structure become intense and narrower with an increase in anodizing voltage. This interprets that the size of the ordered domains increases with increasing anodizing potential. There are six distinct high-intensity peaks formed at 25 V, as shown in Fig. 3.7(f). Also, these six peaks are arranged in the form of a hexagon, which represents the formation of the hexagonal lattice by the nanopores. The high intensity of these peaks shows that this hexagonal lattice is uniformly repeated in the nanostructure. Thus, the best regularity of nanopores was obtained at 25 V in H_2SO_4 medium. According to this results, then the effect of anodization bath temperature is also described in section 3.4.2 for anodizing Al at 25 V.

3.4.2 Effect of Temperature

The influence of electrolyte temperature on pore ordering was also investigated by varying the temperature in the range 1 to 15 °C during two-step anodization of aluminum in H₂SO₄ employing anodization voltage constant at 25 V. Top-view micrographs of porous alumina membrane and their corresponding 3D-FFT images examined at various bath temperatures are shown in Figure 3.8 (a, b) 1 °C, (c, d) 3 °C, (e, f) 7 °C, (g, h) 10 °C, and (i, j) 15 °C, respectively. The highest ordered pore arrangement with a domain size of $\sim 1\text{-}2\ \mu\text{m}$ was obtained at 3 °C, however, on either side of this temperature the scale of pore ordering was found to be deteriorated. At higher temperatures, a gradual decrease in ordered pore domain size was observed associated with the dissolution at the pore edges. Such etched pore walls are indicated by drawing an arrow in Fig. 3.8 (i). Previously, Li et al. (1998) suggested that the ordered domain growth in anodic alumina film is a linear function of time and temperature as described by an empirical formula, $R = Bt^n$, where B is the temperature dependent parameter and n is about 0.5-0.4. However, later Almasi et al. (2005) showed that such linear relation is not valid at higher electrolyte temperatures in an oxalic acid medium. They found an increase in domain size from $0.5\ \mu\text{m}^2$ to $4\ \mu\text{m}^2$ as a linear function of bath temperature (i.e., for 0 to 17 °C) and at above 20 °C a drastic reduction in pore ordering and the domain size is reported. Our results of non-linear domain growth in H₂SO₄ medium with the highest pore ordering at 3 °C in the temperature range 1 to 15 °C corroborates the previous observation by Almasi et al (2005).

For detailed analysis and comparison of spatial order of the nanopores, the 3D-FFT images from a $1.16\ \mu\text{m}^2$ segment of the samples were evaluated and one presented in Fig. 3.8 (b), (d), (f), (h) and (j). A continuous ring pattern with reduced intensity of the peaks as can be seen in Fig. 3.8(b) at 1 °C represents disordered pore pattern. On the other hand, at 3 °C, a clear distinct six spots with sharp intense peaks demonstrates the formation of hexagonal array of pores with a long range order. Such six-fold symmetry as shown in Fig. 3.8(d) also signifies about the higher order configuration of the pore arrangement with larger domain size. At 7 °C, still the six-fold symmetry in pore arrangements exists with the appearance of six distinct larger spots but with reduced intensity in the 3D-FFT pattern (Fig. 3.8 (f)). This reduced spot intensity signifies shrinking of the domain size. On further increase in temperature to 10 °C, a relatively disturbed hexagonal symmetry (i.e., nearly a ring shape) is observed as shown in Fig.3.8(h) which could be attributed by the reduced domain size. A similar situation was observed at 15 °C (Fig. 3.8(i)) with reduced hexagonal domain size and uneven pore opening. We note that the hexagonal symmetry in pore arrangement has not been completely wiped

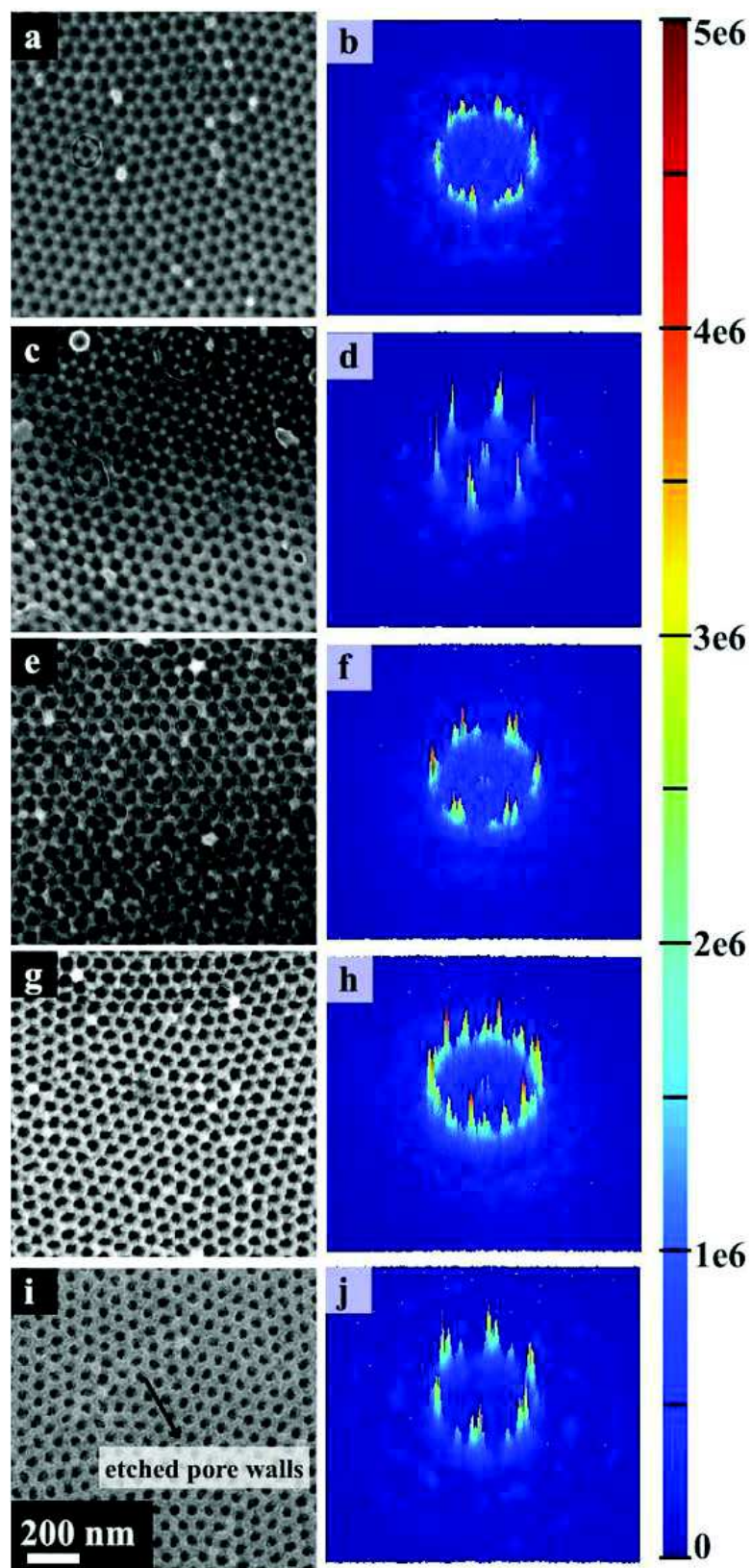


Figure 3.8: FESEM micrographs and 3D FFT images of AAO thin membranes prepared at 25 V for bath temperatures of (a,b) 1 °C, (c,d) 3 °C (e,f) 7 °C, (g,h) 10 °C, (i,j) 15 °C.

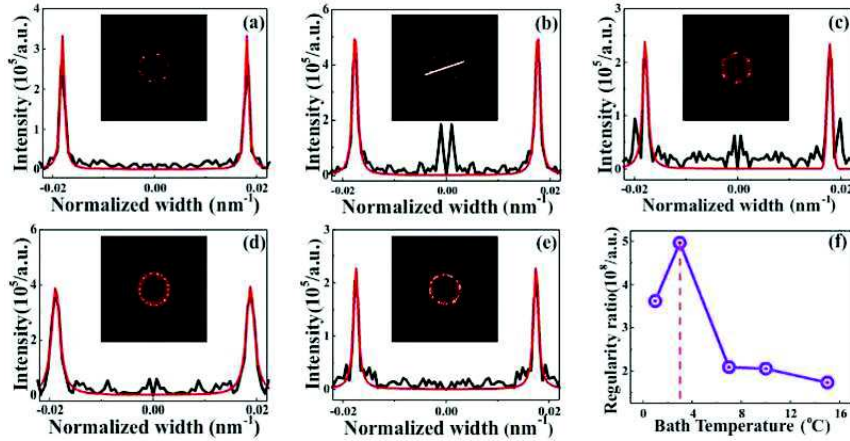


Figure 3.9: Intensity profiles of line scans drawn on AAO surface using 2D FFT images (inset) for 25 V and (a) 1 °C, (b) 3 °C, (c) 7 °C, (d) 10 °C, (e) 15 °C. (f) Variation of pore regularity ratio for different bath temperatures.

out with an increase in temperature till 15 °C. It clarifies that the self-order nature of pore formation up to first neighbor is very little affected by the electrolyte temperature at a given anodization voltage of 25 V. However, the long range order with respect to the repetition of hexagonal pattern, which is nothing but the domain size, is definitely perturbed with the variation of temperature.

For further investigations, we have also evaluated the regularity ratio from the line profile across the hexagonal symmetry of 2D-FFT images. Here, the regularity ratio is defined as the ratio of the maximum spot intensity H_{max} to its full width at half-maximum (FWHM) $W_{1/2}$. Figure 3.9 (a-e) shows the intensity profile along a direction between the two symmetric spots across the center in the 2D FFT image (shown as an inset of Figure 3.9 (b)). The calculated spatial order parameter or the regularity ratio $H/W_{1/2}$ is plotted as a function of the electrolyte temperature in figure 3.9(f).

3.5 SURFACE ROUGHNESS OF SELF-ORDERED POROUS AAO MEMBRANE

In addition to this, the surface roughness of these alumina films using AFM is also analyzed. The films are prepared at the various temperatures from 1 to 15 °C by two-step anodization at 25 V in 0.3 M H_2SO_4 . Figure 3.10 shows the 2D and 3D surface topographic images of the alumina films. Figure 3.10(f) shows the corresponding variation of RMS roughness of the template as a function of bath temperature. The RMS roughness was found to increase monotonously with an increase in temperature from 1 to 15 °C unlike regularity ratio with a peak at 3 °C (Fig. 3.9(f)). This observation is contradictory to previous investigations by Sulka et al. (2007) where they obtained

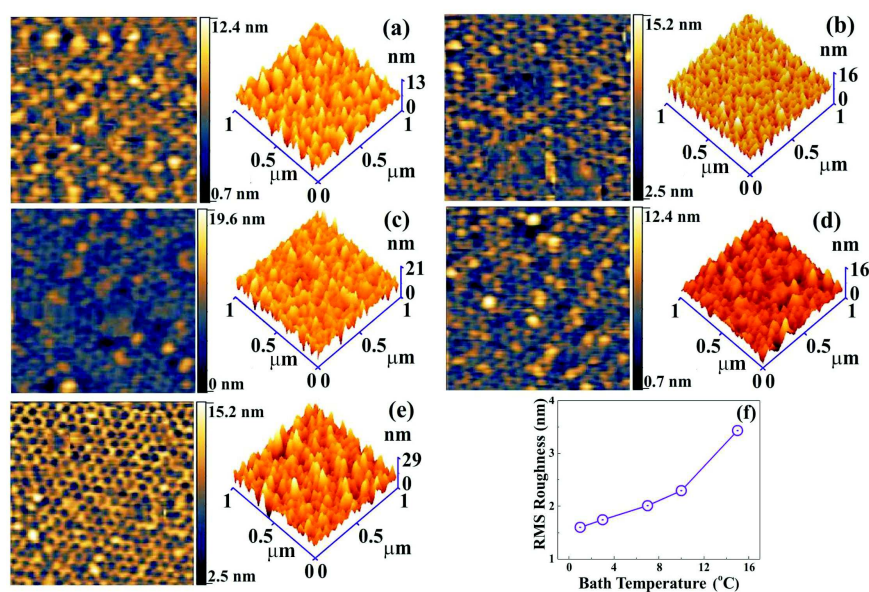


Figure 3.10: AFM surface topography images (2D and 3D) of AAO films prepared at 25 V and bath temperatures of (a) 1 $^{\circ}\text{C}$, (b) 3 $^{\circ}\text{C}$, (c) 7 $^{\circ}\text{C}$, (d) 10 $^{\circ}\text{C}$, (e) 15 $^{\circ}\text{C}$. (f) Variation of RMS roughness with bath temperature.

lower surface roughness with increasing bath temperature with the help of FESEM micrographs. However, we need to point out that AFM is a better technique for measuring the surface roughness accurately than FESEM. Of course, our findings corroborate a previous observation of obtaining higher roughness in AAO template prepared in oxalic acid medium Sulka et al. (2009). This kind of surface roughness enhancement at higher temperature is attributed to the higher rate of alumina template formation as well as the rapid dissolution of an oxide layer. Since high temperature favors both oxidation as well as dissolution kinetics resulting into the uneven surface at the top layer of the template. We note that the variation of pore regularity ratio and RMS roughness are not incommensurate with temperature. The reason is that the pore regularity ratio is a correlation parameter with respect to the arrangement of neighboring pores and extension of lattice size, however, surface roughness measured peak to valley height distribution across the surface. Now, with an increase in temperature the average pore diameter increases, which in turn reduces the overall fraction of pore separation. This is indicated as peak regions in 3D view of AFM. This process effectively, with an increase in temperature, increases the overall peak-valley height differences in addition to contribution from rapid dissolution which results into higher surface roughness.

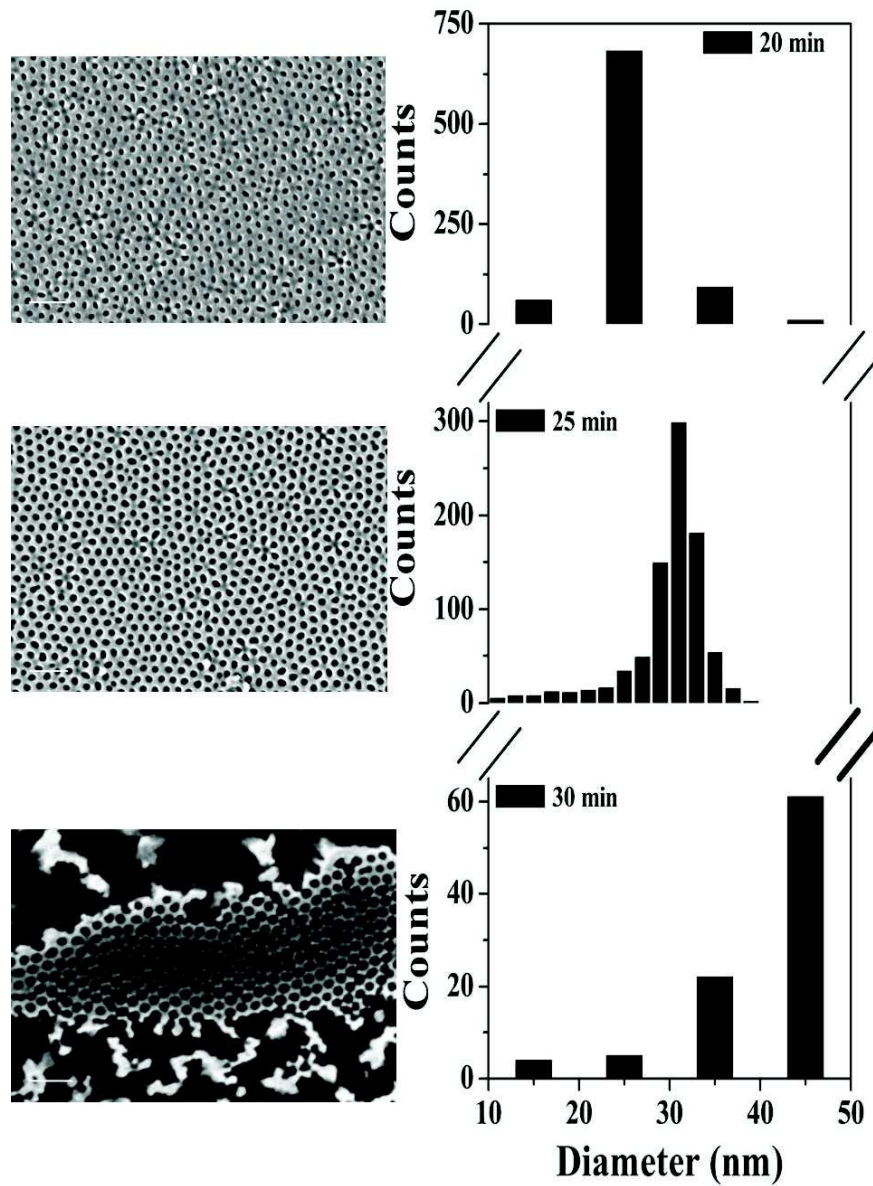


Figure 3.11: FESEM image of AAO membrane after widening the pores in H_3PO_4 solution at RT for 20 to 30 min, images are having the scale bar of 200 nm. The corresponding pore size distribution is shown in the right column.

3.6 BARRIER LAYER REMOVAL AND TUNING THE PORE WALL THICKNESS

The most critical step in the fabrication of AAO is the pore opening while removing the barrier oxide layer by a wet chemical process. As described in Chapter 2, H_3PO_4 acid is used to etch the cap alumina layer. This process is time-consuming and depends mainly on etchant concentration, temperature and the uniformity of the barrier layer (locally). At first, it dissolves the oxide layer to thin the barrier alumina from the center of the hemisphere structure (Lillo et al. 2009). Once the pore is initiated with the thin barrier layer then the migration of solution inside the pores will induce isotropic chemical etching throughout the alumina film, i.e., simultaneous etching of the inner pore walls and the exposed AAO surface kept inside the etchant bath. Therefore, pore size is possibly tuned by controlling the etching rate and time in this wet-chemical process, without affecting the pore density (N) and I_p . The samples used here are prepared by the self-ordered porous AAO membrane at 25 V and 3 °C in H_2SO_4 .

Figure 3.11 shows FESEM images of bottom AAO membrane with different etching time, i.e., 20 to 30 min at room temperature. In this figures, it is clear that the initiation of pore opening without barrier layer was observed at 20 min of H_3PO_4 etching time with average pore size of 25 nm. Whereas, further continuing the process leads to widening the pore size to 35 ± 4 nm for 25 min and 45 ± 4 nm for 30 min. The honey-comb network structure is almost destroyed in the surface while etching the alumina for 30 min, which sets the upper boundary limits in the etching time. Therefore, the porous AAO membranes are etched for the time interval of 20 to 28 min to produce 25 to 45 ± 4 nm pore size.

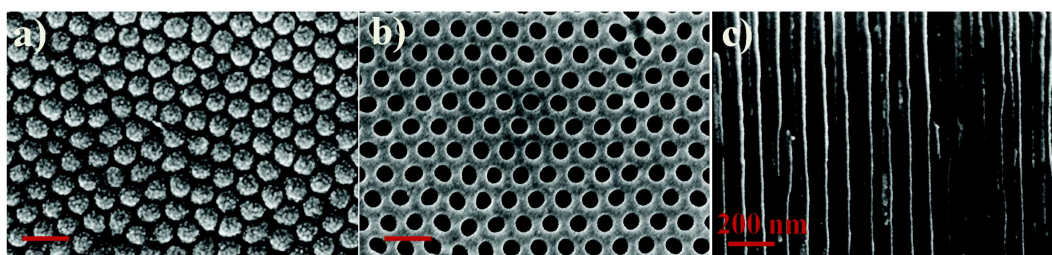


Figure 3.12: FESEM image of AAO membrane prepared by 0.3 M $\text{C}_2\text{H}_2\text{O}_4$ at 40 V, 10 °C: a) bottom, b) top, and c) cross-section view. The scale bar is 200 nm.

3.7 ANODIZATION UNDER OXALIC ACID BATH

Similar to this, highly ordered porous AAO membrane was also prepared by using oxalic ($\text{C}_2\text{H}_2\text{O}_4$) acid at different anodization potentials and bath temperatures. The parameters for optimized conditions had been already carried out in this laboratory before

my joining as a Ph.D. scholar. The preparation steps followed in the optimum conditions of AAO membrane were tabulated in table 3.2 for anodizing Al in both oxalic and sulphuric acids.

3.7.1 Optimum conditions and discussions

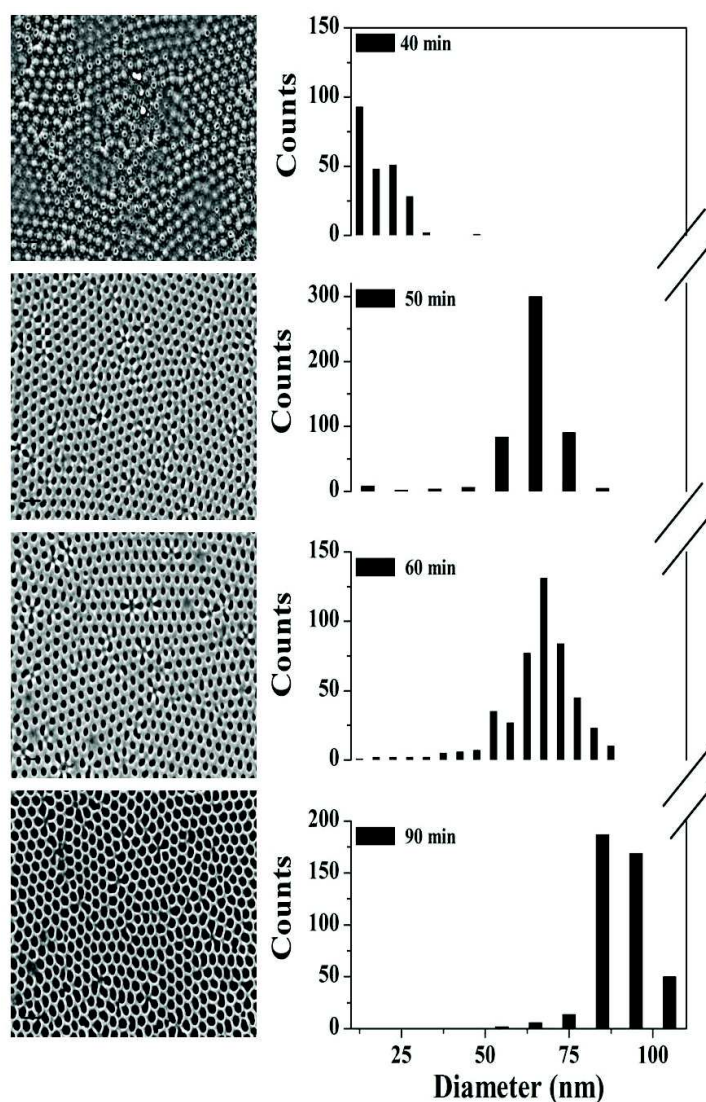


Figure 3.13: FESEM image of AAO membrane after widening the pores in H_3PO_4 solution at RT for 40 to 90 min, images are having the scale bar of 200 nm. The corresponding pore size distribution is shown in the right column.

Porous alumina membrane with hexagonally ordered nanopore arrays was prepared using a two-step anodization of Al in an electrolyte using 0.3 M $\text{C}_2\text{H}_2\text{O}_4$. Figures 3.12 (a-c) show the surface morphology of the porous films with bottom, top and cross-section views respectively. For $\text{C}_2\text{H}_2\text{O}_4$ electrolyte, the pore diameter was 40 nm when

anodized at 40 V, and then it can be tuned to till 100 nm by the wet-chemical process as described in section 3.8. Figure 3.13 show the process of barrier oxide layer removal at different etching time. Moreover, while comparing the pore geometry with the one prepared in H_2SO_4 electrolyte, we observed that the pore parameters, such as, the inter-pore distance (I_p) became higher (~ 110 nm), and the pore density (N) are decreased (40 V, see section 3.3.1). During the anodization of Al in $\text{C}_2\text{H}_2\text{O}_4$, the alumina growth rate was found to be 1 nm/s, as reported by several authors. This is correlated with the aggressiveness of the acids which have different growth rates, such as $\text{H}_2\text{SO}_4 > \text{C}_2\text{H}_2\text{O}_4 > \text{H}_3\text{PO}_4$ (Sulka et al. 2008).

Table 3.2: Optimum conditions for self-ordered AAO membrane.

Anodization conditions	Electrolyte		Remarks
	H_2SO_4	$\text{C}_2\text{H}_2\text{O}_4$	
Applied voltage	25 V	40 V	
Bath temperature	3 °C	10 °C	
Electrolyte concentration	0.3 M	0.3 M	
Pre-cleaning	30 min	30 min	Removal of surface impurities
1 st step	10 hrs	10 hrs	For large domain size $\sim 1-2 \mu\text{m}^2$
Removal of Al_2O_3	30 min at 60°C	45 min at 60°C	To achieve highly ordered pre-texturing on Al surface
2 nd step	20 s to 2 hrs	75 s to 2 hrs	Highly orderd hexagonal pore arrays
Al removal	30 min at RT	30 min at RT	Free-standing AAO membrane
Pore-widening time	20-30 min at RT	45-90 min at RT	For barrier layer removal and pore wall etching
Pore size D_p	22-45 nm	40-100 nm	
Inter-pore distances	65 nm	110 nm	

3.8 SUMMARY

- Highly ordered pore arrangement of ultra-thin alumina membrane (UTAM) were successfully fabricated by using two different acids (H_2SO_4 and $\text{C}_2\text{H}_2\text{O}_4$), via two-step anodization processes. The present study clearly showed systematic variation of pore regularity, pore diameter, inter-pore distance and porosity in alumina template with the variation of temperature in H_2SO_4 anodizing medium. The largest self-arranged pores of ordered domain size were obtained as 1-2 μm .
- The pore diameter and top surface roughness were increased with the increase in temperature due to temperature assisted dissolution of alumina pore walls as well as a top porous layer. However, the inter-pore distance remained unaffected within the temperature range studied here.
- The variation in the pore diameter with respect to the pore widening time were optimized for porous AAO membrane with two different interpore distances.

Chapter 4

FABRICATION, STRUCTURAL AND MAGNETIC PROPERTIES OF COBALT NANOWIRE ARRAYS

Magnetic cobalt nanowire arrays are grown via electro-deposition process through the pores of porous AAO membrane, which are described in the previous chapters. These nanowires are grown electrochemically using Chrono-amperometry with two different conditions: (i) pulse-deposition (frequency, $f=25$ Hz and $T_{ON} = T_{OFF} = 20$ ms) with the pulse height of 2 V (0 to -2 V) and (ii) continuous deposition at -1.1 V, respectively. The structural evaluation and the corresponding $M(H)$ loops behavior are characterized with varying their size (diameter, length) and inter-wire spacings. It is found that the presence of crystalline phases (Co: fcc/hcp) are highly influenced by the diameter and the pH of the electrolyte, whereas for some cases, the length of the wire leads to tuning the Co texture from one phase to other. Therefore, this study is involved by the influence of Co nanowire arrays with its crystalline phases and their magnetic reversal processes. At first, growth of Co nanowires with bi-layer texture (ie., hcp (002) and hcp (100) phases) is demonstrated for larger pore diameter (~ 70 nm) and fcc (111) phase for nanowires of the diameter of 45 nm, respectively. Among these crystalline phases of Co, the Co hcp (002) phase is performed particularly to investigate the magnetostatic interaction between the nanowires in an array as a function of diameter and inter-wire separations. The geometry of the nanowire (i.e., size, shape and interwire separation) is controlled by the selected AAO membranes which has a pore size (cell size) of 25-45 nm (66 nm), and 50-80 nm (105 nm), respectively. During this investigation, independent to the pore geometry, a pH dependent (~ 6.7) growth is performed to obtain Co hcp (002) phase. In this chapter, the summarized results of the magnetic properties of the highly ordered Co nanowire arrays as a function of diameter, length, inter-wire spacings and the presence of crystalline phases are discussed.

4.1 MAGNETIC Co NANOWIRE ARRAYS

Recently, the physics of magnetic nanowire (NW) array has attracted great attention due to the easily accessible route of electrochemical deposition through anodic aluminum oxide (AAO) template (Henry et al. 2001, Darques et al. 2004, Zhang et al. 2007, Kartopu et al. 2008, Sánchez-Barriga et al. 2009, Maaz et al. 2010, Ahmad et al. 2011,

Vivas et al. 2012 Vivas et al. 2012). The main advantages in this bottom-up technique are; AAO template can be fabricated with varying pore diameter, length, density and periodicity, by simply changing the processing parameters, such as anodizing voltage, electrolyte, and electrolyte temperature (Li et al 1998, Nielsch et al. 2002), as mentioned previously in Chapter 3. Therefore, the geometry (i.e., size and shape) of the magnetic nanowires is controlled by filling with pores in porous alumina membrane via electrodeposition processes (García et al. 1999, Henry et al. 2001, Zhang et al. 2007 Kartopu et al. 2008, Maaz et al. 2010, Vivas et al. 2011). At first, we define the magnetization terms which contribute in the resultant magnetization behaviour of the magnetic nanowire arrays, such as the magnetic anisotropy and the static interactions between the neighboring wires. The magnetic anisotropies are classified into three components such as shape, magneto-crystalline and magneto-elastic. Here, the shape is determined by the geometry of the material and other two are the intrinsic property of the material. The static interaction is extrapolated by the geometry of the nanowires and their periodicity in an array with respect to applied field direction (H_{ext}).

For large aspect ratio ($\tau \gg 1$) nanowires, the resultant magnetic anisotropy is primarily determined by the shape anisotropy (K_{shape}), which leads to longitudinal (out-of-plane) magnetic anisotropy (along L). It is also well known that this shape anisotropy is originated by the demagnetization factor (N_d) present in the nanostructure. Apart from the shape anisotropy, other anisotropies such as magneto-crystalline anisotropy (K_{ma}), magneto-elastic anisotropy ($K_{elastic}$) may also affect the resultant magnetic behavior in nanowires. The K_{ma} is originated from the spin-orbital interaction in subatomic level, whereas microscopically, it has been related to the atomic structure of a crystal that introduces preferential directions for the magnetization i.e., the tendency of the magnetization to align itself along a preferred crystallographic direction. The preferred crystallographic directions for Fe is body-centered cubic (bcc) structure with (100) direction as its easy axis (Henry et al. 2001). Similarly, the magnetization for Ni is aligned along the (111) the direction of face-centered cubic (fcc) structure (Pan et al. 2005, Kartopu et al. 2008), and Co material has two different crystalline phases, such as, hexagonal-close-packed (hcp) and fcc structures. Then, the preferred directions are observed to be either (100) or (002) for hcp Co and (111) for fcc Co structures (Armyanov et al. 2000, Zhang et al. 2007, Ye et al. 2009). The change in the crystalline phases of Co in the nanowire arrays and the resultant behavior of magnetization is discussed later in this chapter. In addition to this, the $K_{elastic}$ anisotropy arise from the effect of magnetostriction due to the influence of stress or strain on the magnetic material during growth or by the magnetization processes.

At the same time, the magnetostatic interaction is also contributing in the resultant

magnetic behavior which originates from long-range dipole-dipole interaction between the neighboring nanowires in arrays. The term interaction will have an average effect of the overall energy transfer (relaxation) through mutual exchange between the neighboring particles or the wires. This static interaction is similar to the exchange interaction between the nanocrystalline particles. However, the exchange interaction phenomena are observed to be a short range interaction (Armyanov et al. 2000) (i.e., it can be negligible if particles are separated by a distance higher than 10-20 Å), and the static interaction is for long-range interaction between the array of nanoparticles. Therefore, understanding of the magneto-static interaction has been trivial interest among the researcher in magnetic nanoarrays. In general, it is complicated by the fact that the dipolar fields depend on the magnetization state of each element, which, in turn, depends on the fields due to adjacent elements. Therefore, initial studies are performed based on the preparation of single nanowire or keeping the inter-wire separation higher than twice the diameter of the nanowire (\sim few μm). This helps to investigate the nanosize effect of magnetic nanowires without any interaction from the neighboring magnetic nanowires in an array. In this case, at the earlier stage, the ion track etched polycarbonate porous (PC) membrane with poor pore ordering and large interpore distances (\sim 1 μm) is utilized to study the single nanowire properties. However, the last couple of decades, porous AAO membrane is used for the growth of nanowire arrays due to the uniformity and high density within the easy processing steps. In which the interpretation for the fundamental issues on magnetization properties of magnetic states and the reversal mechanisms in magnetic nanowires are focused.

Among different magnetic nanowires such as Fe (Escrig et al. 2008), Co (Darques et al. 2004, Xu et al. 2005, Wang et al. 2007, Kartopu et al. 2008), and Ni (Goolaup et al. 2005, Escrig et al. 2007) studied so far, Co nanowires were investigated extensively as Co is a hard magnetic material and its magnetic properties depend on several factors, such as crystal orientation, phase, and grain size. In hcp Co phase, the magnetization easy axis, originated from the magnetocrystalline anisotropy, lies along the direction of crystallographic c-axis. Therefore in hcp Co, the easy axis is \parallel to nanowire length for (002) phase and in the case of the phase of (100), it is aligned \perp to nanowire length. As discussed earlier, for 1-D magnetic nanowires, the contribution of two major anisotropies, namely; the shape and the magnetocrystalline anisotropies are determining the magnetic properties of the system. In this case, Co nanowires grown with hcp (002) phase, the magnetocrystalline anisotropy enhances the longitudinal anisotropy; whereas in the case of hcp (100), this reduces the effective anisotropy. Normally, the hcp phase of Co is preferred in data recording systems because it exhibits significantly

higher magnetic anisotropy and hence is capable of delivering potentially higher coercivities.

Most of the structural investigations on electrodeposited magnetic Co nanowires were observed to have the polycrystalline structure (Yang et al. 2000) but the textured growth of Co nanowire array with hcp phases was reported recently (Henry et al. 2001, Darques et al. 2004, Xu et al. 2005, Zhang et al. 2007, Han et al. 2009, Maaz et al. 2010). The crystalline orientation with respect to the nanowire axis has been fabricated by adjusting the electroplating conditions, such as pH, plating current, and bath temperature (Henry et al. 2001, Zhang et al. 2007, Vivas et al. 2011, Pirota et al. 2011). This leads to influences the magnetic anisotropy in many ways (Wang et al. 2007, Han et al. 2009, Ren et al. 2011, Vivas et al. 2012) and provide an added advantage to tune the anisotropy of the system for spintronic applications.

In addition to this, the pore diameter modifies crystalline structure of electrodeposited Co nanowires. fcc Co (111) phase was found to grow when D_p is below 50 nm (Pirota et al. 2011, Vivas et al. 2011) due to the lower surface energy of the fcc phase present during the deposition. Moreover, recent studies are shown with the change in the crystallographic phases as a function of both length and diameter. Very recently, Pirota et al. (2011), and Vivas et al. (2011) are shown the reduction in the magnetic coercivity (H_c), squareness (M_r/M_s) as a function of the length of nanowires (L). This have been demonstrated by the change in crystalline structure from the fcc to hcp Co phases during electro-deposition through pores of 35 nm. In this case, the critical length of fcc Co phase was estimated around 260 to 270 nm, as evidenced from both structural (XRD) and magnetic behaviour ($M(H)$ loops: VSM). Whereas, in the case of varying the diameters; 35 to 70 nm, Vivas et al (2013) reported the change in crystalline phases from fcc Co (111) to hcp Co (100) for the arrays of Co nanopillars with 120 nm height. Importantly, the resultant magnetization processes in these Co nanowires are illustrated with different reversal magnetization process by using the micromagnetic simulations.

These studies have shown growing research interest to understand the mechanism behind the remagnetization processes of magnetic Co nanowire arrays (Han et al. 2003, Han et al. 2009, Sánchez-Barriga et al. 2009, Yang et al 2010, Vivas et al. 2011, Ren et al. 2011, Vivas et al. 2012). Based on the above literature, it is found that the understanding of the reversal mechanism for different crystalline Co phases is not well established for an array of nanowires and their micromagnetic simulation studies. Additionally, the investigation based on the magnetostatic interaction is also limited only with varying the diameter within the cell structure of the porous alumina membrane. However, in this study, we investigate the magnetostatic effect of Co nanowire arrays grown through two different cell size with nearly equal pore diameter.

It is known that understanding of the reversal magnetization processes for 1-D magnetic nanowire arrays are complicated due to the competition between the shape anisotropy, magnetocrystalline anisotropy, and the magnetostatic exchange interactions between the neighboring wires (Han et al. 2003, Vivas et al. 2011). Therefore, in this Chapter, we describe the growth of magnetic Co nanowire arrays as a function of geometry (diameter and length, i.e., shape) in a controlled electro-deposition process via potentiostat mode using pulse dc- and continuous deposition processes. This leads to control the crystalline phase of Co during the growth as mono- and bi-layer textures, i.e., for magneto-crystalline. In addition to this, particularly the magnetostatic interaction is also studied for Co hcp (002) crystalline phase by varying the pore density of porous AAO from $(0.8-2.25) \times 10^{10}$ per cm^2 area, respectively.

4.2 MECHANISM OF Co DEPOSITION INSIDE NANOPOROUS MEMBRANE

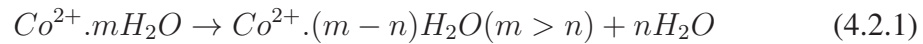
The electrochemical behavior of the nanoelectrode system is quite different than the bulk electrode for the synthesis of Co nanowire arrays, and still, it is a great challenge to understand the growth kinetics inside the nanoporous electrode (Valizadeh et al. 2001). Basically, the oxidation or reduction of the electrochemically active species does lead to the current flow in the electrode reaction, i.e., the current flow is limited by the diffusion rate. For bulk case, the electrode geometry has a significant effect in the diffusion rate, i.e., time dependent and independent current flows after applying the potential steps. In this view, the time-dependent current flow obey the Cottrell equation for planar electrodes, (i.e., $i \propto \frac{1}{\sqrt{t}}$, no steady-state current is achieved) (Bard et al. 2008), whereas, the hemispherical diffusion conditions exist with steady-state current flow in spherical (micro-) electrodes and obey the Cottrell equation when $r_0 \rightarrow \infty$ (i.e., r_0 is the radius of the spherical electrode) (Brad et al. 2008). However, for nanoelectrodes (i.e., inside the nanochannels of the porous PC membrane), the diffusion nature has explicated and characterized by two types of diffusion regimes (Pletcher et al. 1991): (i) time-dependent diffusion that appears as linear or Cottrell diffusion for short time, and (ii) the gradually increasing radii of spherically shaped diffusion zones from each recessed nanoelectrode, result in the overlapping of diffusion zones at a longer time, which leads to a constant steady-state current as diffusion controlled limiting current (Valizadeh et al. 2001) during the synthesis of Co nanowires. Additionally, Valizadeh et al. (2001) also showed the existence of microscopic concentration variations between mouth and vicinity of the recessed nanoelectrodes. This leads to steady-state current density by reducing the diffusion length while depositing inside the pores, i.e., $j_{pore} \propto \frac{1}{L}$ (Schlorb et al. 2010). Therefore, it is also mentioned that the ion concentration may

modify when the thinner membrane is used. In this Ph.D. work, we used porous AAO membrane with thickness of $\sim 3\mu\text{m}$ to synthesise Co nanowires potention-statically.

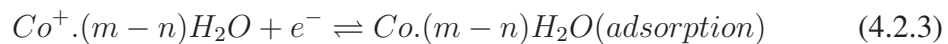
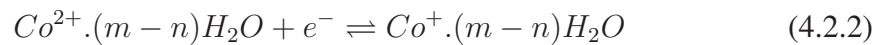
In addition to this, Cao et al. (2006) have proposed a current assisted growth mechanism, which plays an important role in controlling and designing of metallic nanostructures (nanowires/nanotubes) inside the pores of porous alumina membrane. This is considered by the competitive growth rates for metal atoms entering the crystal lattice, i.e., V_{\parallel} and V_{\perp} , at where growth rate is parallel and perpendicular to current direction, respectively. Metal (Fe, Ni, Co) nanowires can be obtained at $V_{\parallel} \approx V_{\perp}$ while applying low current density, whereas nanotubes can be obtained at $V_{\parallel} \gg V_{\perp}$ with high current density (Cao et al. 2006). Accordingly, Narayanan et al. (2008) also followed the same to describe the mobility assisted formation of nanowires and nanotubes, while keeping the voltage constant.

However, the growth mechanism in a porous material initiates with metal atom absorption at the bottom edge of the pore, which is energetically favorable due to the reduced coordination number and high surface area, i.e., the effective cathode surface area. When negative potential is applied to the working electrode, divalent metal ions (Co^{2+}) are surrounded by the hydration layer and move towards the cathode, which are then reduced as Co. Moreover, the reduction process of Co^{2+} ions in the electrodeposition solution consists of three steps, as described below:

(i) The hydration number of Co^{2+} ions decreases initially, and then Co^{2+} ions are rearranged in solution near the cathode surface,



(ii) Further reduction in Co^{2+} ions are observed from the surrounding water molecules, as a step-by-step process shown in Eqns. 4.2.2-4.2.3,



(iii) The final step is that the adsorbed Co atoms discard the surplus hydration layer, and enters into the crystal lattice,



However, the electro-crystallization of Co deposition is a complex phenomenon; at

which Co has an hcp structure and cubic (fcc) structure at room temperature, whereas bulk Co, has an fcc structure above 422 °C at ambient pressure. This structural transitions in electrodeposition have been observed by several ways, such as, (i) the presence of Co concentration in the electrolyte (Henry et al. 2001, Darques et al. 2004, Ren et al. 2011, Vivas et al. 2012), (ii) added additives to the electrolyte, (iii) variation in the pulse frequency (Zhang et al. 2007) or the current density by galvanostatic and potentiostatic deposition in alumina templates, respectively. For example, at low pH (less than 2.5), hydrogen evolution is more active in solution due to a higher concentration of H⁺ ions. This causes heavy adsorption of the hydrogen into the deposited Co during the growth process at room temperature. Hence, the disturbed crystallizes is fcc Co structure, and the structure could be heavily faulted due to the desorption of hydrogen from the deposit. For pH above 6.0, the onset of cobalt hydroxide precipitate is reached due to the interaction of Co²⁺ ions and OH⁻ ions at the cathode. Then, the reduced Co has an hcp structure with the c-axis parallel to the growth direction (along *L*), which is promoted by the presence of such Co-hydroxide layer (Cavallotti et al. 1983).

Moreover, the effect of pore diameter on texture of Co nanowires has also been investigated by several authors (Henry et al. 2001, Darques et al. 2004, Xu et al. 2007, Zhang et al. 2007, Kartopu et al. 2008, Ye et al. 2009, Yang et al. 2010, Maaz et al. 2010). The orientation of the hexagonal c-axis of Co nanowires has been found to change from perpendicular to parallel to the wire axis (Vivas et al. 2013) or to the presence of an fcc Co phase, which is enhanced at small diameters (Darques et al. 2004, Sánchez-Barriga et al. 2009, Pirota et al. 2011), when decreasing the pore diameter below a critical value of about 50 nm (Henry et al. 2001). In both cases, an increase of the uniaxial anisotropy is observed. Still, the origin of the change of crystallographic texture of Co as the wire diameter is varied and left as an opened question. However, it may be related to several reasons, such as; (i) a local increase of pH in the pores of smaller diameter, where the Boric acid could not fully play its buffering action, and (ii) generated stress during the growth of Co deposition due to the constrains in the lateral direction by the pore walls. In this work, the effect of pore diameter and the pH were analyzed by the selected deposition techniques of pulse dc- and chronoamperometry studies for the preparation of Co nanowires into the pores of porous AAO membrane. The deposition conditions of the above-mentioned techniques were already described in Chapter 2.

4.3 PULSE DEPOSITION

The pulsed dc- ($f=25$ Hz, $V = -2$ V and $T_{ON}=T_{OFF}=20$ ms) electrodeposition was performed to fill the Co material inside the pores of nanoporous membrane. The structural

and magnetic properties of Co nanowires were characterized to investigate the influence of the pH of the electrolyte (2 to 6) and the wire geometry. The nanowire length was varied from 25 nm to 4000 nm, whereas the wire diameter was kept in the range from 45 to 70 nm. It is important to mention that the effect of pH was not observed during the pulse deposition. Figure 4.1 show the $M(H)$ loops of Co nanowires prepared as a function of pH, i.e., the as prepared electrolyte solution has pH of 4 and it has been adjusted into 2 and 6 by adding Con.H₂SO₄ and NaOH, respectively. During this investigation, the length of the nanowire is kept constant by controlling the deposition time (i.e., no of sequences in the pulse deposition) and the diameter is also fixed by the pore size of the porous AAO membrane, 70 nm, respectively. In addition to this, the function of wire geometry and the corresponding structural changes during the growth of Co nanowire is tabulated for pH 4 in Table 4.1. and the magnetic behaviors of as deposited Co nanowires as a function of length and diameter are described below:

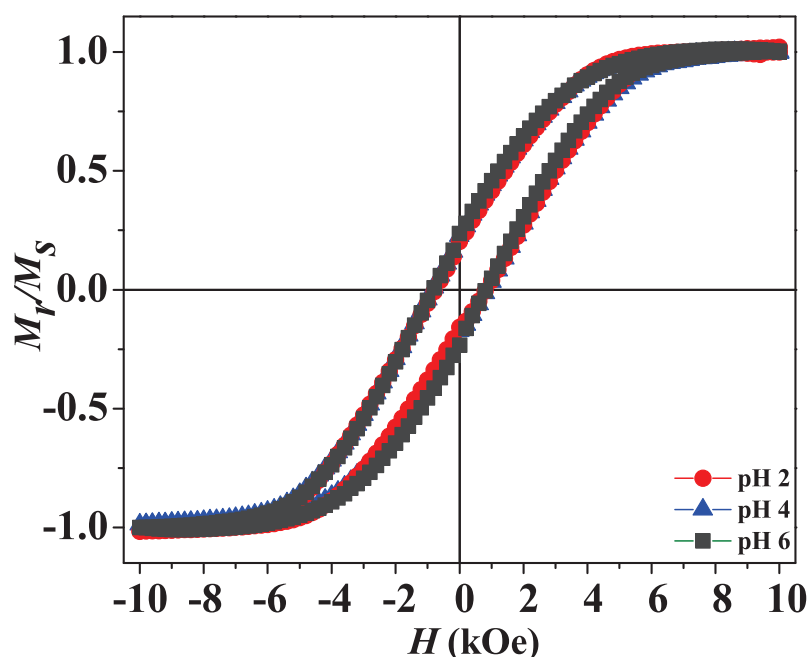


Figure 4.1: $M(H)$ loops of Co nanowires prepared as function of pH 2, 4, and 6, respectively.

4.3.1 Magnetic properties as a function of nanowire length

Figure 4.2(a) shows the FESEM image of AAO membrane with hexagonal pore arrays. The average diameter and interpore distance are estimated as 70 ± 5 nm and 110 ± 5 nm, respectively. The cross-sectional view of AAO membrane with partially filled Co nanowires is shown in Fig. 4.2(b). The average length, L , of nanowires was 1000 ± 20 nm. Figure 4.2(c) presents the XRD patterns for nanowires with varying length from 100 to 2000 nm. As shown in the figure, only one peak is observed at $2\theta = 44.4^\circ$ for the

Table 4.1: Wire geometry and the extracted structural parameters of Co nanowires via pulse dc- technique.

Co nanowires \Rightarrow Mode of \downarrow Electrodeposition	Diameter (D) (nm)	Crystalline phase	Solution pH
Pulse (25 Hz $T_{ON} = T_{OFF}$ = 20 ms)	70	hcp (002); $L < 300$ nm hcp(100); $L > 300$ nm	4
	45	fcc (111); $L < 200$ nm hcp (100) and hcp (101); $L > 200$ nm	

nanowire arrays with $L < 500$ nm, indicating textured growth of Co hcp (002) structure. It is to be mentioned that the XRD peaks corresponding to hcp (002) and fcc (111) Co structures lie within $\Delta\theta = 0.2^\circ$. It is rather difficult to distinguish these two phases from the measured XRD spectra (Zhang et al. 2007, Vivas et al. 2011). But it is reported that the Co hcp structure is more stable than fcc Co at room temperature (Ye et al. 2009). Moreover, the deposition conditions applied here are favorable to the Co hcp growth (Han et al. 2009, Ye et al. 2009, Vivas et al. 2012).

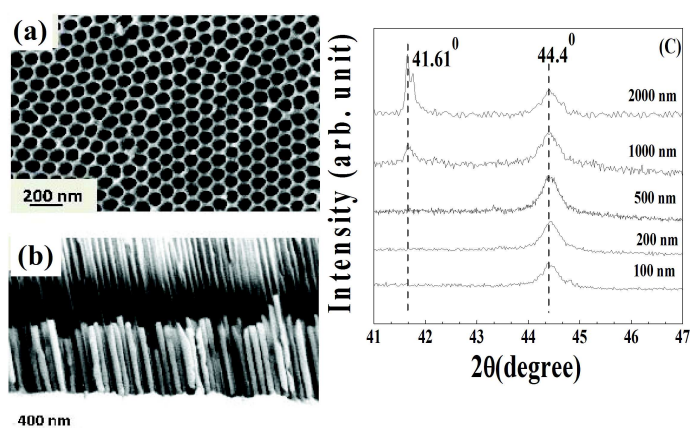


Figure 4.2: FESEM images of AAO membrane (a) top view, (b) cross-sectional view filled with Co nanowires, and (c) X-ray diffraction patterns of Co nanowires with varying length (L) of the nanowires

Interestingly, with increase in length ($L > 500$ nm) of the nanowires, one more peak corresponding to Co hcp (100) appears at $2\theta = 41.6^\circ$ along with the existing hcp (002) peak. In fact, the intensity of (100) peak becomes dominant with further increase in L . Nevertheless, the (002) peak does not vanish but appears as a small hump even at $L = 4 \mu\text{m}$. Therefore, the structural evolution indicates that initially Co grows into the pores with hcp (002) texture up to few hundred nanometers and then the growth orientation changes to hcp (100) as L increases. It is to be mentioned that there might be

an existence of an intermediate region where the mixed state of both textures lies. The quantitative investigation of preferred orientation has been carried out with the help of texture coefficient (TC). For $L=1000$ nm, $T_{(002)}=1.05$, and $TC_{(100)}=0.95$ were reported and decrease in $TC_{(002)}$ to 0.63 was observed when L increased to 4000 nm. This indicates the preferred (100) phase at higher L suggesting diminishing of (002) texture and enhancement in (100) texture with increasing the length (Ye et al. 2009).

4.3.1.1 Magnetic properties of bilayer crystalline texture of Co hcp (002) and hcp (100) structures

Figures 4.3(a)-(e) show the $M(H)$ hysteresis curves measured for the nanowire arrays with different L values: 60, 200, 500, 1000 and 2000 nm, respectively. $M(H)$ data are presented here for the external magnetic fields (H) applied both parallel (\parallel) and perpendicular (\perp) to the nanowire axis at room temperature. Irrespective of the nanowire length, all the samples show their easy axis of magnetization along the axis of the nanowire with decreasing anisotropy field. As shown in Fig. 4.3(f), the variations of both the longitudinal coercivity H_C and the squareness ratio M_r/M_s as a function of L indicates three different regions. In region I, with $L < 300$ nm, the values of $H_C=1.6$ kOe and $M_r/M_s=0.8$ are independent of L . In region II, with $300 \text{ nm} < L < 500$ nm, H_C decreases from 1.6 kOe to 0.9 kOe, but the squareness ratio remains same. In region III (with $L > 500$ nm), the sharp decrease of both H_C and M_r/M_s indicates a reduction in effective longitudinal anisotropy, even with the enhancement of the shape anisotropy.

4.3.1.2 Angular dependence of magnetic coercivity based remagnetization process in bi-layered Co nanowire arrays

The reversal magnetization behavior in magnetic NW array has also performed for better understanding. Therefore, the angular dependence of magnetization with respect to the wire axis was investigated in Co nanowires with three different nanowire lengths, 200, 400 and 1000 nm. There were several reports to quantify the reversal magnetization of nanowires by angular dependence of hysteresis loops, and mentioned as a useful tool (Han et al. 2003, Landeros et al. 2007, Escrig et al. 2008, Lavin et al. 2009, Vivas et al. 2012, Vivas et al. 2012). The measured experimental coercivity (H_c) can be compared with the expected evolution assuming different possible reversal modes, such as coherent rotation (C) in which all the spins rotate simultaneously; transverse rotation (T_r) in which spins rotation takes place via propagation of transverse domain wall; and curling or vortex rotation (V), in which spins are reversing their directions via propagation of vortex domain wall.

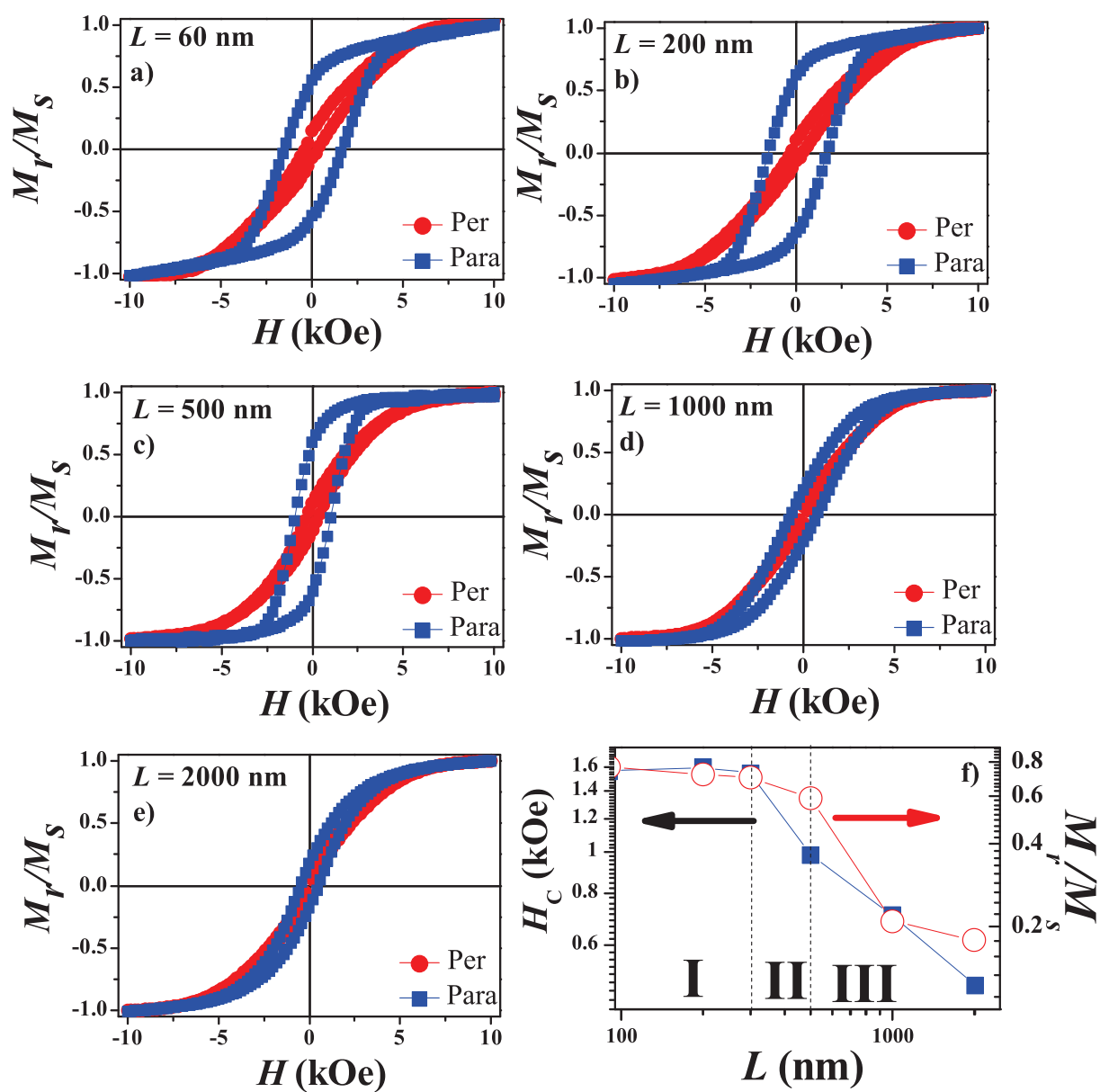


Figure 4.3: Normalized longitudinal (\parallel) and transverse (\perp) $M(H)$ loops of Co nanowire arrays for lengths (a) 60 nm, (b) 200 nm, (c) 500 nm, (d) 1000 nm and (e) 2000 nm. (f) shows the measured H_C and the squareness ratio, M_r/M_s , as a function of nanowire length L .

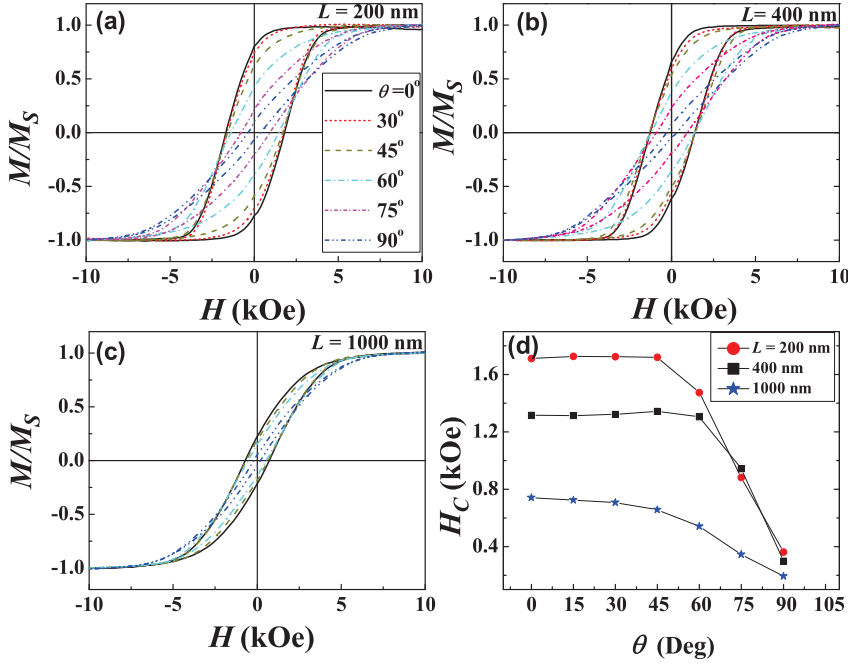


Figure 4.4: Measured $M(H)$ loops of Co NW array for lengths (a) 200, (b) 400, and (c) 1000 nm for different θ values. (d) Shows the measured H_C as a function of θ .

Figures 4.4(a)-(c) present the detailed angular dependence of $M(H)$ hysteresis curves measured for the NW array with three different L values; 200, 400, and 1000 nm, respectively. The $M(H)$ data presented here are measured with varying the angle, θ , between 0° to 90° . Irrespective of the NWs length, the $M(H)$ curves show systematic decrease in hysteresis loops with increasing θ from 0° to 90° and M_r/M_s follows the cosine function of this angle as expected. This indicates that the bulk easy axis arising from both the shape and the magnetocrystalline anisotropies lies along the NWs axis. However, the anisotropy field, H_k ($-H_s^{90} + H_s^0$, H_s is the saturation field), decreases with increasing L , indicating a transformation from an anisotropic to the isotropic system. The variation of H_C as a function of θ for three different wire lengths is shown in Fig. 4.4(d). It is interesting to see that irrespective of the nanowire length, H_C decreases sharply for $\theta > 45^\circ$. However for $\theta < 45^\circ$, the following observations are made: (i) for $L = 200$ nm, H_C is independent of θ , and (ii) for $L = 400$ and 1000 nm, H_C shows upward and downward trends, respectively.

To correlate the structural investigations with experimentally observed magnetic behaviors, we have performed the micromagnetic simulation using the 3D-OOMMF package (<http://math.nist.gov/oommf/>) with keeping the external field in the direction of the nanowire axis. For NWs, with $L = 200$ nm, the structure was considered to be hcp (002)

with the crystallographic *c*-axis in the longitudinal direction. For $L=400$ nm, the texture is defined as two segments along the NWs length; the lower segment of length 300 nm with hcp (002) structure and a mixture of hcp (002) and (100) with an equal percentage for rest of the upper segment. While simulating for $L=1000$ nm, we have considered three different segments: (i) lower segment of length 300 nm with hcp (002) texture, (ii) middle segment of length 200 nm with mixed structure of both hcp (002) and hcp (100), and (iii) upper segment of length 500 nm with hcp (100) structure. The resultant study having a good agreement with the experimental data and details are discussed in Chapter 6.

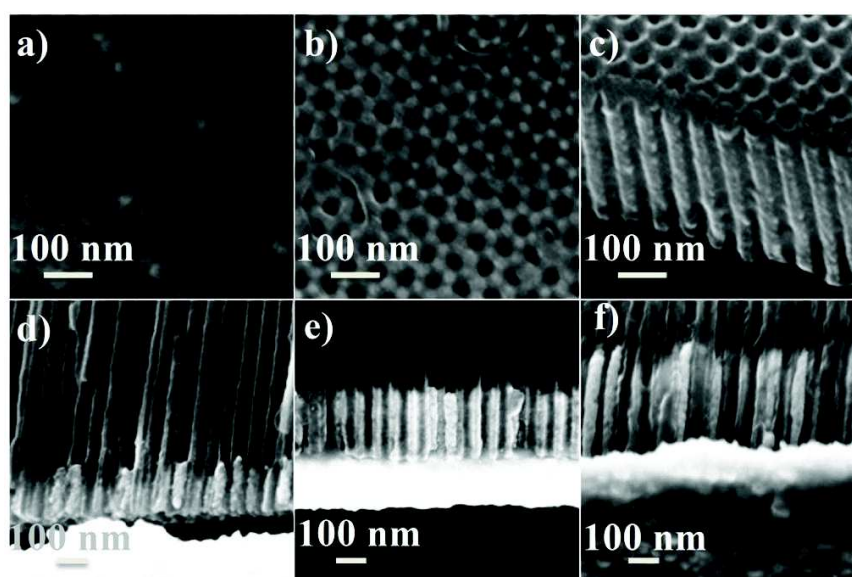


Figure 4.5: The surface morphology of porous anodic alumina membrane (a) bottom, b) top, c) cross-section view. The partially embedded Co nanorod arrays with variable length (d) $L=100$ nm, e) $L=200$ nm and f) $L=400$ nm, respectively.

4.3.2 Magnetic properties as a function of nanowire diameter

Porous alumina membranes with hexagonally ordered nanopore arrays were prepared using a two-step anodization of Al in an electrolyte using 0.3 M of H_2SO_4 . Figures 4.5(a)-(c) show the surface morphology of the porous films with bottom, top and cross-section views respectively. It is also expected that the diameter of the pore should be uniform throughout the channel length, and is shown in Fig. 4.5(c). Pores filled Co nanorod arrays were obtained by a dc pulse deposition technique, hence the growth was found to be uniform throughout the nanochannels. Partially etched porous alumina membranes, which were embedded with Co nanorod arrays, are shown in Figs. 4.5(d)-(f) with different nanorod lengths of 100, 200 and 400 nm, respectively. The diameter of

each Co nanorod was found to be same as the diameter of the nanopore (i.e., $D_p = 45 \pm 5$ nm) in the alumina membrane. It is to be mentioned that, during this investigation, the template with nanopore diameter was kept at a fixed value of 45 ± 5 nm, whereas, the length of the as grown nanorod array was varied from 25 to 400 nm keeping in mind that the aspect ratio (L/D) covers both below and above the unity. To the best of our knowledge, there is no report on the reversible process so far on nanorods with length less than 120 nm. Therefore, it will be interesting to work in this regime due to the following reasons: (i) decrease in aspect ratio leads to an enhancement of shape anisotropy due to geometry effect and (ii) growth of single crystalline structure in lower length regime enables us to see the effect of magnetocrystalline anisotropy against the shape anisotropy.

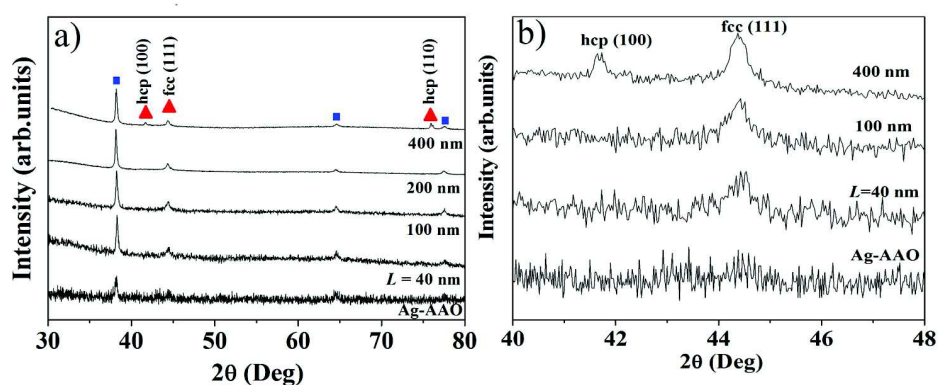


Figure 4.6: the structural characterization of Co embedded porous anodic alumina by X-ray diffractometer, b) Expanded view of XRD plots as a function of the length of the nanorod arrays (symbols: square and the triangle represents the Ag substrate and the deposited Co, respectively).

The recorded X-ray diffraction patterns for Co nanorod arrays with varying lengths are shown in Fig. 4.6(a). The 2θ scan provides the information of Co nanorods with a preferential growth of fcc (111) for length up to 200 nm and further growth indicate the change of the crystalline structure into hcp polycrystalline phases with the presence of peaks from (100) at 41.6° and (110) at 75.9° respectively. Some of the additional peaks at 38.2° , 64.6° , and 77.5° are obtained from the Ag (filled square) coated thick film, which served as an electrical contact in one of the faces of the porous membrane. The peak corresponding to Co fcc (111) at $2\theta \sim 44.4^\circ$ is shown in Fig. 4.6(b) in the expanded form, which indicates that the decrease in FWHM while growing the length of Co nanorod array from 40 to 400 nm, as expected in a nano-scale regime. Moreover, it is well known that to distinguish between the peaks arising from hcp (002) and fcc (111) Co phases is very difficult, where the 2θ lies very close to each other i.e., at 44.2°

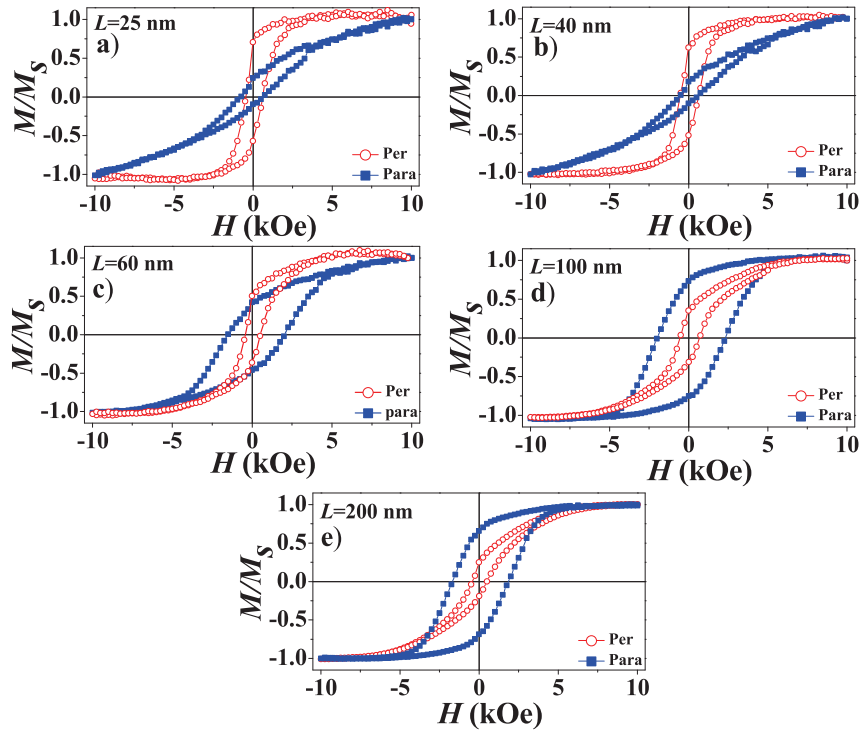


Figure 4.7: Magnetic behavior of Co nanorod arrays with variable length a) $L=25$ nm, b) $L=40$ nm, c) $L=60$ nm, d) $L=100$ nm, e) $L=200$ nm.

and 44.4° , respectively. In particular, we know that for bulk Co, the hcp structure is more stable than the fcc structure at room temperature (Ye et al. 2009), whereas, the plausible growth of hcp (002) phase for larger diameter (~ 70 nm) was discussed earlier in section 4.3.1 and reported in our work (Sellarajan et al. 2013, Kulkarni et al. 2013). However, it is still unclear why the amount of fcc phase increases in small diameter (Darques et al 2004, Sánchez-Barriga et al. 2009, Pirota et al. 2011). In particular, this agrees with very recent studies of diameter influenced crystalline phase diagram, which reported that fcc Co phase formation is favorable for 35 nm pore size while growing them through electrochemical route (Sánchez-Barriga et al. 2009, Pirota et al. 2011, Vivas et al. 2011, Vivas et al. 2013).

4.3.2.1 Effective magnetic anisotropy

Experimental results

We have also performed magnetic characterization with applied field both parallel (\parallel) and perpendicular (\perp) to the nanorod axis at room temperature. Figures 4.7(a)-(e) show the complete data set of the hysteresis loop for different lengths of the nanorod arrays. Table 4.2 presents the extracted physical parameters from the measured $M(H)$

loops. In this table, M_r^{\parallel}/M_s and M_r^{\perp}/M_s represent the remanence ratio for parallel and perpendicular directions, respectively. Hence, the ratio, $M_r^{\parallel}/M_r^{\perp}$, greater or less than unity determines the easy axis parallel or perpendicular to the nanorod axis, respectively. The magnetization easy axis may also be defined by the sign of the effective anisotropy field, ΔH_s (Ahmad et al. 2011). Here the estimated values of ΔH_s ($= H_s^{\perp} - H_s^{\parallel}$) for our samples are given in table 4.2, where H_s^{\parallel} is the saturation field when the magnetic field is applied parallel to the nanorod axis and H_s^{\perp} is the saturation field when the magnetic field is applied perpendicular to the nanorod axis. The dependence of ΔH_s on L and hence the change over in easy axis direction from perpendicular to parallel direction supports the observation made on remanence ratio data, as mentioned above.

From table 4.2, it is confirmed that the easy axis lies along the longitudinal direction for $L \geq 100$ nm as expected from the shape anisotropy. However, a reduction in both H_c^{\parallel} and M_r^{\parallel} was observed for $L = 200$ nm. The origin of such discrepancy might be due to the change of the crystalline structure from fcc (111) phase to hcp (100) phase while nanorod growing in length beyond 200 nm. This is further confirmed from the X-ray diffraction data where the appearance of hcp(100) phase was observed for a nanorod of length 400 nm (see Fig 4.6(a)). The fcc (111) phases orient one of their easy magnetization direction along the nanorod axis, which reinforces the shape anisotropy. Whereas, the small contribution from the hcp (100) phase, in which the c axis is aligned normal to the rod axis, may result in the decrease of M_r^{\parallel} and H_c^{\parallel} (Pirota et al. 2011, Vivas et al. 2011, Sellarajan et al. 2013, Vivas et al. 213). As presence of hcp (100) phase within a nanorod complicates the magnetization reversal process (Sellarajan et al. 2013), in this case, our theoretical explanations on observed behavior of anisotropy field, ΔH_s as a function of L was restricted to the nanorod length, $L \leq 200$ nm. To explain $\Delta H_s(L)$, the following two approaches are made: (i) analytical calculations and (ii) micromagnetic simulations, which are provided below.

Table 4.2: Extracted magnetic parameters of Co nanorods.

Length (nm)	H_c^{\parallel} (Oe)	H_c^{\perp} (Oe)	M_r^{\parallel}/M_s	M_r^{\perp}/M_s	$\Delta H_s = H_s^{\perp} - H_s^{\parallel}$		
					Expt. ΔH_s (Oe)	Analytical (H_k)(Oe)	Simulated ΔH_s (Oe)
25	710	530	0.16	0.64	-5676 ± 275	-3355	-2394
40	563	588	0.15	0.56	-3854 ± 265	-604	-2380
60	1781	474	0.43	0.43	-1344 ± 224	1408	-1195
100	2151	626	0.74	0.33	1016 ± 230	3188	1492
200	1730	472	0.64	0.22	1595 ± 350	4002	3276

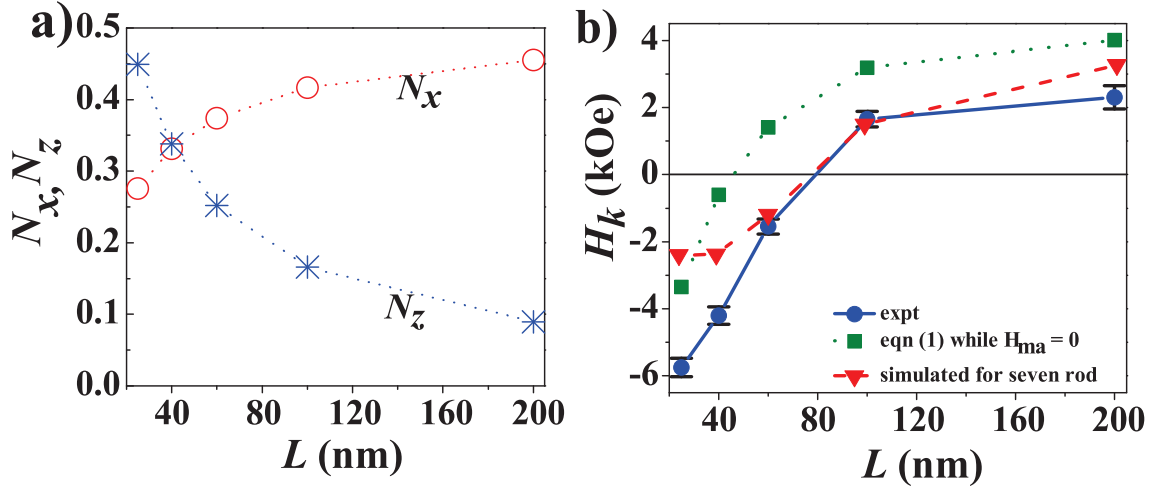


Figure 4.8: a) The behavior of the demagnetization factors (N_x and N_z) as a function of L for circular cylinders, calculated using on Eqns. 2 and 3, and b) the effective anisotropy field (H_k): experimental, micromagnetic simulated, and analytical expression (Eqn. 1) as a function of length (L).

Analytical Calculations

An analytical approach has been made to estimate the effective magnetic anisotropy field on an array of nanocylinders based on the following assumptions: 1) the shape anisotropy related with demagnetization factor of the geometry, 2) the magneto-crystalline anisotropy, depending on the crystal symmetry of the material used and 3) the magneto-static coupling among the nanocylinder arrays, as described in Eqn. 1.2.3, and can be written as in cgs unit (Strijkers et al. 1999, Han et al. 2003, Ahmad et al. 2011):

$$H_k = 4\pi\Delta N(L)M_s + 6.3\pi M_s r^2 L/S^3 \pm H_{ma}; \quad (4.3.1)$$

where r , L and S are the nanorod parameters such as radius of the nanorod, length of the rod and the separation between the rods (in nm) respectively and $\Delta N(L) = N_x(L) - N_z(L)$; with N_x and N_z are the demagnetization factor along the x and z-axis respectively, and can be determined using the relations (Lavin et al. 2009),

$$N_z(L) = 1 - F_{21}(D^2/L^2) + \frac{4D}{3\pi L}. \quad (4.3.2)$$

and

$$N_x = (1 - N_z)/2 \quad (4.3.3)$$

Here, $F_{21}(y) = F_{21}[-1/2, 1/2, 2, -y]$ is a hypergeometric function. Figure 4.8(a) presents the variations of N_x , and N_z as a function of L . It is interesting to see that for the ratio of

$L/D=0.9065$, the values of N_x and N_z become $1/3$, where the effect of shape anisotropy gets nullified due to the spherical symmetry of the nanorods. Hence, equation (4.3.1) predicts the crossover of H_K from negative to positive value occurred at a critical length, $L_c (= 4\Delta NS^3/6.3r^2 \sim 45.9 \text{ nm})$ with a rod diameter of 45 nm. In other words, for $L > L_c$ the easy axis lies along the rod axis, whereas for $L < L_c$, it is perpendicular to the rod axis. The calculated $H_k(L)$ values using equation (4.3.1) with $H_{ma} = 0$ is shown in Fig. 4.8(b). The estimated anisotropy field for our samples, tabulated in table 4.2, is also plotted in Fig. 4.8(b) along with the above analytically calculated curve. From this figure, it is clear that a large discrepancy on L_c value was observed. Experimentally determined value of L_c was around $78 \pm 5 \text{ nm}$, which was almost two times larger than the analytically predicted one. This large discrepancy may be attributed by the non-uniform reversal magnetization process in the rods, as mentioned by a vortex domain wall for fcc (111) (Vivas et al. 2013). To further understand the reversal magnetization process, micromagnetics simulations has been carried out using 3D–OOMMF package, as described in Chapter 6.

4.4 CONTINUOUS DEPOSITION

In this case, the main objective is to prepare Co nanowires with hcp (002) phase to study the magnetostatic interaction between the nanowires in arrays. Therefore, the electrodeposition conditions are modified from pulse deposition into a continuous deposition process at $-1.1 \text{ V vs Ag/AgCl}$ and pH of 6.7 as reported by several authors (Darques et al. 2004, Vivas et al. 2012). This leads to growing the hcp (002) phase inside four different nanopore geometries of porous AAO membrane.

4.4.1 Effect of magnetostatic interaction in hcp Co (002) phase

The textured growth of hcp Co (002) nanowire arrays were prepared with consideration of following geometries (i.e., pore diameter (D_p) and interpore separation (I_p)) of alumina membrane:

- $D_p = 25 \text{ nm}$ and $I_p = 65 \text{ nm}$
- $D_p = 45 \text{ nm}$ and $I_p = 65 \text{ nm}$
- $D_p = 50 \text{ nm}$ and $I_p = 105 \text{ nm}$
- $D_p = 80 \text{ nm}$ and $I_p = 105 \text{ nm}$

In this case, the above variation in the pore geometry leads to have the nanowire diameter approximately the same within two different cell sizes ($I_p = 65 \text{ nm}$, and 110

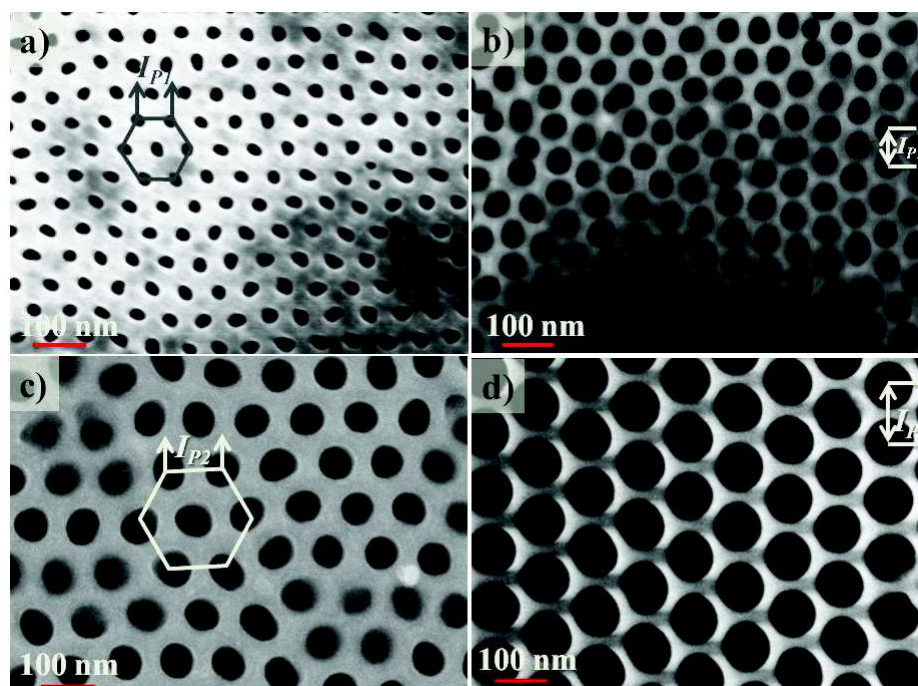


Figure 4.9: Surface morphology of porous AAO membrane with two different diameters in cell sizes of 65 nm (a-b), and 110 nm (c-d). The diameters of the AAO membranes are (a) 25 nm, b) 45 nm, c) 50 nm and d) 80 nm, respectively.

nm for $D_p \sim 50$ nm). During the investigation, the analysis is also considered by ' N ', number of wires per unit area, i.e., $N \sim 1.0 \times 10^9$ per cm^2 for larger interwire spacings (110 nm), and for 65 nm spacings: it is approximately equal to $3 \times N$ (i.e., $\sim 3.0 \times 10^9$ per cm^2). Here, for simple system the length and the crystalline phase is controlled by maintaining the electrodeposition time and the deposition parameters (pH=6.7 and 40 °C). The uniform in length and higher filling rate ($> 90\%$) of Co hcp (002) have been achieved for length (L) of < 300 nm. Importantly, hcp Co (002) phase is chosen because the length of the nanowire has not influenced in their magnetic properties (coercivity and remanence ratio) of Co nanowire arrays in the absence of other crystalline phase, as reported previously in this work (Sellarajan et al. 2013, Kulkarni et al. 2013).

4.4.1.1 Magnetic properties as a function of nanowire geometry (both inter-wire separation and diameter)

The highly ordered hexagonal arrays of monodispersed pores in the AAO membrane is confirmed by FESEM imaging, as depicted in Fig. 4.9. In this figure, sample (a,b) were prepared in H_2SO_4 bath at 25 V, and the pore widening time was kept at 20 min

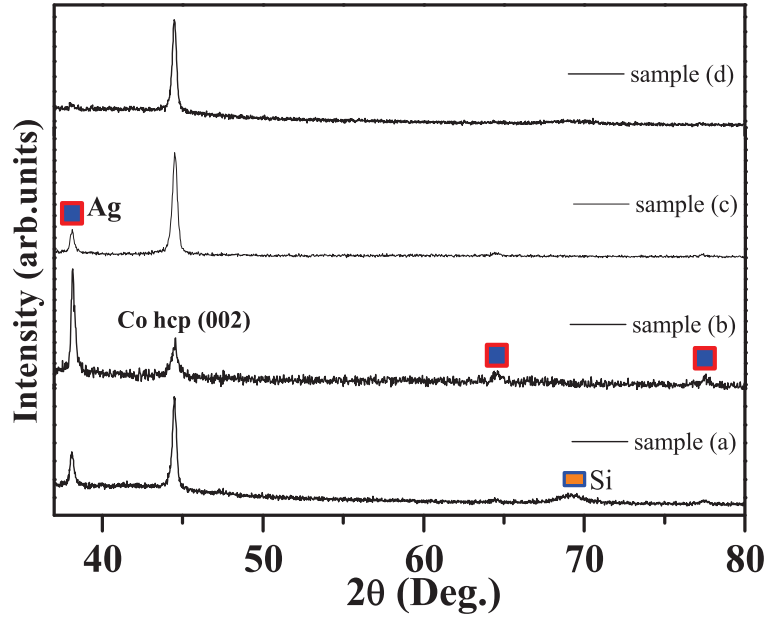


Figure 4.10: The structural characterization of Co embedded porous anodic alumina by X-ray diffractometer as function of diameter (cell size): a) 25 nm (65 nm), b) 45 nm (65 nm), c) 50 nm (110 nm), and d) 80 nm (110 nm), respectively.

($D_p \sim 25 \pm 3$ nm) and 29 min ($D_p \sim 45 \pm 5$ nm) without affecting $I_{p1} \sim 65 \pm 4$ nm, respectively. Similarly, AAO membranes with larger interpore distance, $I_{p2} \sim 110 \pm 3$ nm were prepared in $C_2H_2O_4$ bath at 40 V with the pore size of 50 ± 5 nm (45 min) and 80 ± 7 nm (90 min), as shown in Figs. 4.9(c and d), respectively.

In addition to this, X-ray diffraction patterns of deposited Co nanowires are presented in Fig. 4.10 as a function of wire diameter (inter-wire separation), as mentioned above. As shown in these figures, only one peak is observed at $2\theta = 44.4^\circ$, indicating a textured growth of Co with hcp (002) phase, irrespective of different wire diameters. Such observations were also reported for nanowire grown in electrolyte with PH above 6 (Darques et al. 2004).

Magnetic properties of as-grown samples were performed at room temperature using a vibrating sample magnetometer (VSM: LakeShore) while applying 10 kOe (H_{ext}) field in the direction parallel and perpendicular to nanowire axis. The resultant $M(H)$ hysteresis loops are shown in Figs. 4.11(a)-(d) for different wire diameters of 25 ± 3 , 45 ± 5 , 50 ± 5 and 80 ± 7 nm, respectively. We refer these samples as sample-a, sample-b, sample-c and sample-d hereafter and they correspond to Co NWs with D_p (I_p) of 25 (65), 45 (65), 50 (110) and 80 nm (110 nm), respectively. Table 4.3 show the extracted magnetic parameters such as coercive field (H_c), and remanent magnetization value (M_r/M_s) in both parallel (H_{ext}^{\parallel}) and perpendicular (H_{ext}^{\perp}) directions. At first, the

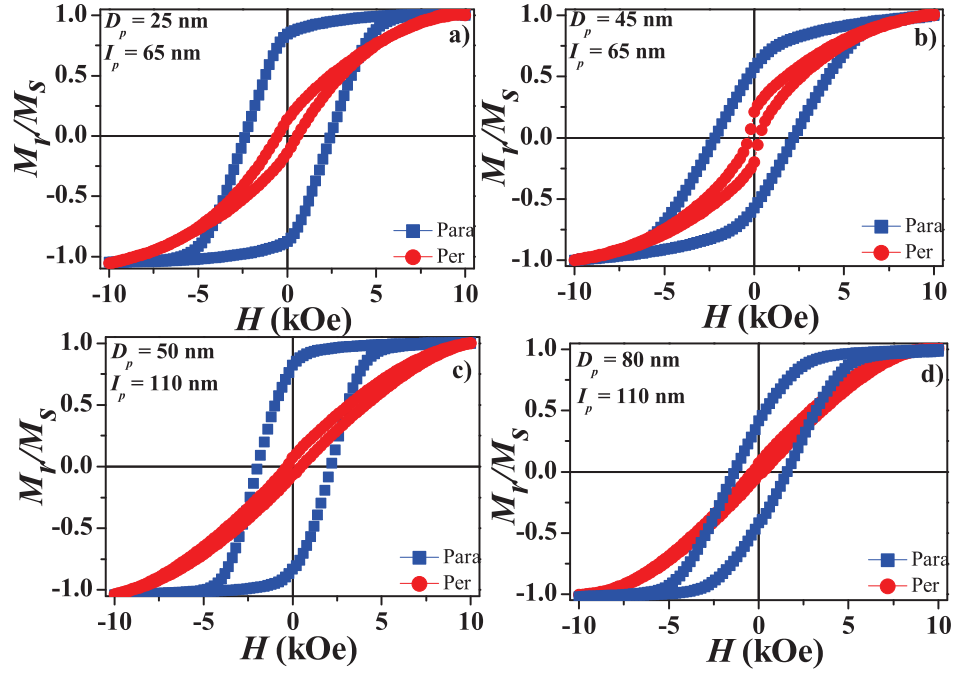


Figure 4.11: $M(H)$ loops Co nanowire arrays with four different diameters within the two different interwire separations: D_p 25 nm (a) and 45 nm (b) in I_p of 65 nm, and D_p 50 nm (c) and 80 nm (d) in I_p of 110 nm. H_{ext} is applied in both parallel (square) and perpendicular (circle) to nanowire axis.

reduction in H_c was observed with increase in diameter of the nanowires for an applied field parallel to the nanowire axis, as reported by several authors. The behavior of coercivity as a function of D/S for a constant L (D =wire diameter, L = wire length, and S =inter-wire spacings), was derived based on the analysis of the influence of effective magnetostatic interaction among the nanowires, and the expression is as follows (Vázquez et al. 2005, Arora et al. 2012),

$$H_c = \frac{2K}{\mu_0 M_s} [1 - \{ \frac{N|E_v|}{K} \}^{1/2}], \quad (4.4.1)$$

where $2K/\mu_0 M_s$ denotes the intrinsic H_c due to magnetic anisotropies, K , E_v is magnetostatic interaction energy, and N is the number of nanowires which are reversed by the large E_v . It is well known that magnetostatic interactions favor an antiparallel distribution of magnetization in the neighboring NWs and depends on the direction of the field, length (L) to the diameter (D) ratio and inter-wire separation (S). In this case, the reversal of an individual nanowire results in the decrease in the E_v that equals in the magnetic anisotropy barrier ΔE . Here, the interaction term has been derived while considering that the NWs are homogeneously magnetized for $D/L \ll 1$, i.e., due to their uniaxial magnetic anisotropy, with magnetic charges at both ends, $\sigma = |M|$. This

interaction energy, E_v was considered as multipolar components rather than dipolar for $S \ll L$, and can be written as (Vázquez et al. 2005, Arora et al. 2012),

$$E_v = \left(\frac{\mu_0}{8\pi}\right)M_1M_2L\left(\frac{D^2}{S}\right)\left\{1 - \left[1 + \left(\frac{L}{S}\right)^2\right]^{-1/2}\right\}, \quad (4.4.2)$$

where, M_i is the magnetization component along the length of the wires. Equations (4.4.1) and (4.4.2) suggest that with the increase in D/S , the magnetic charges would increase leading to an enhanced magnetostatic interaction between the wires for constant L . Additionally, for constant D , the increase in L/S leads to increase the static interaction in the array of NWs. This is having a good agreement with our experimental results, that the observed decrease in the H_c value is as a function of D . Importantly, for constant L/D , our results show that the extracted H_c values of two different S (I_{p1} and I_{p2}) are ~ 2000 Oe in Co nanowires [$D \sim 50$ nm as shown in Figs. 4.11(b and c)]. Therefore, it is clearly indicating that the obtained H_c value is not highly influenced by term L/S at room temperature. In order to obtain deeper information, the temperature dependence of magnetic hysteresis loops have been measured for sample -b and -c, when the field is applied parallel to the nanowire axis. The corresponding $H_c(T)$ is later discussed for providing the possible influence of L/D with temperature.

Moreover, it is clear from the magnetization hysteresis loops that for all the samples the easy axis is along the wire length. The higher $M_r/M_s \sim 0.9$ is observed for smaller ratio of D/S [sample-a ~ 0.35 and sample-c ~ 0.45], whereas in case of larger D/S ratio [sample -b and -d (~ 0.7)] the shearing effect is observed to be more and resulted with a reduction in the M_r/M_s (see Table 4.3). This indicates that the magnetostatic interactions are increasing as wires get closer together. Therefore, the variation in M_r^{\parallel}/M_s for wire diameter of ~ 50 nm in two different I_p values are believed to be influenced by the magnetostatic interaction between the neighboring nanowires in arrays, as suggested in Eqn. 4.4.2. This is also consistent with the results obtained by

Table 4.3: Magnetic parameters of hcp Co (002) nanowires as function diameter and interwire spacing.

Sample Name	Diameter (nm)	interwire spacing (nm)	Packing density	H_{ext}^{\parallel}		H_{ext}^{\perp}	
				H_c^{\parallel} (Oe)	M_r^{\parallel}/M_s	H_c^{\perp} (Oe)	M_r^{\perp}/M_s
sample-a	25	65	3×10^9	2500	0.9	610	0.13
sample-b	45			2240	0.68	300	0.2
sample-c	50	110	1×10^9	2110	0.86	400	0.12
sample-d	80			1500	0.41	250	0.05

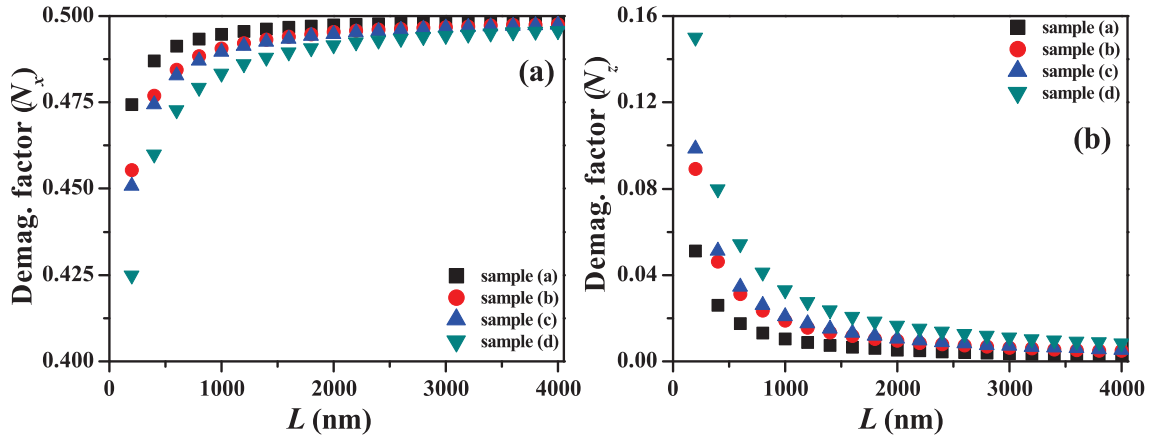


Figure 4.12: Theoretically calculated demagnetization factor of nanowire in both perpendicular (N_x :fig. (a)) and parallel (N_z :fig.(b)) to nanowire axis, by using Eqns. 4.3.2 and 4.3.3.

Sanchez-Barriga et al. (2009), a reminiscent influence of the magnetostatic dipolar interaction on the magnetic behavior could manifest through a small contribution to the reduced remanent magnetization for shorter wires.

The effective anisotropy of grown Co nanowires was mainly contributed by the shape anisotropy, magnetocrystalline anisotropy, magnetoelastic anisotropy, and magnetic dipole interaction between the nanowires in arrays. Here, the magnetoelastic anisotropy is not considered for calculations in Co with the poor magnetostriction effect. Therefore, the dipolar interaction is the only term which results in the variations in the $M(H)$ loops of sample -b and -c. Other contributions from the shape and the magnetocrystalline anisotropies are same as the diameter and the crystalline phase of Co NW were kept same. Here, the shape anisotropy arises from the demagnetization factor of the 1D nanowires. The value of shape anisotropy field, $H_{shape} \sim 2\pi M_s$, is independent to the wire diameter for $L \gg D$. Figure 4.12 shows theoretically predicted demagnetization factors as a function of length for all four samples shown in Fig. 4.11(a)-(d). As expected the close relation is found for samples between -b and -c, at where the shape demagnetization factor may not affect the magnetic characteristics of Co nanowires (see Fig. 4.12). Furthermore, the understanding of reversal magnetization processes due to the magnetostatic and magnetoelastic effects were carried out in sample -b and -c at low temperature from 300 K to 5 K with the interval of 50 K, respectively.

Figures 4.13(a and b) show the resulting hysteresis loops measured for both systems of nanowire arrays at low temperatures. Insets show the magnetization behaviors of Co nanowires when the field is applied to ± 40 kOe, along the wire axis at different temperatures. The main observation as a quasi-monotonic decrease in H_c with increasing

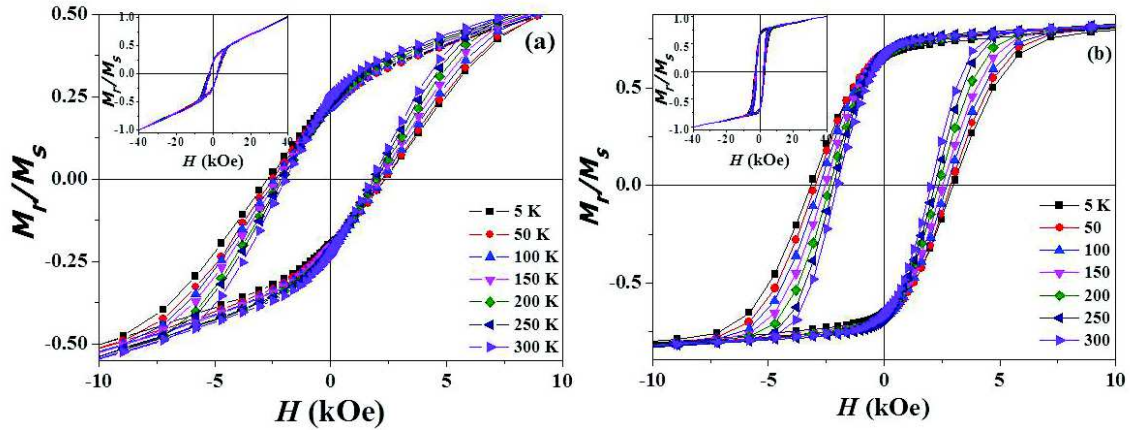


Figure 4.13: Low temperature magnetic measurements of Co nanowire arrays with diameter of ~ 50 nm for two different inter-wire separations: a) 65 nm, and b) 110 nm. Inset shows the $M(H)$ loops of the corresponding Co NWs with $H_{ext} = \pm 4$ kOe.

temperature is shown in magnified $M(H)$ loops in Fig.4.13, and the values of $H_c(T)$ and the variation of normalized remanent (M_r/M_s) values as function of temperature are depicted in Figs. 4.14 (a and b) for samples -b and -c, respectively. In this case, the M_r/M_s value is defined as the value of M_r is normalized with the value of M at 40 kOe, i.e., the ratio of the magnetization at $H_{ext} = 0$ and 40 kOe ($M(0)$ and $M(40)$ kOe).

From $H_c(T)$ data, the following observations are made. $H_c(T)$ follows a linear behavior with dH_c/dT have a negative slope of -2.27 for I_{p1} (sample-b) and -4.05 for I_{p2} (sample-c), respectively. This linear increment of $H_c(T)$ in both of the sample is due to the suppression of the thermally activated magnetic relaxation at low temperature. However, the variation in the rate of the increment in $H_c(T)$ is nothing but due to the effect of the magnetostatic interaction between the neighboring wires. In addition to this, the contribution of magnetostatic interaction field has been evaluated by using a simple formula, $H_{int} = -4.2M_s\pi r^2 L/S^3$, at where the interwire separation is reciprocal to H_{int} , here M_s , r , L and S are the saturation magnetization, radius, length and separation between the nanowires (Strijkers et al. 1999, Han et al. 2002, Srivastava et al. 2007). Then, the calculated values of sample -b and -c are -128 Oe and -37.5 Oe for $L=300$ nm, respectively. However, the variation in the $H_c(T)$ can be clarified due to the two different approaches, that may be (i) due to the variation in the observed M_s as function of T, i.e., it increased (i.e., $M_s(T)=17\%$ from 300 K to 5 K) for sample (c) and it remains nearly constant M_s (7%) for sample (b) in the temperature range studied, and (ii) the variation in the tensile stress on the wires due to the contraction effect of the alumina at low temperature.

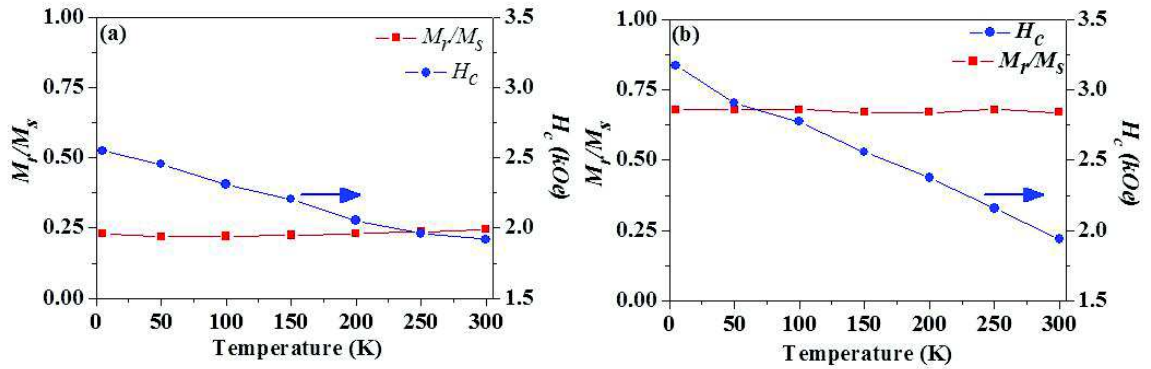


Figure 4.14: M_r/M_s (square) and H_c (circle) measured parallel to the axis of the nanowires plotted as a function of temperature for Co nanowire arrays with diameter of ~ 50 nm for two different interwire separations: a) 65 nm, and b) 110 nm.

4.5 SUMMARY

This chapter highlights the importance of crystalline structure in the magnetic properties of Co nanowire arrays. It can be concluded that:

- The crystalline structure of Co was tailored with varying both diameter and the electrochemical processes.
- For pulse deposition, the structure of Co has been modified from hcp (002) to fcc (111) while reducing the diameter. Whereas, the change in pH has not shown any influences during the growth of crystalline Co. However, the increase in the length of nanowire was demonstrated with the change in crystallographic phase to hcp (100) above the critical length in both cases. The reason behind this structural transition is still unclear. However, this may be due to a twisted wire with circumferential strain while growing nanowires in a constrained AAO pore wall structure as suggested by Hu et al [2005].
- This change in the crystallographic phase of Co as a function of the length of nanowire resulted with different magnetic behaviors. Independent to nanowire length, Co hcp (002) phase shows longitudinal anisotropy, whereas, fcc Co (111) was established by the change in the magnetic anisotropy from transverse to longitudinal just below and above the critical length. However, the reduction in the longitudinal anisotropy was observed with the presence of hcp (100) phase above certain NWs length. Importantly, the observed reduction in coercivity and remanent ratio of ordered Co nanowires were also explained considering the change in crystalline structure from hcp (002) to hcp (100) phase as they grow in length,

i.e., the hcp (100) phase determines magnetocrystalline anisotropy nearly at transverse orientation and compensate the shape anisotropy. The angular measurement was evident for the highly uniaxial and isotropic magnetic anisotropy as a function of hcp crystalline Co phases for L of 200 and 1000 nm, respectively.

- For continuous deposition, different hcp Co phase textures were obtained by modifying the electrolyte pH from 2 to 6.7 in the electrodeposition of Co nanowires at 40 °C. In this case, the uniaxial magnetic anisotropy with hcp Co (002) phase (i.e., magnetization easy axis lies along the nanowire axis) was grown in different diameter and periodicity, to demonstrate the magnetostatic interaction effect among the NWs. Here, it was paid attention to study the magnetostatic interaction between the NWs by keeping the diameter \sim same and varying the interwire spacings (i.e., vary the density of the NWs) in hcp Co (002) phase. Therefore, the resultant reduction in remanent ratio was considered as a function of diameter and the interwire spacings, whereas coercivity was determined by only the diameter in the array of Co NWs. During this investigation, nanowire at \sim 50 nm in diameter exhibits nearly equal H_c (\sim 2.0 kOe) for both the inter-wire spacings. However, the resultant M_r/M_s was founded to be highly influenced by the interwire spacings, i.e., 0.9 for 105 nm and 0.6 for 65 nm. This was exemplified by the long range order of magnetic dipolar interaction among the nanowire arrays with different densities $[(0.8-2.25) \times 10^{10}$ per cm^2]. With decreasing NWs diameter within the same interwire spacings, both H_c and M_r/M_s was found to be increased and enhancing the shape anisotropy in hcp Co (002) phase. This latter effect is even more pronounced in the case of NWs separated with $>$ twice the diameter of Co nanowires, either lower or higher density of NWs, i.e., the highest M_r/M_s achieved in hcp Co (002) phase.

These findings are indicating the crystalline structure of Co depends on both the geometrical parameters and the particular electrodeposition parameters. Furthermore, detailed investigations are required to understand the reversal magnetization processes of different Co phases which are observed in micromagnetic simulations.

Chapter 5

PREPARATION AND MAGNETIC PROPERTIES OF NANODOT ARRAYS

5.1 SURFACE PATTERNING OF MAGNETIC NANODOT ARRAYS

Recent studies on ordered arrays of surface nanostructures such as nanodots and nanoholes became intensive research interest due to cost effective approach by a non-lithographic patterning process (Lei et al. 2007, Kouklin et al. 2006). In this approach, ultrathin alumina membrane (UTAM) was used as an evaporation or etching mask on a substrate. This method is applicable to pattern all different types of materials such as metals, semiconductors, and metal alloys (Lei et al. 2005, Kouklin et al. 2006, Ding et al. 2006, Li et al. 2006, Kim et al. 2007, Zou et al. 2009, Gao et al. 2009, Wu et al. 2010). Hence, this low-cost, nano-patterning process become an ideal model system to the fabrication of electronic, magnetic and optical nanodevices with extremely small size and high density.

In particular, the porous alumina membrane possesses several essential features desirable to test the theories of nanomagnetism and their future applications. The size and the periodicity of the pores can be tuned by selecting the appropriate anodization conditions (Jessensky et al. 1998, Li et al. 1999). As reported earlier, these porous masks were prepared by two methods; i) attached UTAM (i.e., a free-standing ultrathin alumina membrane is ready to transfer on any of the substrate), and ii) connected UTAM (i.e., growth of ultra-thin porous alumina on a desired substrate) (Lei et al. 2005, Li et al. 2006, Lei et al. 2007). Due to higher regularity and large scale of ordering, attached UTAM (Jeong et al. 2009) is more preferable. In this process transferring these thin porous alumina on the Si wafer is most critical and challenging task. It is also reported that the size and the shape of the nanoparticles can be tuned due to the shadowing effect by thickening the porous membrane or by the deposition time (Wu et al. 2010).

Arrays of magnetic nanodots (Fe, Ni, Co, FePt, CoPt, etc.,) had been fabricated by using this technique (Li et al. 2006, Kim et al. 2007). Most of their magnetic properties were limited by perpendicular anisotropies for high density magnetic media applications. Research on hard magnetic in-plane anisotropy was not reported previously. In

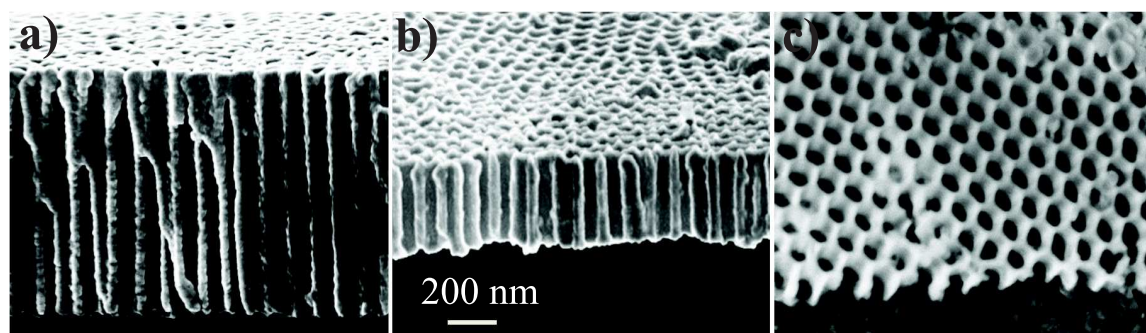


Figure 5.1: FESEM surface morphology and section view of the UTAM with different anodization time (a) 900 s, (b) 420 s and (c) 75 s. The scale bar used here are for 200 nm.

this report, we patterned both soft ($\text{Co}_{90}\text{Fe}_{10}$) and hard (SmCo_5) magnetic nanodot arrays with large in-plane magnetic anisotropies. The dot arrays with different heights were deposited and the results were correlated with the thickness of the same thin film. The in-plane magnetic anisotropy was liable in both film and the dot arrays, however, the strong magnetic anisotropy was reduced in the dot array due to the exhibited vortex along the perpendicular direction. This magnetic vortex has a strong potential application in spin-based nanoelectronic devices because of the superior thermal stability and the negligible magneto-static interaction.



Figure 5.2: Surface morphology of UTAM after transferred on Si substrate.

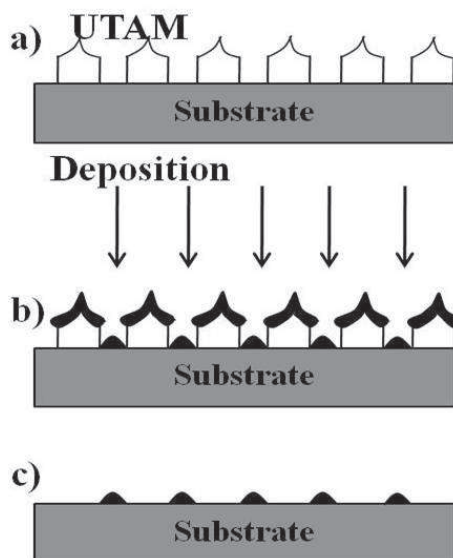


Figure 5.3: Schematic outline of the fabrication of highly ordered nanodot arrays and the anti-dot formation which limits the shape of the dots (a-c).

5.2 CONDITION OPTIMIZATION OF UTAM

The cross-sectional view of highly ordered porous anodic alumina membrane (AAO) was shown in Fig. 5.1(a-c) for thicknesses of a) 880 ± 20 nm, b) 360 ± 20 nm, and c) 100 ± 20 nm. The average thickness of the AAO was controlled by the anodization time (i.e., 900 to 75 s). Interestingly, even after the barrier removal, the thinner membrane retains the shape of honeycomb structure (see Fig.5.1(c)) while comparing with a thick membrane (> 300 nm) which has circular in pore structure. This is due to the higher etching rate of side walls in UTAM structure.

Alumina membranes with aspect ratio ($\tau = \text{thickness/pore size}$) from 10 to 1 were used as evaporation masks on Si substrate. CoFe was deposited by sputtering technique in a ultra-high vacuum chamber. The removal of UTAM leads to show the ordered of nanodot arrays on Si. It is to be mentioned that the well-ordered nanodot structures were obtained through the UTAM of thickness less than 300 nm ($\tau < 3$). For ($\tau > 3$), the shadowing effect does not allow to form the nanodot array on the substrates, though the formation of nanodot arrays structures $\tau \leq 10$ was reported by Lei et al. (2007).

Similarly, UTAM was also prepared in 0.3 M sulphuric acid by varying the 2nd anodization duration from 20 to 50 s for $\tau < 3$. The growth rate is 2.5 nm/s with pore size of 25 nm and interpore distance of 65 nm in 25 V, 3 °C. The optimum conditions were tabulated in Table 1. Photo shows the transparent UTAM which is transferred on Si substrate in Fig.5.2.

Table 5.1: Optimum condition for the fabrication of UTAM.

Electrolyte (0.3 M acid)	2 nd anodization time (s)	Growth rate (nm/s)	Pore widening time (min)	Pore parameter	
				D_p (nm)	I_p (nm)
Oxalic	75-150	1	50-60	80-100	110
sulphuric	20-50	2.5	13-18	25-40	66

5.3 FABRICATION OF NANODOT ARRAYS VIA SPUTTERING TECHNIQUE

5.3.1 $\text{Co}_{90}\text{Fe}_{10}$ Nanodot arrays

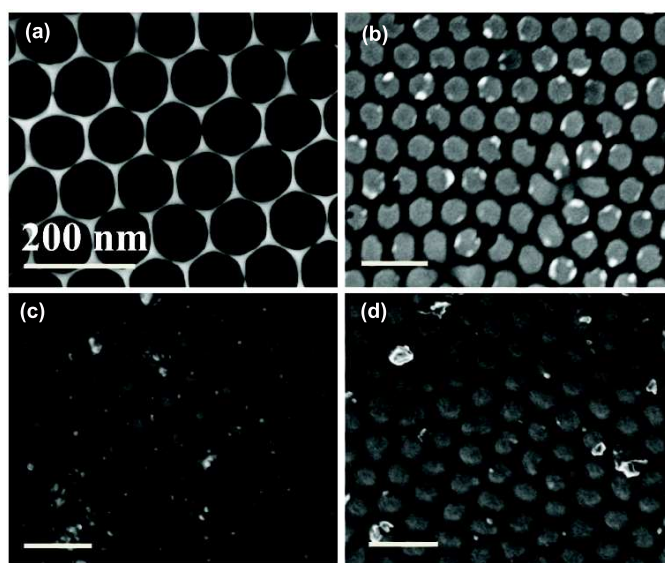


Figure 5.4: Surface morphology of the UTAM based nanodot arrays prepared by the sputtering system with variable thickness on CoFe. a) UTAM on Si substrate, b) CoFe dots with 10 nm thickness, c) 20 nm and d) 30 nm. Here, the scale bar drawn is 200 nm.

Nanodot array structures of $\text{Co}_{90}\text{Fe}_{10}$ with varying height from 0 to 50 nm were deposited by varying the duration of sputtering time. During sputtering, the deposition occurred: i) through the nanochannel arrays, and ii) on the top surface of the pore walls. With the progress of deposition, in other words, as the thickness of the deposited film increases, the face of the pore wall becomes narrower. This leads to the change in shape of the deposited nanostructure from disc to elliptical to conical. This phenomenon is known as shadowing effect in the fabrication of patterned nanodot arrays using UTAM

as an evaporation mask by sputtering as shown in Fig.5.3. In fact, we also observed the disk arrays without shadow effect for thickness less than 20 nm. However, the shape was little modified into hemisphere for higher thickness. Figure 5.4 shows the highly ordered hexagonal arrays of $\text{Co}_{90}\text{Fe}_{10}$ nanodot structures with a thickness of 20 (b), and 30 nm (c-d). The dot arrays were replicating the same hexagonal ordering as similar to porous membrane in the patterned nanodots.

5.3.2 Magnetic properties of NanoDot arrays

5.3.2.1 Vibrating sample magnetometry

The magnetic properties of the fabricated nanodot arrays are macroscopically analyzed by vibrating sample magnetometry. Here, anti-dot arrays will also contribute significantly in the $M(H)$ loops. This was avoided by ultrasonication in diluted NaOH before performing the magnetic studies. This will help to remove the UTAM along with antidot arrays.

Figures 5.5 (a-e) show the in-plane easy magnetization of $\text{Co}_{90}\text{Fe}_{10}$ nanodot arrays structure with heights a) 10, b) 20, c) 30, d) 40, and e) 50 nm, respectively. The resultant behavior shows gradual increase in the M_r/M_s from 0.4-0.8 and H_c from 100 to 300 Oe with increase in $\text{Co}_{90}\text{Fe}_{10}$ thicknesses, as shown in Fig. 5.5(f). Whereas, small discrepancy in the decrease in H_c with single domain state was observed at 50 nm, which may be due to the presence of magnetic antidot arrays on the sample surface with maximum error(30-40%). Therefore, the film thicknesses are limited to less than 50 nm for UTAM with a pore size of 100 nm. Interestingly, $M(H)$ loops accompanied with these H_c variations were involved in the reversal magnetization processes with a different magnetic state such as vortex, single domain. Li et al. (2007) reported that $M(H)$ loops with reduced H_c values by the pinched neck were representing vortex magnetic states, as shown in Fig. 5.6(a). The pinched neck can be quantified by calculating the ratio between width of the hysteresis loop at zero magnetization ($W_{M=0}$), and at half the saturation magnetization ($W_{M=0.5M_s}$, i.e., $\delta = W_{M=0}/W_{M=0.5M_s}$ as shown in Fig. 5.6(b). The loop width ratio, δ was observed to increase from 0.6 to 0.8 as the thicknesses increase from 10 to 50 nm. It is evidenced that the increase in thickness leads to single domain state with width ratio close to ~ 1 . Whereas, 20 nm sample shows perfect vortex state with smaller width ratio of ~ 0.4 . As a comparison, we have shown the $M(H)$ loop of 20 nm thin film, which indicates a single domain state. Further understating of these vortex magnetic states were analyzed by the first order reversal curve, see section 5.3.3.

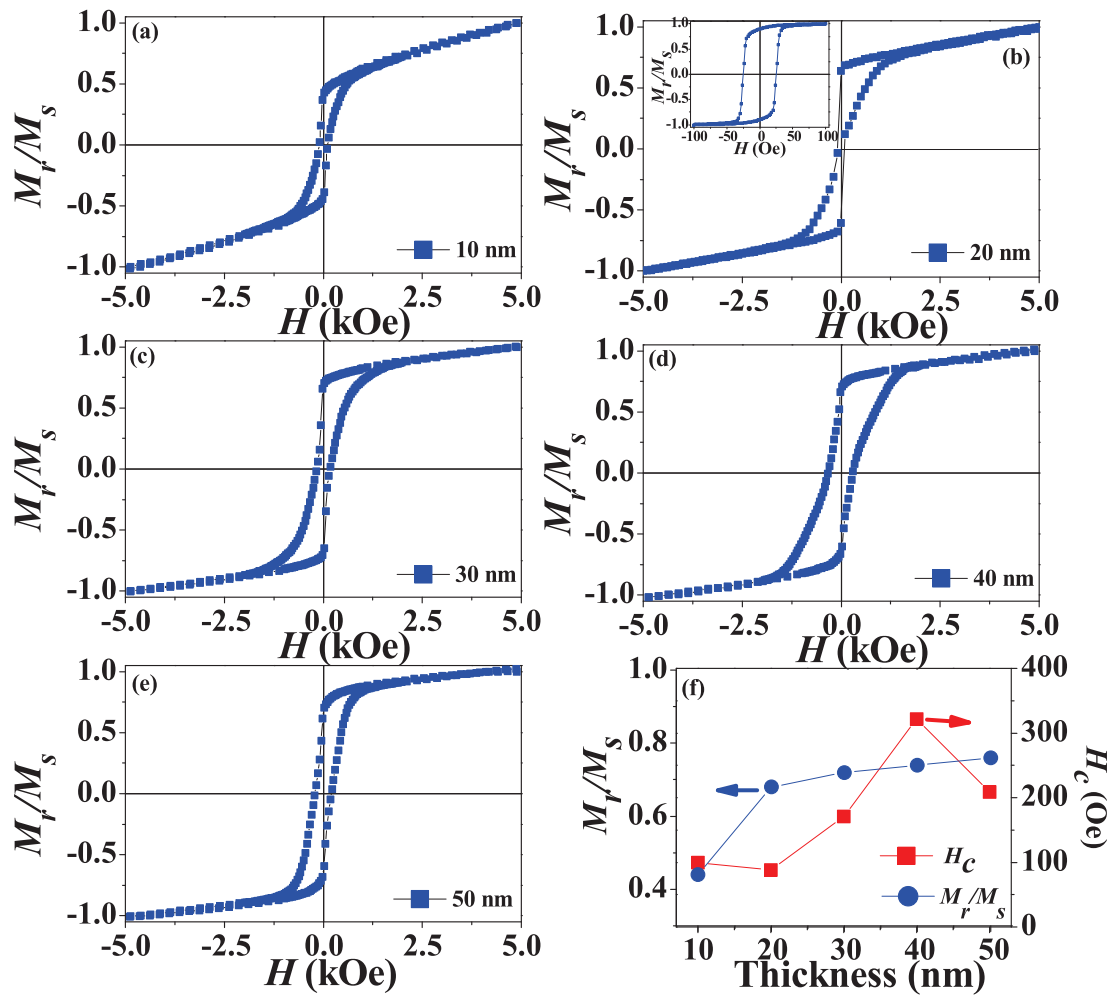


Figure 5.5: Magnetic hysteresis loops of $\text{Co}_{90}\text{Fe}_{10}$ nanodot arrays when the field applied parallel to the film direction (a) 10 nm, (b) 20 nm, (c) 30 nm, (d) 40 nm and (e) 50 nm and (f) M_r/M_s and H_c as a function of thickness.

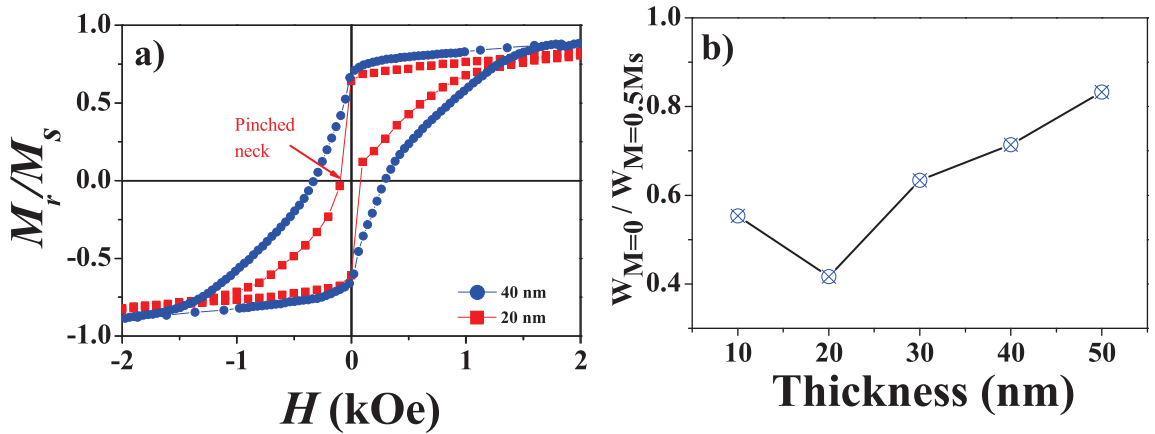


Figure 5.6: Magnetic hysteresis loops of CoFe nanodot arrays when the field applied parallel to the film a) for thickness of 20 nm (pinched neck) and 40 nm, b) show the ratio of $W_{M=0}$ and $W_{M=0.5M_s}$, δ as a function of thickness to represent the pinched neck or the vortex magnetic state in the CoFe nanodot arrays.

Additionally, $M(H)$ loops for field applied perpendicular to film direction was also examined for $\text{Co}_{90}\text{Fe}_{10}$ nanodot arrays with a thickness of 20, 30, and 50 nm, as shown in Fig. 5.7. The non-saturated behavior exhibits zero remanence with zero coercive field at a thickness of 20 nm which indicating the hard magnetization direction in the $\text{Co}_{90}\text{Fe}_{10}$ nanodot arrays. Whereas, with increase in thickness to 50 nm, the small opening near the zero magnetization field was observed with negligible M_r/M_s as shown in Fig. 5.7(b-c). This may be attributed by the shape effect where these dot structures can be elongated along the pore channels to rearrange the easy axis.

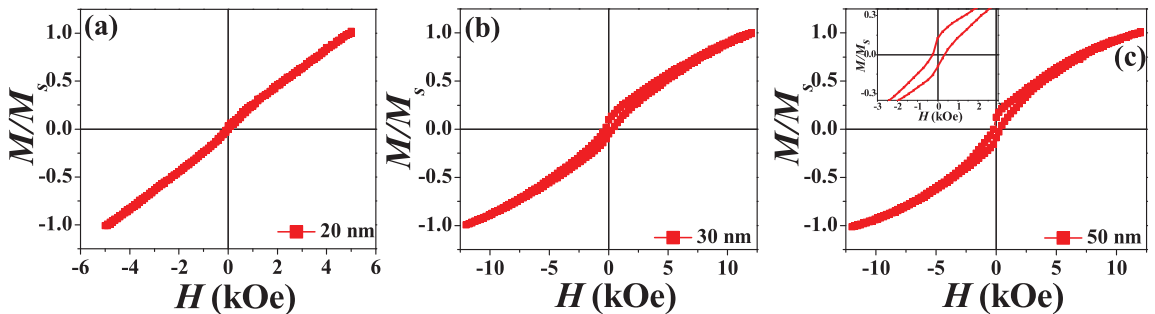


Figure 5.7: Magnetic hysteresis loops of CoFe nanodot arrays when the field applied perpendicular to the film direction; a) 20 nm, b) 30 nm and c) 50 nm.

5.3.3 First order reversal curve (FORC)

Further understanding of the vortex magnetic states in 20 nm $\text{Co}_{90}\text{Fe}_{10}$ nanodot arrays were investigated from the first order reversal curve (FORC), from a set of minor hysteresis loops. The minor hysteresis loops measurement begins by saturating the sample with a large positive applied field H_s . The field is decreased to reversal field H_a and the FORC is defined as the magnetization curve that results when the applied field is increased from H_a back to H_s . This measurement procedure is repeated for different values of H_a to obtain a suite of FORCs (see Fig. 5.8). The magnetization at the applied field H_b on the FORC with reversal point H_a is denoted by $M(H_a, H_b)$, where $H_b > H_a$. Data from consecutive measurement points on consecutive reversal curves are used to determine the FORC distribution, which is defined as the mixed second derivative:

$$\rho(H_a, H_b) = -\frac{1}{2} \frac{\partial^2 M(H_a, H_b)}{\partial H_a \partial H_b} (H_b \geq H_a) \quad (5.3.1)$$

The FORC distribution and related diagram have been calculated using FORCinel (Harrison et al. 2008) which use locally weighted regression smoothing algorithm (LOESS)(Roberts et al. 2000) for the calculation. Usually it is convenient to define a new set of co-ordinates (H_c, H_u) instead of (H_a, H_b) for the representation of the FORC diagram,

$$H_c = \frac{H_b - H_a}{2}, H_u = -\frac{H_b + H_a}{2} \quad (5.3.2)$$

Thus rotating the FORC diagram by 45 from (H_a, H_b) plane to (H_c, H_u) plane (Harrison et al. 2008). We have used both the coordinate system for the discussion of the results. In this measurement $\text{Co}_{90}\text{Fe}_{10}$ nanodot arrays were initially subjected to the maximum field of 2000 Oe, H_s . Afterwards, we have varied the reversal field from 1200 Oe to -2000 Oe with the field spacing of 10 Oe in the previously mentioned manner. The FORC distribution results are given below.

It is well known from the Eqn (5.1), the FORC distribution (ρ) becomes non-zero when the magnetization reversal involves irreversible switching. Whereas, for reversible magnetic switching, there will be no change in the magnetization value $M(H_a, H_b)$ while going from one reversal point to another considering reversible magnetization switching leads to zero FORC distribution. Thus, the magnetization will solely depend on the applied field H_b , making the FORC distribution zero. By using these FORCs, here we are able to examine the nucleation and the annihilation of the vortex magnetization, where there is a reversible and irreversible switching along the field direction.

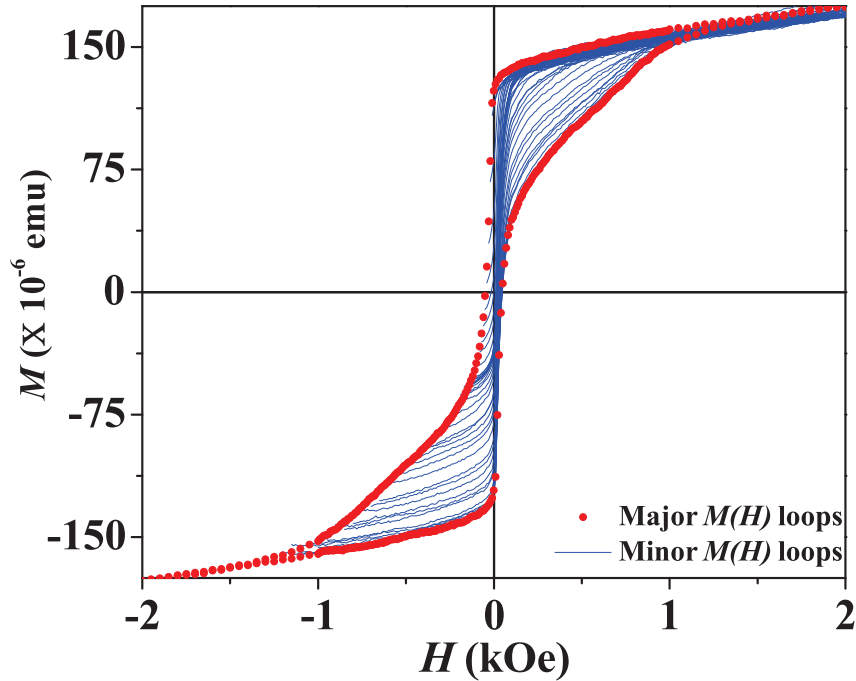


Figure 5.8: Magnetic hysteresis loops of CoFe nanodot arrays for the thickness of 20 nm when the field applied parallel to the film. Red dots indicate the major $M(H)$ loops and the blue continuous line indicates the minor loops for FORC analysis with the field interval (H_a) of 10 Oe.

Figure 5.8 show the experimentally obtained first order reversal curve for 20 nm thick $\text{Co}_{90}\text{Fe}_{10}$ nanodots where the major hysteresis loop delineates the outer boundary for the FORC curve. In this analysis, precise control over the nucleation field and the annihilation field of the vortex magnetization state can be observed. FORCs and the corresponding distributions are shown in Fig. 5.9. The vortex nucleation and the annihilation fields can be identified by the color variation in the FORCs in Fig.5.9(a), color coding represents red for vortex nucleation at where the ρ is positive, and the blue for $\rho=0$ (i.e., for reversible magnetization) and violet is for -ve ρ , which is for the annihilation fields in these nanodot arrays. Whereas, Fig. 5.9(b) is the contour plots of FORC distribution with (H_a, H_b) , and Fig. 5.9(c) representing the same with coordinates of (H_c, H_u) , and Fig. 5.9(d) show the 3D plots of the corresponding FORC distributions. In contour plot of Fig. 5.9(b), two main features were observed, i.e., i) a central peak and ii) the negative-positive region near the bottom left-hand corner of the FORC diagram. The central peak is due to the switching of the magnetization, where the pinched neck is started in $M(H)$ in Fig. 5.5(b) i.e., the nucleation field H_n . For mathematical point of view, this positive peak is associated with the increase in $(\frac{\partial M}{\partial H_b})$ with decreasing H_a . Whereas in terms of H_u and H_c , it showing the non-interacting behavior of the $\text{Co}_{90}\text{Fe}_{10}$ nanodot arrays where $H_u = 0$ Oe and $H_c \sim 20$ nm. This is

expected as for vortex magnetic states, the interaction between the neighboring dots may be negligible. The origin of the negative region is related to sections of the FORCs where $H_b < 0$ (Newell et al. 2005). The occurrence of the negative-positive pairing is a result of the decrease and increase of the reversal field susceptibility as the domain state responds differently with the applied field. This is the onset of the vortex annihilation as the nanodot approaches negative saturation. Until the point -200 Oe, the FORC distribution shows the presence of the irreversible magnetization. If one considers that the nanodot has reached its negative saturation then the irreversible switching will be over and the FORC distribution will be zero and nearly overlap the region $H_a > -20$ Oe. Since the application of the reversal, the field is constrained by the experimental limitation and the features of the sample. We could only concentrate these FORCs from +200 Oe to -200 Oe with H_a of 10 Oe from H_s of 2000 Oe and step of 10 Oe.

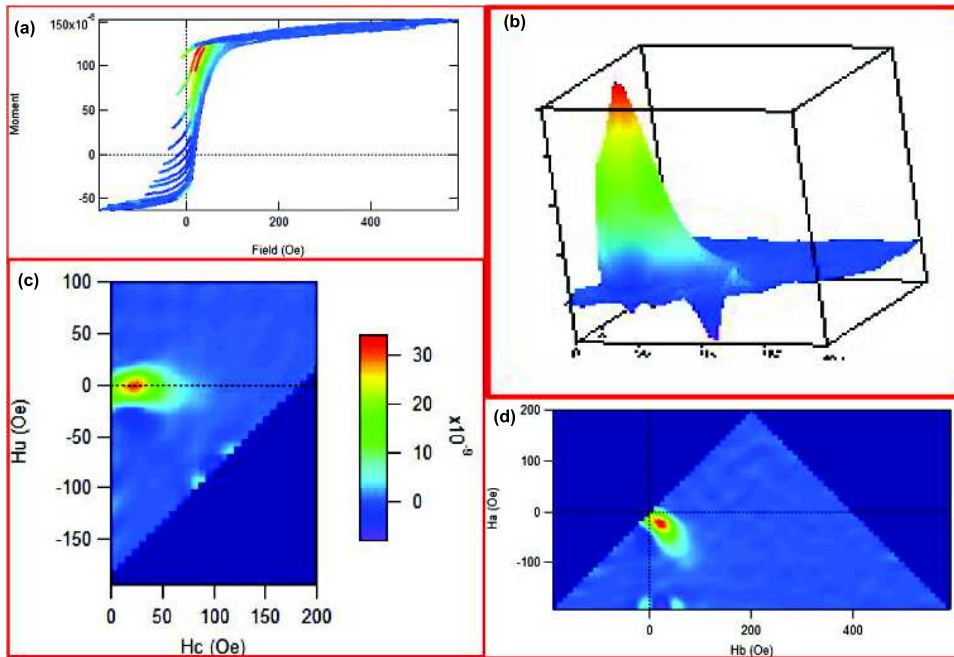


Figure 5.9: Families of FORC distributions: a) minor loops, b) FORCs with coordinates (H_a ; H_b), c) FORCs with coordinates (H_c ; H_u), and d) the 3-D representation of FORC distribution curve.

5.4 SmCo₅ NANODOT ARRAYS

Hexagonal arrays of circular dots with a diameter of 80 nm and a lattice periodicity of 110 nm were patterned by sputtering technique using lift-off process. In this process, the attached alumina membrane was used as an evaporation mask, hence Cr(4 nm)/[Sm(3.2 Å)/Co(6 Å)]₂₀ was sputter coated by the lamination process on Si substrates with 5 × 5

mm² area at 600 °C. This higher substrate temperature helps to relieve the strain induced by lattice mismatch and to improve the adhesion properties of SmCo₅ films. The continuous film was also prepared on the same substrate.

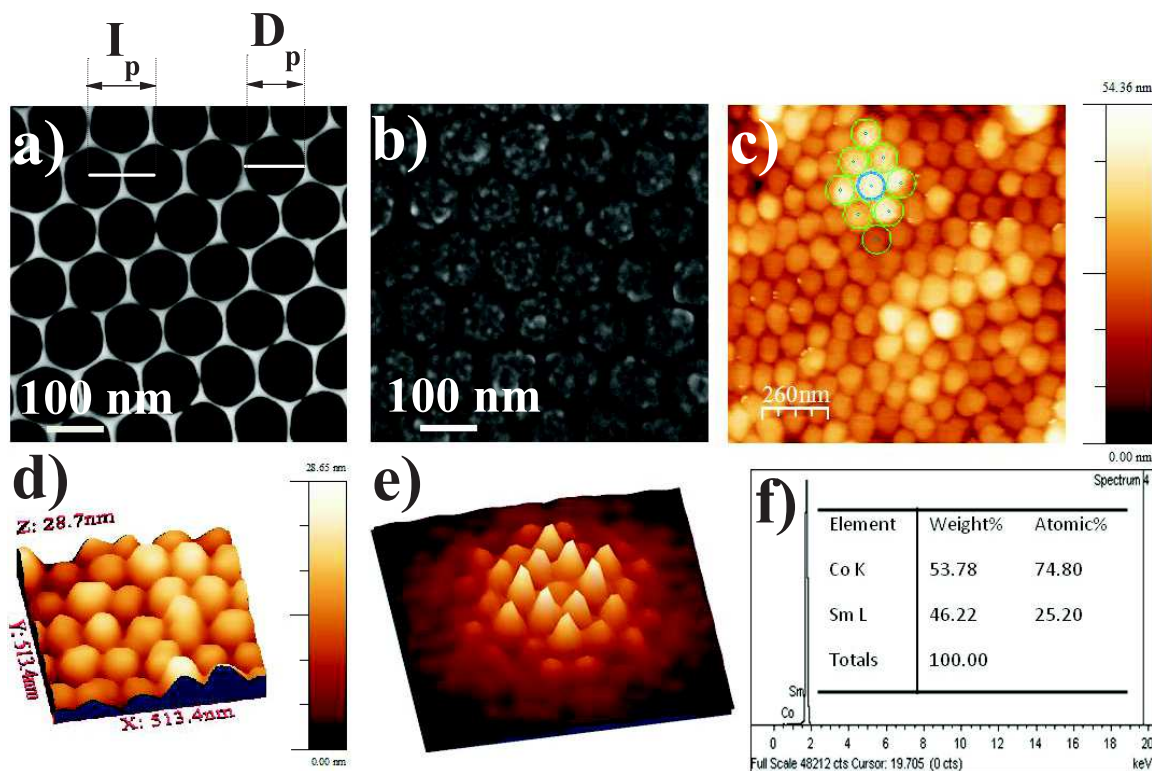


Figure 5.10: Surface morphology of UTAM and SmCo₅ nanodot array using FESEM (a-b) and AFM (c-d) measurements. a) UTAM, b) SmCo₅ nanodot array, c) 1.3 $\mu\text{m} \times 1.3 \mu\text{m}$ scan of AFM topographic images for smCo₅ dots, d) magnified 3D view of (c), e) 3D-FFT image of (b), and f) EDS spectrum of SmCo₅ nanodot array.

5.4.1 Surface Morphology

SEM micrographs of an array of nanopores (UTAM; top view) and of SmCo₅ nanodot array with diameter of 80 nm and periodicity of 110 nm are shown in figures 5.10(a) and (b), respectively. An atomic force image together with its 3-D view was also shown in figures 5.10(c) and (d). The samples were viewed after removal of the UTAM to reveal the hexagonally ordered disc array of the dots i.e., the circular pattern indicates the hexagonal symmetry which is shown in figure 5.10(c). In order to view this hexagonal symmetry, 2D-FFT analysis was also made on the same dot images. The good agreement was observed by the six distinct peaks of 3D view of 2D FFT analysis, shown in figure 5.10(e). The neighboring ring patterns with highly ordered distinct peaks indicate a long range higher order hexagonal symmetry. Moreover, the dot particles were

Table 5.2: Magnetic parameters of SmCo₅ dots and film structure.

Sample name	In-plane			Out- of plane		
	H _s	H _c	M _r /M _s	H _s	H _c	M _r /M _s
	kOe			kOe		
Nanodot array	7.0	3.0	0.90	11.0	1.20	0.40
Thin film	5.0	2.6	0.95	13.0	1.05	0.10

identified and are resulted by the EDS spectra as shown in figure 5.10(f).

5.4.2 Magnetic properties of SmCo nanoDot arrays

5.4.2.1 Vibrating sample magnetometry

Figure 5.11 show the $M(H)$ data of SmCo₅ nanodot array with a film thickness of 20 nm. Here the easy axis of magnetization lies within the film plane as reported earlier (López et al. 2006). The out-of-plane loop is characteristics of a hard axis. In addition to this, the in-plane easy axis hysteresis loop of the dot array is sheared due to magnetostatic interactions between the dots while compared to the hysteresis loop of its film with the same thickness. VSM data on a range of SmCo₅ dot samples gives a value of M_s of 0.2×10^{-3} emu/cm³, 50% of the film, due to the deposition through the membrane and its value of porosity. The magnetization loop has a larger saturation field and a smaller remanent magnetization in dot-array than the continuous film. The larger H_s can be observed due to the smaller separation (i.e., inter-pore distance I_p) in the dot array and its finite size in the sample plane (Ouchi et al. 2010). Consequently, the magneto-static interaction among the dot arrays is influencing to nucleate the dot-array just before the nucleation field of the continuous film (i.e., shearing of $M(H)$ loops in dot arrays). Differences between the dot-array and the continuous film are tabulated in table 5.1. Moreover, the effective anisotropy was also observed less in the dot samples, which is attributed by the higher M_r/M_s given by the formed vortex (pinched neck) magnetization in the dot arrays while the external field applied perpendicular to the film. This pinched neck near zero magnetization can be confirmed when the value is less than 1 (i.e., 0.8) by taking the ratio of $W_{M=0}/W_{M=0.5M_s}$, where $W_{M=0}$, $W_{M=0.5M_s}$ are the widths of the hysteresis loop at zero magnetization, and half the saturation magnetization, respectively. Importantly, the saturation magnetization of the dot arrays were smaller than the film along the perpendicular directions which shows that the film with smaller thickness has not shown the super-para magnetic in nature. Therefore, this can lead into the small change in the effective magnetic anisotropy. It is well known that the domain size of the magnetic states is dependent on the thickness

and the anisotropic energy. From these observed change in magnetic anisotropy might reflect on their magnetic domains observed by MFM analysis.

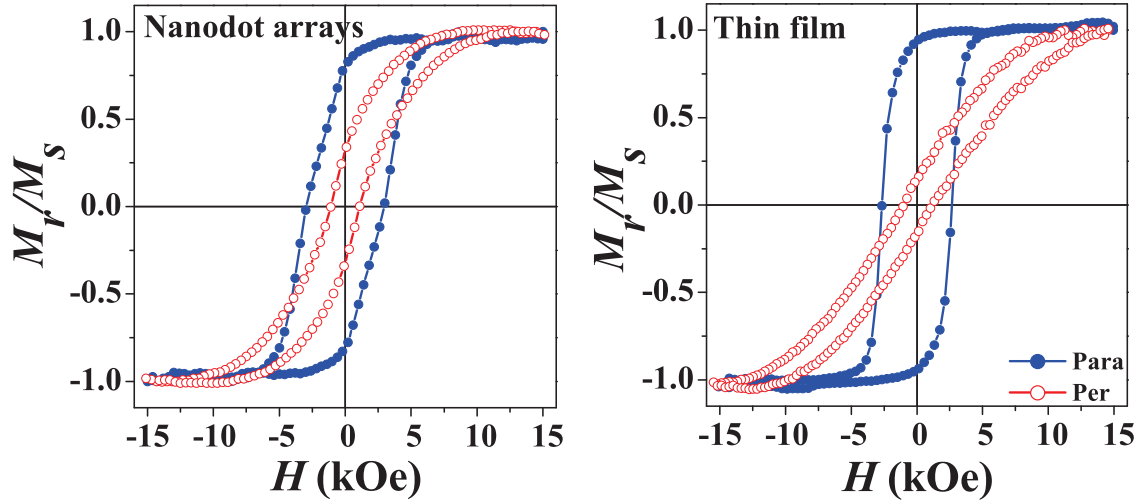


Figure 5.11: $M(H)$ loops of SmCo_5 nanodot arrays and thin film structures with thickness of 20 nm when field is applied along the film and perpendicular to the film direction.

5.4.2.2 Magnetic force microscopy

Scanning probe microscopy images are shown in Figure 5.12. Interestingly, the particles are nearly equal in size while comparing these dot array (Fig. 5.12a) and film (Fig. 5.12g; ~ 70 nm) which may result in the small variation in H_c (i.e., coercivity directly depend on the particle size). These size of the particles was also identified by the color contrast of edge boundary in the phase image shown in Fig. 5.12(b,h). However, the missing higher order hexagonal symmetry in the film exhibits larger magnetic stray field on the surface and it can be seen by the larger magnetic domains in Figure 5.12(i). Controversy to this, the dot arrays are shown uniform magnetic state within the size (i.e., localized magnetization state). The edge effects are clearly visible as a light contrast in the dot samples.

In this process, we expect to have a smaller change in magnetic properties for materials with larger in-plan magnetic anisotropy (Martin et al. 2003) than the soft magnetic material (Fe). There are reports with the pinched neck (i.e., Vortex magnetic state) in the in-plane direction with size-tunable property (Chang-Peng et al. 2006). However, these large in-plane anisotropic materials lead to having an unexpected vortex state in the perpendicular direction and it may be controlled by the size and the separation between the dot arrays. We also have performed dot arrays with a smaller size by varying the pore widening time which results in the non-uniform size of the dot arrays.

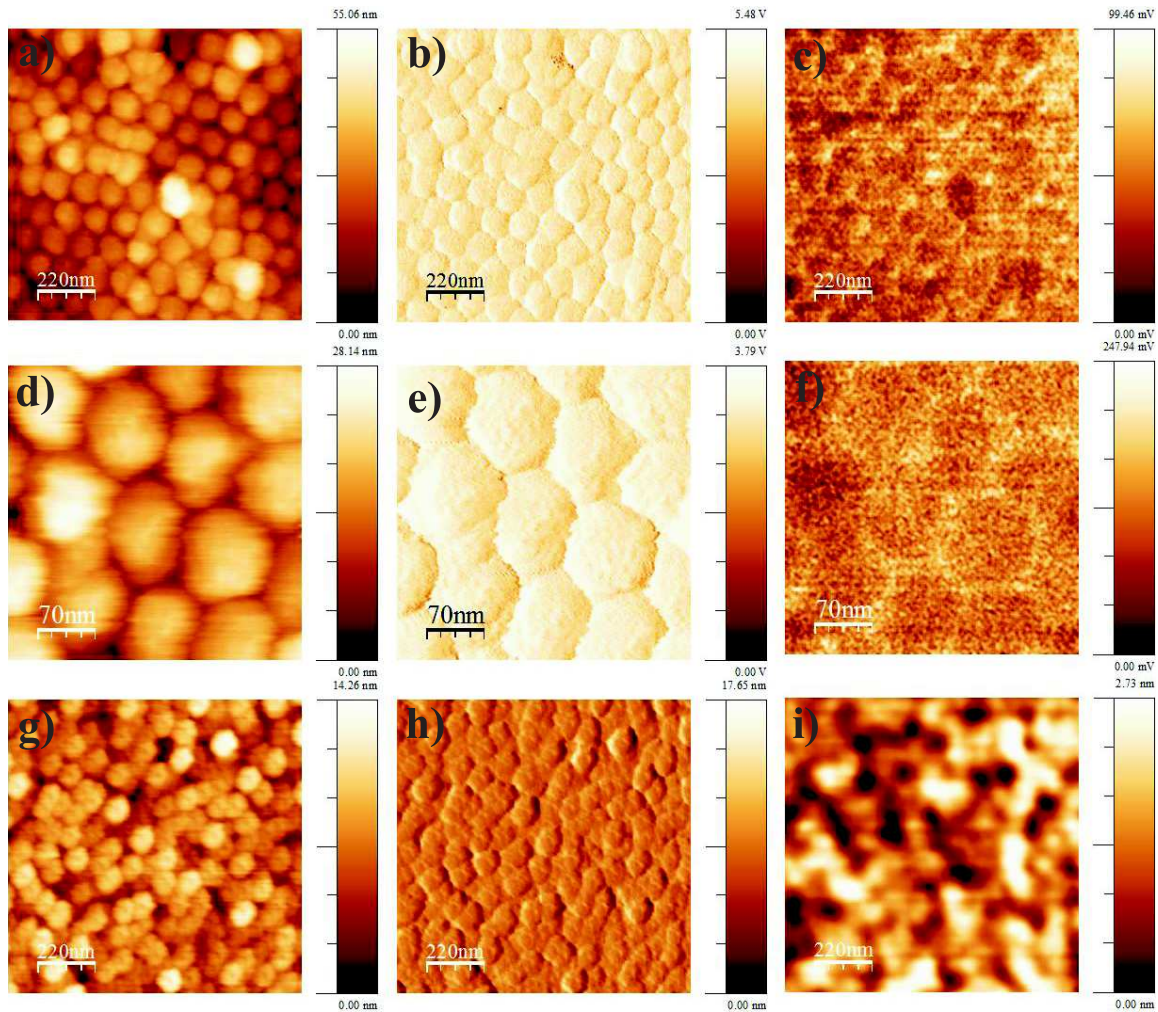


Figure 5.12: Topography (a,d,g), Phase (b,e,h) and MFM (c,f,i) images of SmCo_5 nanodot array (a-f) and thin film (g-i). The scanning area of the sample is $\sim 1.1 \mu\text{m} \times 1.1 \mu\text{m}$ (a-c) and (g-i). Here, (d-f) is the magnified view of (a-c) (i.e., for the area of $350 \text{ nm} \times 350 \text{ nm}$).

5.5 Summary

- Highly ordered pore arrangement of UTAM were successfully fabricated by using two different types of acidic electrolyte bath with thicknesses < 100 nm, via two-step anodization processes.
- Magnetic nanodot arrays of $\text{Co}_{90}\text{Fe}_{10}$, and SmCo_5 were fabricated over a large area using UTAM as an evaporation mask on Si substrate.
- The magnetization reversal via vortex state was observed for $\text{Co}_{90}\text{Fe}_{10}$ with a thickness of 20 nm film with dot diameter of 80 nm.
- Hard magnetic SmCo_5 nanodot arrays with 20 nm thickness show the reduction in the strong in-plane anisotropy in the dot arrays than the film, due to the contribution of the magnetic vortex formation in the perpendicular field direction. The average magnetic domain sizes were as same as the individual dot size, whereas complicated domains were observed in the film. Therefore, the magnetic domains in dots were identically significant for the presence of a single domain magnetic states, however, in the case of film, the formed maze-like domains represent multi-domains structure.

Chapter 6

MICROMAGNETIC MODELING OF MAGNETIZATION REVERSAL IN MAGNETIC CO NANOWIRES

Micromagnetic simulation provides complimentary information to the experimental results about the magnetic reversal process of Co nanowires including different crystalline structures (i.e., for different E_{ma}), such as hcp (002), hcp (100) and fcc (111) phases, along with the shape and the static phenomenon. In this case, hexagonal arrays (i.e., single wire positioned at the middle is surrounded by six nanowires hexagonally) of nanowires are considered to involve the magnetic interactions between the neighboring wires and also within the wire through the magnetostatic field (stray field) in an array of seven or 7×9 number of wires. The effect of both changes in aspect ratio and the crystalline phases are considered for the resultant reversal mechanism and for the effective magnetic anisotropy crossover, as discussed in Chapter 4. In case of former one, the bi-layer crystalline phases of hcp (002) and hcp (100) structures are discussed with their reversal modes, and then, later one is discussed with fcc crystalline phase. Finally, the interpretation of magnetostatic interaction in nanowire arrays of Co hcp (002) phase is demonstrated as a function of the wire diameter and the interwire separation between the nanowires. However, this interpretation is meaningful by considering the term porosity (P) of the AAO membrane or the wire density within a unit area.

6.1 MICROMAGNETISM

In order to understand the magnetic behavior of nanowire array, the reversal magnetization processes have been studied theoretically by both micromagnetic calculations and analytical modeling (García et al. 1999, Han et al. 2003, Vázquez et al. 2004, Escrig et al. 2007, Landeros et al. 2007, Lavin et al. 2009, Han et al. 2009, Bing et al. 2010, Vivas et al. 2011, Pirola et al. 2011, Vivas et al. 2012, Vivas et al. 2012, Vivas et al. 2013). In these studies, emphasis was given on the effect of shape, aspect ratio, crystalline phases etc. However, most of earlier studies upon reversal processes in 1D systems were based on analytical formulae given in Ref. Vivas et al. (2012), which is considered by the angular dependence of magnetic anisotropy. This process has two major drawbacks, (i) it can be applied to a uniaxial system with non-interacting media,

and (ii) it does not include the effect of crystallographic structure on magnetic properties. Therefore, in this study, we have used micromagnetic simulation to understand the reversal mechanism in a 1D system with different crystallographic structures as well as for complex bi-layer structure.

The micromagnetic simulator is a computer based program which carry out micromagnetic simulations. This provides great freedom in the choice of experimental conditions and material parameters, such as object geometry, initial magnetization, the time evolution of the external magnetic field, anisotropy, demagnetization factors, and the exchange interaction. There are several commercial and free software packages available for micromagnetic modeling and simulations, such as OOMMF, Magpar and LLG.

The OOMMF is a freeware for micromagnetic simulation tool, perform based on the finite difference lattice discretization of space and fast Fourier transform (FFT). This firmware is user-friendly and allows the top level scripts to modify or replace. The main developers are Mike Donahue and Don Porter, who made this tool as a free and user-friendly on a wide range of platforms. The aim of this tool is to develop a portable, extensible public domain micromagnetic program and associated tools in the Information Technology Laboratory (ITL) at the National Institute of Standards and Technology (NIST).

Moreover, it is also mentioned that the uncertainty in the material parameters, the inaccurate experimental geometries, and the lack of material inhomogeneities, may lead to limit the micromagnetic simulation do not reproduce the experimental curve quantitatively or reproduce the actual domain structure exactly (Engel-Herbert et al. 2006). However, the simulated results are focused on the experimentally observed $M(H)$ loops in a qualitative way. Therefore, the simulated loop behavior may lead to understand the hysteresis effects by visualization of the magnetization reversal process in arrays of Co nanowires, as discussed in this Chapter.

6.2 BACKGROUND THEORY:

Micromagnetic simulation is developed to describe the macroscopic properties of a ferromagnetic material by simulating the best approximation of the fundamental atomic behavior of the material, by the continuum theory of magnetic moments. This continuum approximation allows the calculation of magnetization structures and magnetization reversal assuming the magnetization (M) to be a continuous function of position (r). In the classical approach, the spin is replaced by classical vector field which initially

allows the determination of magnetostatic fields within the system. Whereas, the quantum mechanical exchange interaction (short range) is limited by the length scale of the continuous material, i.e., $\lambda_{ex} = \sqrt{(2A/\mu_0 M_s^2)}$, where A and M_s are exchange stiffness and saturation magnetization determined by the material property. However, the equilibrium magnetization configuration in the classical micromagnetics is performed by the energy minimization as a function of continuum magnetization \mathbf{M} specified by Brown's equations (Brown et al. 1978), including anisotropy, exchange, self-magnetostatic (demagnetization) and applied field (Zeeman) terms. The detailed magnetic behavior of the given material depends on the balance between these energy terms. Whereas, in micromagnetic simulation, the real nanostructure is decomposed with regular 3D square meshes with each mesh containing 3D magnetization spin vector located at the center of the cell. Then, the reversal magnetization states are predicted by applying the possible dynamic approach; i.e., the magnetization distribution (3D spin relaxation) in the system was then evaluated by integrating the Landau-Lifshitz-Gilbert (LLG) equation:

$$\frac{d\mathbf{M}}{dt} = -\gamma\mathbf{M} \times \mathbf{H}_{eff} - \frac{\gamma\alpha}{M_s} \times (M \times \mathbf{H}_{eff}), \quad (6.2.1)$$

where,

- \mathbf{M} is the magnetization of each 3D mesh,
- \mathbf{H}_{eff} is the effective field of the mesh,
- γ is the gyromagnetic ratio,
- α is the damping coefficient.

The effective field is defined as:

$$\mathbf{H}_{eff} = \frac{1}{\mu_0} \frac{\partial E_{total}}{\partial \mathbf{M}}. \quad (6.2.2)$$

The average magnetic energy density, E_{total} is the addition of the four different magnetic energy contributions as follows:

(i) the magnetostatic energy, E_m , arises due the interaction of the magnetization \mathbf{M} with the demagnetising field, \mathbf{H}_d , which is proportional to induced \mathbf{M} and is defined as (Sellarajan et al. 2013):

$$E_m = -\mu_0 \mathbf{H}_d \cdot \mathbf{M}/2, \quad (6.2.3)$$

(ii) the magnetocrystalline anisotropy energy, E_{an} , arises due to the magneto-crystalline anisotropy of the system and can be written as:

$$E_{an} = K_1 \sin^2 \psi, \quad (6.2.4)$$

where ψ is the angle between the easy axis and the magnetization \mathbf{M} , and K_1 is the anisotropy constant,

(iii) the exchange energy, E_{ex} , originates from the misalignment of a spin with respect to the neighbouring spin and can be written as:

$$E_{ex} = A \sum_{i=1}^3 (\Delta M_i)^2 / (M_s)^2, \quad (6.2.5)$$

and (iv) the Zeeman energy in presence of the external field \mathbf{H} , is defined as:

$$E_{ze} = -\mathbf{M} \cdot \mathbf{H}. \quad (6.2.6)$$

It is to be mentioned that in case of NW arrays, Eqn.(6.2.3) for E_m gets modified as $E_m = -\mu_0(\mathbf{H}_d + \mathbf{H}_{dp}) \cdot \mathbf{M} / 2$, where \mathbf{H}_{dp} is the dipolar interaction field arising due to interaction between neighboring NWs.

Therefore, E_{total} can be expressed as,

$$E_{total} = E_{ex} + E_{demag} + E_{ma} + E_{Zeeman}. \quad (6.2.7)$$

here, the minimization of the ferromagnetic exchange energy aligns the magnetic moments parallel to each other, whereas the minimization of the magnetostatic energy favors the existence of magnetic domains. The magnetocrystalline anisotropy energy describes the interaction of the magnetization with the crystal lattice, which orients the magnetization preferably along certain crystallographic directions. The minimization of the Zeeman energy of the magnetization in an external field rotates the magnetization parallel to the applied field.

In this study, we have performed the micromagnetic simulation using the 3D-OOMMF package (Donahue et al. 2012, Ren et al. 2011) with external field applied in both parallel and perpendicular to the NW axis (Sánchez-Barriga et al. 2009, Vivas et al. 2012). $M(H)$ loops were simulated for applying the external field from +1.5 T to -1.5 T, where the field was reduced with the intervals of 200 steps. While carrying the micromagnetic simulation for an array of seven nanowires or 7×9 no. of wires, each nanowire is segmented with a smaller cubic unit cell with edge the dimension of ~ 3 nm. The magnetization vector (\mathbf{M}) of a unit cell was defined by three components, m_x , m_y , and m_z along the x , y and z axes respectively, whereas z axis lies along the nanowire axis and in the cartesian coordinate system, the angular distribution of each component can be written as:

$$\chi_x = \cos^{-1}(m_x/|M|), \quad (6.2.8)$$

$$\chi_y = \cos^{-1}(m_y/|M|), \quad (6.2.9)$$

$$\chi_z = \cos^{-1}(m_z/|M|), \quad (6.2.10)$$

where χ is the angle between \mathbf{M} and the corresponding axis (x or y or z), $|M| = \sqrt{m_x^2 + m_y^2 + m_z^2}$ and $\mathbf{M} = m_x\hat{x} + m_y\hat{y} + m_z\hat{z}$, where \hat{x} , \hat{y} , and \hat{z} are the unit normal vectors along x , y , and z axis, respectively. Therefore, in this work, evaluation of the reversal mechanism based on the extracted magnetic components in a system of seven nanowire array were evidently shown by respective angular distribution term, χ_i (here, i represents x , y and z). It is to be noted that the center of the bottom of the nanowire was assigned as $x = y = z = 0$.

6.3 MAGNETO-CRYSTALLINE ANISOTROPY

The physical origin of the magneto-crystalline anisotropy energy is the interaction of the mean exchange field and the orbital angular momenta of the atoms in the lattice. This interaction is referred to as spin-orbit coupling, i.e., the electron spin is coupled to the electronic orbital and influenced by the local environment. This deals with the arrangement of atoms in crystalline materials, which energetically prefer certain orientations for easy magnetization. Therefore, the magneto-crystalline anisotropy is closely related to structure and symmetry of the material. For a material with the single easy axis perpendicular to the hard axes (hcp Co) the energy associated with the magnetic anisotropy can be written as:

$$E_{an} = K_0 + K_1 \sin^2 \psi + K_2 \sin^4 \psi, \quad (6.3.1)$$

where K_0 , K_1 , and K_2 are anisotropy constants and ψ is the angle between the magnetization direction and the c -axis.

For cubic material with three easy axes, the anisotropy energy is often expressed as:

$$E_{an} = K_0 + K_1(\alpha_1^2 \alpha_2^2 + \alpha_2^2 \alpha_3^2 + \alpha_3^2 \alpha_1^2) + K_2 \alpha_1^2 \alpha_2^2 \alpha_3^2 + \dots, \quad (6.3.2)$$

where $\alpha_i = \cos \psi_i$ and ψ_i are the angles between the magnetization and the easy axes. In this Eqns., K_0 is independent of magnetization direction and if $K_2 \ll K_1$ then both K_0 and K_2 can be ignored. Therefore, K_1 in J/m^3 is only used, and then if $K_1 > 0$, then the anisotropy axis is an easy axis; if $K_1 < 0$ then the axis is a hard axis.

Table 6.1: Geometry dimension and the magnetic parameters of Co nanowires for hcp and fcc structure.

Crystalline phase	M_s (T)	A (J/m)	K_1 (J/m ³)	diameter (nm)
hcp Co	1.76	$1.3e^{-11}$	$4.5e^5$	70
fcc Co	1.76	$1.3e^{-11}$	$6.7e^4$	45

6.3.1 Effect of crystalline phases in Co Nanowires

Numerous reports were available for the understanding of shape anisotropy in micro-magnetic simulation of Co nanowire arrays. Whereas, in this study, the magnetocrystalline anisotropy energies of hcp and fcc Co phases were investigated to interpret our basic understanding towards the magnetic reversal mechanism for our experimental observations, as a size effect. In this regards, nanowires of single, hexagonal and 7×9 number of nanowires were considered to simulate the data to generate the results. In addition to this, we also knew that the competition between the magnetocrystalline anisotropy and demagnetization energy cannot be neglected when the magnetocrystalline anisotropy energy is comparable to the shape anisotropy energy (for hcp phase); while magnetocrystalline anisotropy energy is less than 10% of shape anisotropy energy (fcc phase), this competition can be neglected in micromagnetics simulation.

The dimension of wire geometry is considered from table 4.1 and the corresponding crystalline structures of bulk Co are given in table 6.1 as A (the exchange constant), M_s (the saturation magnetization), and K_1 (magneto-crystalline anisotropy constant of Co). In this work, the simulation is performed on a hexagonally ordered array of maximum 72 (8×9 matrices) NWs based on the computational facilities currently available. Here, in the simulation, the radius, r , was taken as 35 nm. In the case of hexagonally ordered array structure, the centers of NW axes were kept at a separation, $S=105$ nm.

6.3.2 Magnetic domain structure of hcp Co (002) phase

At the remanent state, the equilibrium state in the nanowire with this structure is found to be a single domain state with the magnetization direction parallel to the easy axis (i.e., along z -axis) Fig. 6.1 for $L=200$ nm. In this case, $\psi = 0$ leads in vanishing the anisotropy energy. Further, due to the parallel spin configuration, the exchange energy also becomes negligible. Hence, the most important energy contribution for the single

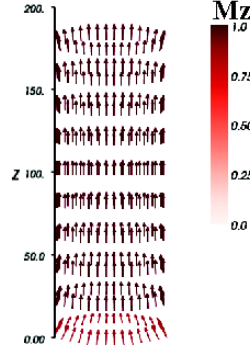


Figure 6.1: NW cylindrical shell at remanent state for $L=200\text{nm}$ with hcp (002) structure showing the magnetic spins parallel to NW axis indicating a single domain magnetic state.

domain state comes from magnetostatic energy due to the existence of the demagnetizing field, H_d , which depends on the net magnetic moment M . The estimated value for 200 nm single nanowire is $E_m = N_d M_s^2 / 2 = 1.44 \times 10^5 \text{ Jm}^{-3}$ with the demagnetization factor, $N_d=0.15$.

In a hexagonal array structure, along with demagnetizing field, H_d , the nanowire experiences a net nonzero field, produced from the superimposition of the field of neighboring nanowires, termed as, dipole interaction field, H_{dp} which depends on both length and separation among the nanowires. The presence of this dipole field enhances the magnetostatic energy in the array structure. For example, in the case of a hexagonal array structure of seven nanowires, E_m was found to be $2.3 \times 10^5 \text{ Jm}^{-3}$, which is almost enhanced by 67% in comparison to the single nanowire structure. Therefore, with reversing the field direction, interaction among nanowires causes several Barkhausen jumps (see Fig. 6.2) due to coherent rotation of individual nanowire which initiate at different switching fields. This can be understood from the simulations by changing the number of NWs in an array. The simulated $M(H)$ data for a single NW are perfectly rectangular (see Fig. 6.2). As the number increases to seven NWs in a hexagon array, the magnetic reversal happens in steps suggesting individual NW reverses coherently at different external fields, H_c^i , which can be defined as (Escrig et al. 2008),

$$H_c^i = H_c^s - H_{int} \quad (6.3.3)$$

where H_c^s is the coercive field of an isolated NW. Here, i stands for the number of NWs in an array. The sign of H_{int} can be negative or positive, however, its magnitude depends on the location and separation with respect to the neighboring NWs and their

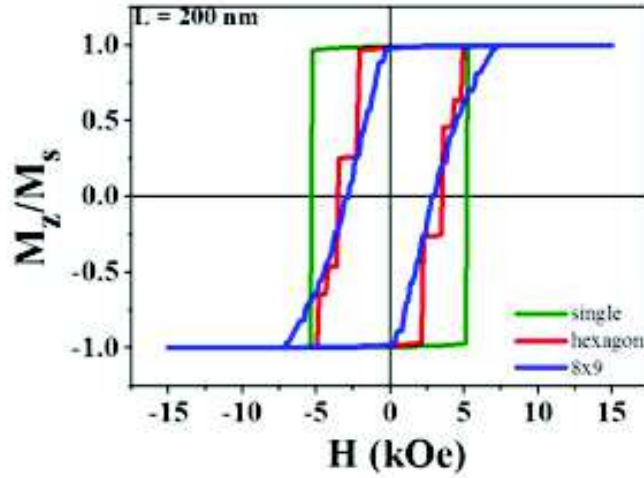


Figure 6.2: shows shearing of $M(H)$ curve with increase in number, i , of NWs in the array structure when the magnetic field is applied along the wire axis.

magnetization directions. For an example, H_{int} is maximum when all the NWs in an array have their magnetization directions parallel to each other (i.e., $M=M_s$). Reversing an NW at a field much lower than H_c^s followed by Eqn. (6.4.1) effectively reduces H_{int} , which is nothing but the step width between successive Barkhausen jumps. With further increase in the number of NWs in the array structure, the $M(H)$ behavior ends with a sheared behavior (see Fig. 6.2 for 8×9 NW array) due to an increase in the number of Barkhausen jumps. This figure also indicates that H_c was found to decrease by 50% with an increase in the number of NWs from single NW to an array of 8×9 NWs, especially at magnetic field applied along the wire axis. To further reduce the discrepancy in H_c between the measured and simulated values, the following factors need to be considered: (i) number of NWs (i.e., 10^8 for an area of $5 \times 5 \text{ mm}^2$ as in real case) in an array, (ii) presence of defects and texture within an NW, and (iii) physical shape variations among the NWs.

6.3.2.1 Angular variation of H_{ext}

Figure 6.3 presents the variation of $H_c(\theta)$ calculated using the analytical formula (Eqn. 1.2.6) along with experimental values. For a comparison, the values of $H_c(\theta)$ obtained from the micromagnetic simulations for single NW as well as seven NWs in a hexagon array are also shown. It is clear from the figure that the shape of the curves for single NW obtained from the analytical formula and by Micromagnetic simulation is matching well. However, substantial changes in $H_c(\theta)$ were observed for seven NWs. From these observations, we conclude that in hcp (002) structure, the reversal mechanism occurs only by coherent rotation of the magnetic moment vectors, not by transverse mode

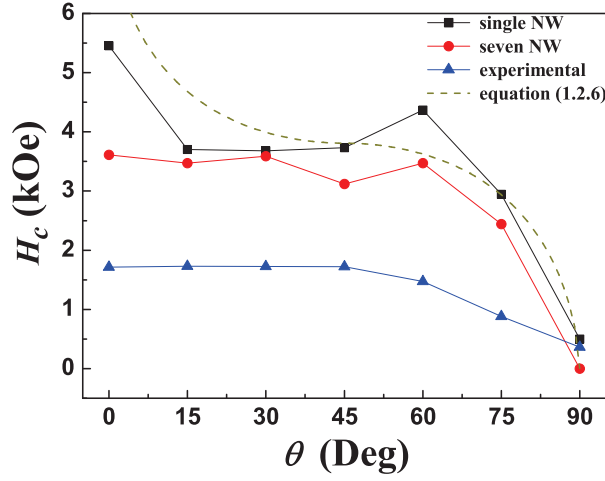


Figure 6.3: Comparison of H_c vs θ curves in case of NW with $L=200$ nm calculated using Eqn. (1.2.6), and by micromagnetic simulation for single NW and seven NWs in a hexagonal array.

as reported earlier. It is to be mentioned here that in the case of hcp (002) structure, micromagnetic simulation for single NW results into a constant H_c value irrespective of the NW length and the reversal process indicated coherent rotation.

6.3.3 Magnetic domain structure of hcp Co (100) phase

The remanent magnetic state of a nanowire with hcp (100) structure was characterized by two vortex states with opposite chiralities separated by domain wall. In this state, the magnetization can be expressed as (Li et al. 2008):

$$M = \sum_N (M_s \cos \chi_i \hat{z} + M_s \sin \chi_i \hat{\phi}) \quad (6.3.4)$$

where χ_i is the angle between M and nanowire axis or of the i^{th} element and it is to be mentioned that the angle χ_i changes from 0° to 90° as one moves from center to the edges, however, along it remains constant. Therefore, a solid nanowire can be defined as a parallel cylindrical shell with constant M . To be a more clear picture, the magnetic state of the vortex was determined by the angular distribution of M along the radial direction with respect to the NW axis, i.e., χ , at the remanence state for different z values (see figure. 6.4(b)). As shown in this figure (inset of Fig. 6.4(b)), for $z = 100$ and 400 , χ changes from 90° to 0° along the radial direction as one approaches towards the center. This implies that along the direction for a constant (r, ϕ) , χ remains unchanged. Therefore, as stated above, a solid NW with hcp (100) structure can be defined as parallel cylindrical shells with constant M (see Fig. 6.4(a)), however at the

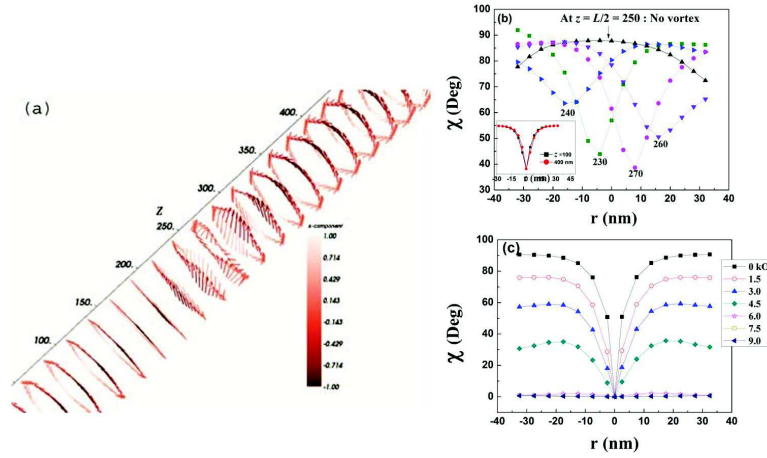


Figure 6.4: (a) NW cylindrical shell of $L=500$ nm with hcp (100) structure at remanent state showing two vortices (clockwise and anti-clockwise) separated by a domain. (b) χ vs r around the middle of the NW with no vortex state at $z=250$ nm. (c) χ vs r showing the decrease in vorticity with increasing the applied field H .

middle, the cylinder is twisted to form a domain.

As shown in Fig. 6.4(b), the domain also can be characterized by a vortex state (Eqn. 6.3.4) for which the center of the vortex is shifted towards the edge (-ve r direction) with clockwise rotation as approaches $L/2$ and vanishes completely exactly at $z = L/2 = 250$ nm. Further increasing z , vortex starts appearing on the other side (+ve r direction) with anti-clockwise rotation and then moved towards the center. For further understanding the reversal mechanism, the radial distribution of χ with increasing the field from 0 (remanence state) to the saturation field is shown in Fig. 6.4(c). Here the field was applied along the direction. From this figure is clear that the intensity of vorticity (i.e. the angular distribution of M) is high at the remanence state and it decreases with the increasing field, and vanishes at the saturation field. Theoretical simulation results for the vortex structure can be correlated with experimentally observed vortex state by using scanning electron microscopy with polarization analysis (SEMPA) in a nanodisk (Chung et al. 2010). Therefore, we can conclude that in pure hcp (100) structure, the reversal mechanism occurs via a process with reducing the vorticity along with the domain wall motion which creates at two ends and annihilate at the center of the NW.

6.4 COMPARISON WITH EXPERIMENTAL RESULTS

6.4.1 Mixed state with both hcp (002) and hcp (100)

Considering the above-simulated observations for hcp (100) and (002) structures and to correlate with both structural and magnetization data, three different structures were

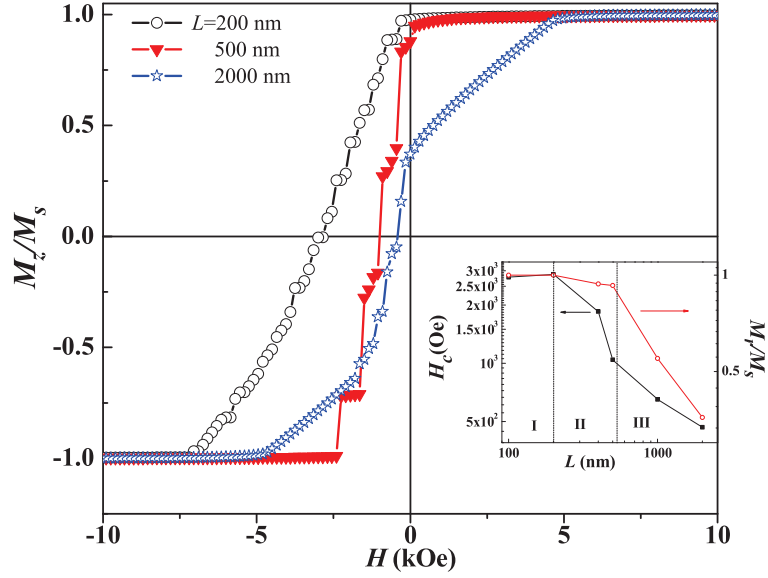


Figure 6.5: shows the simulated $M(H)$ curves as a function of L with average diameter of 70 nm and 20 nm spacing with field applied in longitudinal direction. Inset: simulated values of H_c and M_r/M_s as a function of L .

defined in three regions. For the nanowires, with $L < 300$ nm (region I), the structure is considered to be hcp (002) with the crystallographic c -axis in the longitudinal direction. In region II, with $300 \text{ nm} < L < 500 \text{ nm}$, the texture is defined as hcp (002) up to initial 300 nm and a mixture of hcp (002) and (100) with an equal percentage for the remained nanowire length. While simulating the region III ($L > 500$ nm), hcp (100) texture is assigned for the length above 500 nm along with the same texture as given for region II.

The simulated $M(H)$ curves for the structures corresponding to three different regions are given in Fig. 6.5. It is to be mentioned that the structure considered here as hexagonally ordered array of seven nanowires. The inset of Fig. 6.5 gives the simulated values of H_c and M_r/M_s as a function of L . In region I, both simulated values of H_c and M_r/M_s show independent of the nanowire length as observed experimentally. This strongly supports our structural observations of hcp(002) growth at the bottom of the nanowire. However, the observed large discrepancy in H_c values in between simulated ($H_c=3.1$ kOe) and experimental (~ 1.6 kOe) results may be due to the presence of the defects and additional dipolar interaction field due to a large number of wires (10^8 nos. for an area of $5 \times 5 \text{ mm}^2$) in the arrays.

Moreover, the magnetization distribution (M) of z -component for the three segmented NW of length 1000 nm is shown in Fig. 6.6(a) at $H=0$ (remanent). In this figure, the distribution is shown only for an outer cylindrical shell for better clarity,

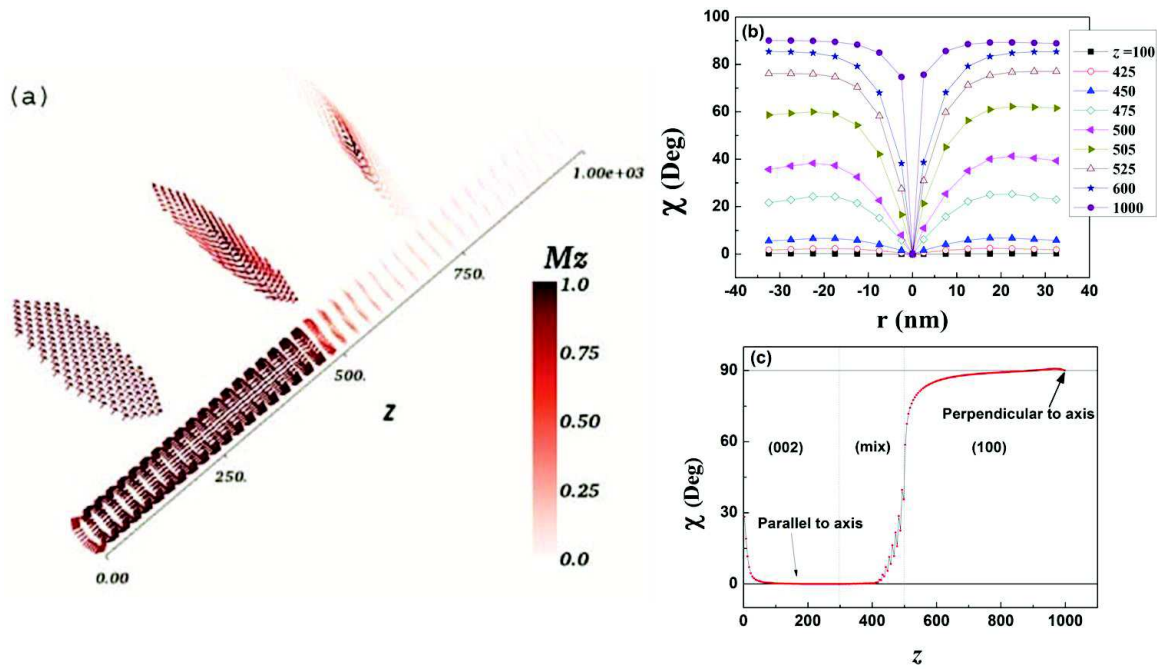


Figure 6.6: (a) NW cylindrical shell of $L=1000$ nm with hcp (002) and (100) structures at remanent state. (b) The variation in χ with r , showing coherent structure ($\chi=0^\circ$) at lower z values ($z < 400$ nm) and the appearance of vortex for $z > 400$ nm. (c) Variation in χ with z indicating interaction region among two magnetic states along NW axis.

though the actual simulations are carried out on a solid cylinder. Three planar sections with M_z component for three different z -values are shown in the same figure. From these views, we can infer that NW of length 1000 nm with three segments has following magnetic moment distributions; (i) lower segment of length 300 nm with hcp (002) structure shows that moment vectors are aligned parallel to each other and to the z -axis, i.e., NW axis and it known as a coherent state, (ii) middle segment of length 200 nm with equal percentage of hcp (002) and (100) structures shows a gradual change from coherent to vortex state and (iii) upper segment of length 500 nm with hcp (100) structure shows a dominant magnetic vortex state. Figure 6.6(b) presents χ along the radial direction for different z -values. This figure clearly indicates that whole length of NW can be divided into two segments with respect to the magnetic state. First, a lower segments of length 400 nm dominated by the coherent state. Then, with further increasing the z value vortex starts appearing and the intensity of the vorticity increases with increasing the length and reaches to 90% of its maximum value at a length of 600 nm (see Fig. 6.6(c)). These results imply that a mixed state with equal percentage of hcp (100) and hcp (002) structures can be represented by gradual crossover from a coherent state to a vortex state. Interestingly, in the upper segment of this bilayer structure no domain was formed as observed in the case of single hcp (100) structure (Fig. 6.4(a)).

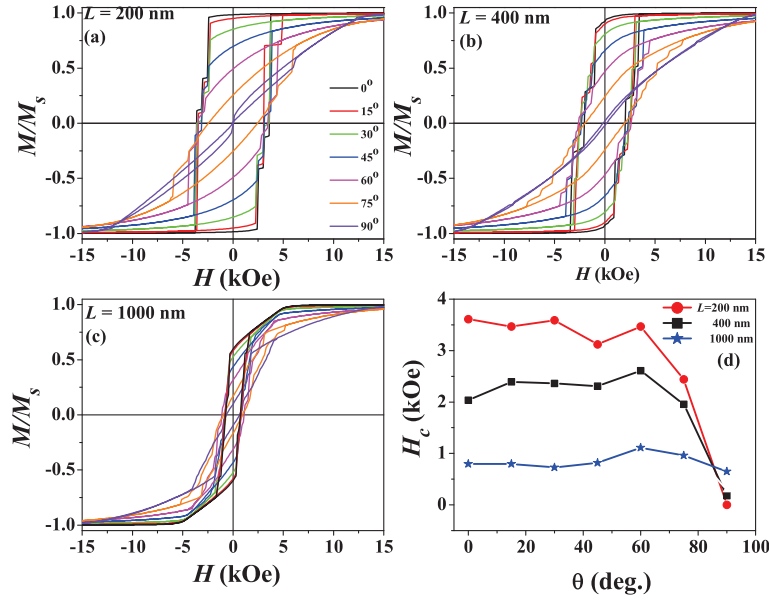


Figure 6.7: Simulated $M(H)$ curves for different θ values: (a) $L=200$ nm (with hcp (002) only), (b) $L=400$ nm (with 300 nm of hcp (002) and 100 nm mix state of hcp (002) and hcp (100)), and (c) $L=1000$ nm (with 300 nm of hcp (002), 200 nm mix state of hcp (002) and hcp (100) and remaining 500 nm of hcp (100)). (d) simulated H_c vs θ for different NW lengths.

Figures 6.7(a)-(c) present the simulated $M(H)$ curves for three different wire lengths, 200, 400, and 1000 nm, respectively, with hexagonal ordered an array of seven NWs. $M(H)$ curves presented here are simulated with varying θ between 0° to 90° with respect to the NW axis. Similar to the experimental results (see Figs. 4.4(a)-(c)), $M(H)$ curves show a systematic decrease in the hysteresis loops with increasing θ . The variation of H_c as a function of θ for three different wire lengths is shown in Fig. 6.7(d). It is interesting to see that the behaviors of H_c for $L=200$ and 400 nm are similar to those of experimental ones (see Fig. 4.4(d)). However, the coercivity values extracted from the simulated curves are almost two times larger in comparison to the experimental values. This may be due to the possibility of the no. of wires, texture defects and the physical shape variation in the system as discussed earlier. Moreover, for $L=1000$ nm, the coercivity values are very close to the experimental one.

6.4.1.1 Energy density contributions

It is equally important to see the change of different energy density contributions defined by Eqns. (6.2.3-6.2.6) with texture orientations. Figure 6.8 presents comparative bar diagram with different energy contributions at remanent state for NWs having lengths $L=200$, 400, and 1000 nm. Since at the remanent state $H=0$, E_{ze} becomes zero. Now,

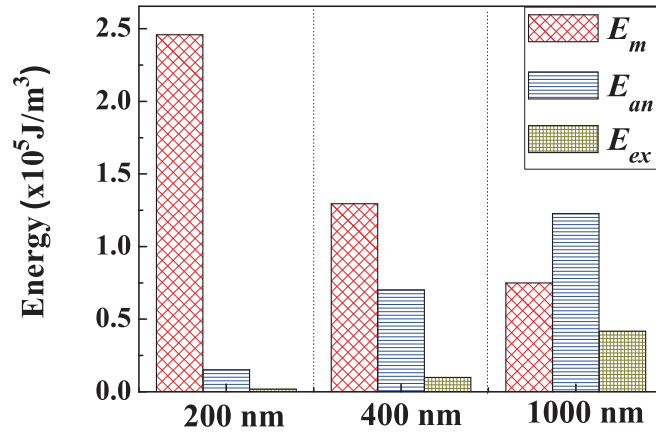


Figure 6.8: Different energy contributions in three cases of $L=200$, 400 , and 1000 nm at remanent state.

for NW with only hcp (002) structure, spins are aligned parallel to each other (see Fig. 6.1) (i.e., coherent state) with $\chi=0$, both E_{an} and E_{ex} become negligible. However, the magnetostatic energy, $E_m \sim 2.45 \times 10^5$ J/m³, was found to contribute dominantly. This dominance of E_m gives better squareness ($M_r/M_s=1$) with highest H_c as can be seen in Fig. 6.7. In the case of $L=400$ nm, as explained earlier, the structure represents 100 nm mix region on the top of 300 nm hcp (002). This provides 15% volume contribution of hcp (100) structure in the whole 400 nm length. But interestingly, it decreases E_m by almost 50% to 1.3×10^5 J/m³ as spins in mix region start curling, losing the perfect coherent structure. This can be seen as E_{ex} starts appearing ($\sim 9.9 \times 10^3$ J/m³) along with E_{an} ($\sim 0.7 \times 10^5$ J/m³). It is to be mentioned here that, though the curling of spins started, the magnetization reversal is still dominated by coherent rotation as $M_r/M_s \sim 1$ with reduction of H_c by a factor of 1.5. For NWs, with $L=1000$ nm, hcp (100) dominates the structure. This gives highest E_{an} ($\sim 1.3 \times 10^5$ J/m³) among all three cases studied here as the hcp (100) structure has an easy axis of magnetocrystalline anisotropy perpendicular to wire axis giving $\chi=90^\circ$. A single vortex appears in 1000 nm, as explained earlier, which enhances E_{ex} to its maximum value ($\sim 0.43 \times 10^5$ J/m³).

6.4.2 Magnetic domain structure of fcc Co (111) phase

The diameter, D , was taken as 45 nm and the separation between the nanorod was kept at $S \sim 66$ nm. We have considered the parameters of bulk Co, namely, the exchange constant, $A = 1.3 \times 10^{-11}$ J/m, the saturation magnetization, $M_s = 1.76$ T, and the magneto-crystalline anisotropy constant, $K = 2.7 \times 10^5$ J/m³ for Co fcc-phase (Vivas

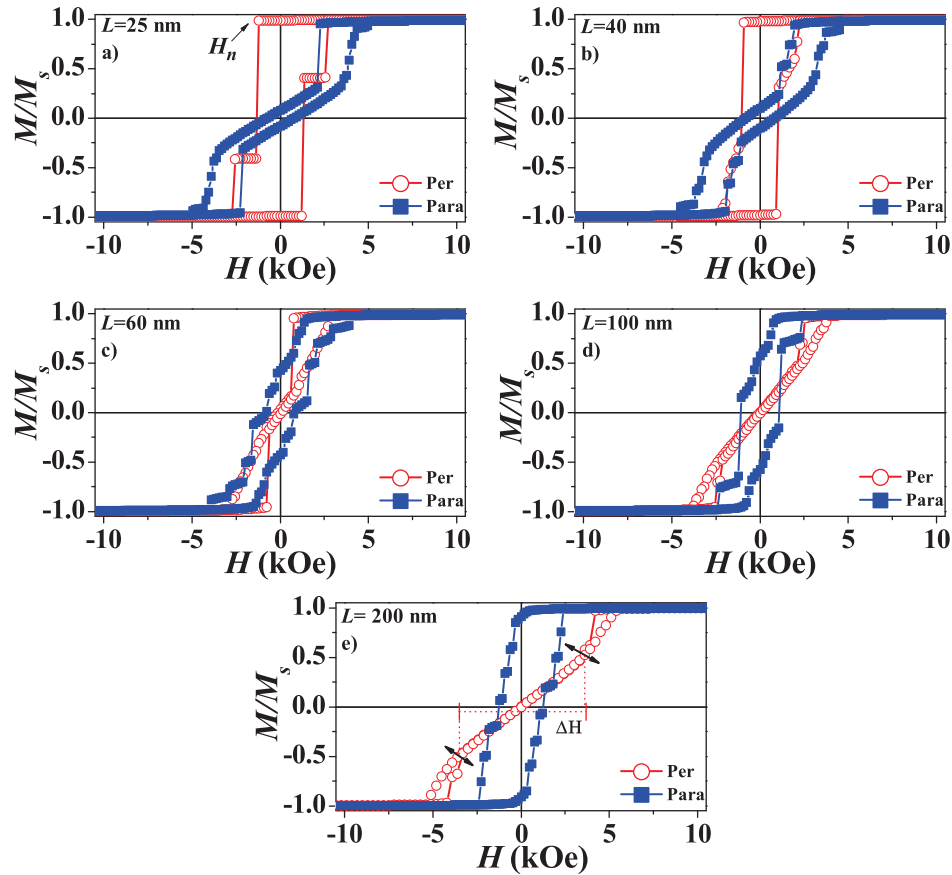


Figure 6.9: $M(H)$ loops obtained from the micro-magnetic simulation with field applied parallel and perpendicular to the rod axis for variable nanorod lengths (L); a) $L=25$ nm, b) $L=40$ nm, c) $L=60$ nm, d) $L=100$ nm, e) $L=200$ nm.

et al. 2011, Jamet et al. 2000). Figure 6.9 presents the simulated $M(H)$ loops for different values of L in the range between 25 to 200 nm. In this figure, the simulated $M(H)$ loops for field applied parallel and perpendicular directions to the nanorod axis are shown. Similar to the experimental results (see Figs. 4.7(a)-(c)), $M(H)$ curves show a systematic modification of easy axis from in-plane(perpendicular to nanorod axis) to out-of-plane magnetization while increasing the length of the rod. The extracted H_k values from these simulated curves are plotted in Fig. 4.8(b). It is interesting to see that, the simulated curve for H_k matches quite well with the experimental one and the critical crossover length, L_c , was estimated to be around 77 nm. This value is very close to the experimental one. The origin of this good agreement between the theory and the experimental results is due to the critical nature of magnetization reversal process which is explained below. The angular distribution of M vector is used to explain the magnetic reversal process of nanorods in both H_{ext}^{\parallel} and H_{ext}^{\perp} directions, respectively.

6.4.2.1 External magnetic field applied perpendicular to nanorod axis

For $L = 25$ nm, the simulated $M(H)$ loop shows a sharp transition at a nucleation field, $H_n = -1200$ Oe due to the coherent transition of magnetic spin vectors (Fig 6.9(a)). This is expected as for a circular disc with $L/D \ll 1$, the shape anisotropy dominates in-plane easy axis and causes the coherent spin reversal at this switching field. However, with increasing the nanorod length to $L = 40$ nm, the nucleation field was shifted towards less negative value and occurred at $H_n = -900$ Oe (Fig. 6.9(b)). Unlike $L = 25$ nm, this transition in $M(H)$ loops was found to be due to the creation of a vortex state within nanorods in the xy -plane and with further increasing the applied field towards the negative saturation field value, H_s , a process of vortex annihilation was depicted by a long tail in this $M(H)$ loop. Figure 6 (a) shows a 3D view of z -component magnetic distributions (outer shell) within a nanorod at a field of -900 Oe, presenting the vortex configuration in the xy -plane. For further clarity, a 2D view of spin distribution on the xz -plane with $y = 0$ is shown in the inset of the figure. This figure clearly indicates that the vortex having a center core whose m_z component lying along the negative z axis. Fig 6.10(b) shows the angular distribution, $\chi_z(r)$, of \mathbf{M} vector extracted for different z values from a nanorod. This predicts that the vortex intensity is uniform irrespective of the z values and the switching of vortex core in negative z direction, i.e., $\chi_z(r) = 180^\circ$ at $r = 0$ occurs at the nucleation field itself. The origin of such vortex formation for $L = 40$ nm is due to both the shape and magnetocrystalline anisotropies in the system.

For $L > D$, the simulated $M(H)$ loops showed a sharp transition at H_n followed by a reversible region with $M_r^\perp = 0$. While analyzing these $M(H)$ behaviors with an increase in rod length, the following observations are made: (i) the value of H_n shifted towards higher +ve field values, (ii) the width of the reversible region (ΔH) increases, and (iii) the percentage of drop in M at H_n decreases. These observations made with an increase in rod length were found to be due to the change in spin configuration within a nanorod/nanorod array as discussed below.

For $L = 60$ nm, the vortex nucleation within nanorod array initiates at 700 Oe and results in sharp fall in magnetization value by 80 %. Then, M follows a reversible behavior and maintains a linear relationship with the decreasing field till $H = -700$ Oe. With further decreasing in the field, the deviation from the linearity indicates the beginning of vortex annihilation process. In the reversible region, it was observed that the hexagonal symmetry of the nanorods and the magneto-static interaction among them make to initiate the vortex chiralities within a nanorod either in xy , yz or xz planes, keeping equal percentage of contribution in m_x as a function field H . Figure 6.10(c)

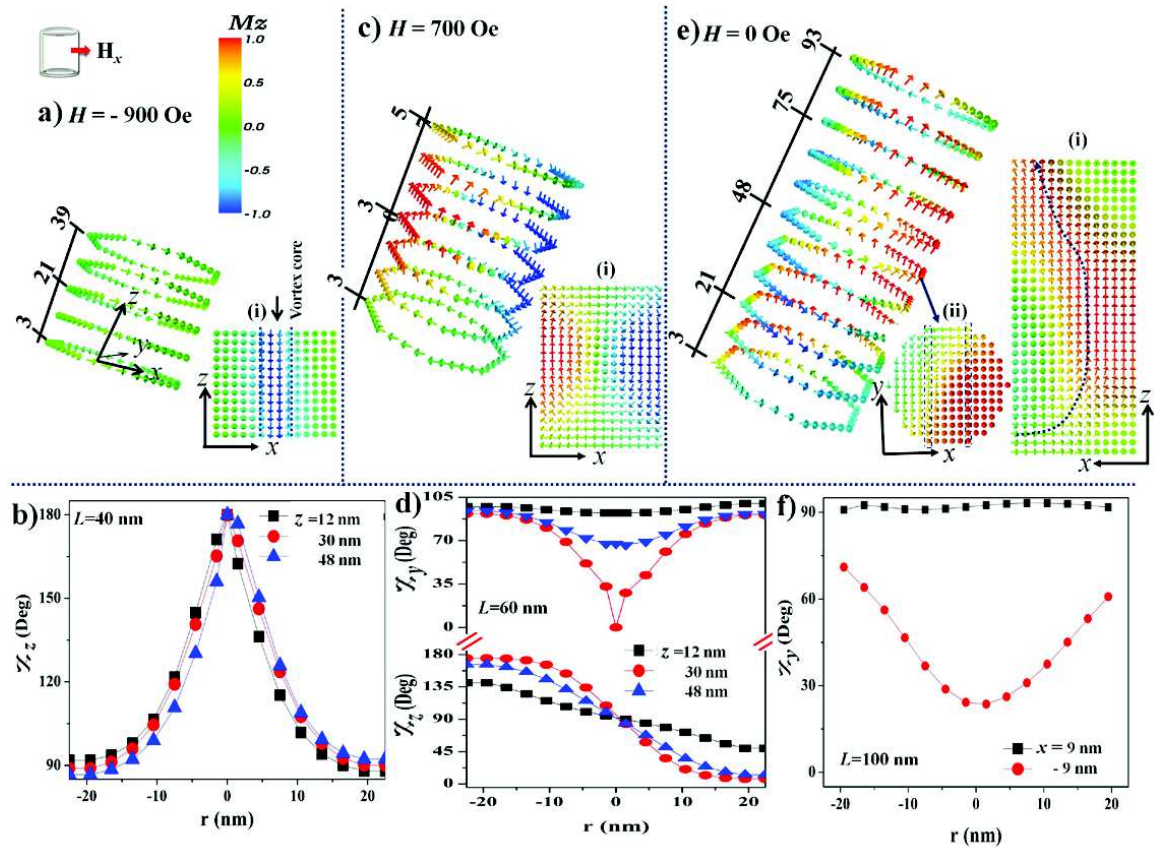


Figure 6.10: shows 3D view of z -component magnetic distribution a) for nanorods with L ; a) 40 nm at $H = H_n$, c) 60 nm at $H = H_n$, and e) 100 nm at $H = 0$ Oe, respectively. The outer shell of the cylindrical rod is shown here for better clarity. The arrows schematically indicate the magnetization direction and the colors indicate the longitudinal magnetization, M_z . The external field applied here was perpendicular to the rod axis. Inset (i) shows the 2D xz -plane at $y=0$, for solid cylinder of the same rod. Inset of Fig. 6(e)(ii) presents 2D view in xy plane at $z=48$ nm to represent the C-state. The variation of χ_i vs r along the length of the rod in the xz plane at $y=0$ was shown in (b) and (d) for corresponding Figs. (a) and (c), respectively (Here i represents y and z). Fig. 6(f) shows the angular variation of \mathbf{M} vector at $x=9$ and -9 nm, which is shown by the dotted line in inset (ii).

shows 3D view of z -component magnetic distributions (outer shell) within a nanorod at a field of 700 Oe, presenting the vortex configuration in the xz -plane. Two-dimensional representation of the \mathbf{M} vector in xz -plane at $y=0$, shown in the inset of fig 6.10(c) further confirms the presence of vortex structure with the core along the y direction. The values of χ_y and χ_z extracted from this plane from different z -values are shown in Fig 6.10 (d). At $z = 30$ nm, i.e., at the middle of the nanorod, $\chi_y(r)$ represents the vortex structure with angular variation from 0 to 90°, whereas the change of $\chi_z(r)$ from 0 to 180° confirms the vortex chiralities around a y axis.

For $L = 100$ nm, with $L \gg D$, the shape anisotropy dominates and causes to align the magnetic spins along the z axis. This results in a shift of H_n towards higher +ve value to 2510 Oe. At this field, the nucleation initiates with two different spin configurations among the nanorods: (i) inhomogeneous twisting of magnetic spin distributions (\mathbf{M}) around the rod axis, as shown in Fig. 6.10(e) for $H = 0$, and (ii) initiation of spin flipping along the z -axis in the xy -plane located at the center of the nanorod (not shown here). In the case of former one, the spin distribution is in "C" state within the xy plane for $z = 48$ nm (see inset (i) in Fig. 6.10(e), whereas along the rod axis, they are confined in "S" state (i.e., in the xz -plane, see inset (ii) of Fig. 6.10(e)) as reported previously (Scholz et al. 2003). Fig. 6.10(f) presents the variation $\chi_y(r)$ extracted from the inset (i) of Fig. 6.10(e) for two different x values to further quantify the "C" state. For $x = -9$ nm, $\chi_y(r)$ shows a variation in angle from 75 to 15° along the radial direction confirming the rotation of \mathbf{M} vector within the xy -plane. Whereas for $x = 9$ nm, a constant $\chi_y(r) = 90^\circ$ indicates \mathbf{M} vector along z -axis, which moves towards the edge during the annihilation processes. In the case of later one, with decreasing field, the progress of spin flipping moves towards both top and bottom ends in antiparallel configuration with its nearest neighbor and form a flux closure pattern at the end.

Further increase in L to 200 nm, the formation of vortex structure is fully disappeared. Rather, the reversal process initiates with spin flipping along the z -axis in the xy -plane located at the center of the nanorod as observed in some of the nanorods with 100 nm in length. It is to be mentioned that the spin-flipping always occurs simultaneously with its neighboring rod in the antiparallel configuration. In the reversible region, the linearity of $M(H)$ loop was nothing but due to the rate of change of spin flipping towards z -axis with decreasing the field value.

While comparing the experimentally observed $M(H)$ behaviors with the simulated curves for nanorod lengths of 25 and 40 nm, we concluded that for $L \ll D$, in-plane easy axes are confined within a plane, however, as L approaches D , the simulated results predict that the magnetization reversal processes are dominated by the creation and annihilation of vortex structure in the nano-rod. It is to be noted that the signature of

vortex propagation in experimentally measured $M(H)$ loops is not very clear, however low saturation field, large M_r^\perp/M_s , and comparatively the sharp transition indicates the average effect in the magnetization measurements from the nanorod array. In case of nanorod arrays with $L > D$, we have not observed any signature of reversal behavior in experimentally measured curves. However, the decrease in M_r^\perp/M_s with an increase in rod length, shows a qualitative agreement with the simulated behavior.

6.4.2.2 External magnetic field applied parallel to nanorod axis

For field parallel to the rod axis, the simulated $M(H)$ loops for nanorod length varying from 25 to 200 nm are shown in Fig. 6.9(blue square). With $L < D$, i.e., for the nanorods with lengths of 25 and 40 nm, initiation of vortex formation with respect to the z -axis occurs at nucleation fields, H_n , of 2250 and 1990 Oe, respectively, followed by a sharp drop in magnetization values by 70 %. At this nucleation field, the remaining 30 % of net m_z contribution comes from the angular distribution of \mathbf{M} vector along the radial direction, i.e., for constant z -value. The spin distribution along the outer shell of a nanorod at $H = 2000$ Oe is shown in Fig. 6.11(a). As shown in the inset of Fig. 6.11(b), for $z = 12, 21$ and 30 nm, $\chi_z(r)$ changes from 90° to 0° along the radial direction as one approaches towards the center. This implies that along the z direction for a constant (x,y) co-ordinate, χ_z remains unchanged. Therefore, a solid nanorod with fcc (111) structure can be defined as parallel cylindrical shells with constant \mathbf{M} as reported for a case of hcp (100) (Sellarajan et al. 2013, Kulkarni et al. 2013). With further decreasing in the field, M vs H shows a linear relationship. This can be correlated with the change in the rate of change of angular distribution of \mathbf{M} vector, i.e., $\partial\chi_z/\partial(r)$ along the radial direction. When the field increases in reverse direction, the \mathbf{M} vector initiates its rotation towards negative z -direction from the edges (see Fig. 6.11(b)), whereas the core size reduces in diameter (shadow region) with reduction in +ve m_z contribution. At $H = H_c$, the coercive field, with an equal contribution of negative m_z from the larger outer shell and +ve m_z from the shrinkage core makes the net m_z to zero value. When the external field becomes strong enough, the vortex annihilation starts and the reversal process completes with the annihilation of the vortex from all nanorods giving $M = -M_s$.

For $L \gg D$ the simulated $M(H)$ shows several Barkhausen jumps in the $M(H)$ loops, as shown in Fig. 6.9(c)-(e). For $L = 60$ nm, the reversal process occurs with two different spin configurations: (i) formation of a single vortex within a nanorod as mentioned above for $L = 40$ nm, and (ii) two vortices with opposite chiralities (clockwise and anti-clockwise) separated by a domain at the center of the nanorod, as shown in Fig. 6.11(c).

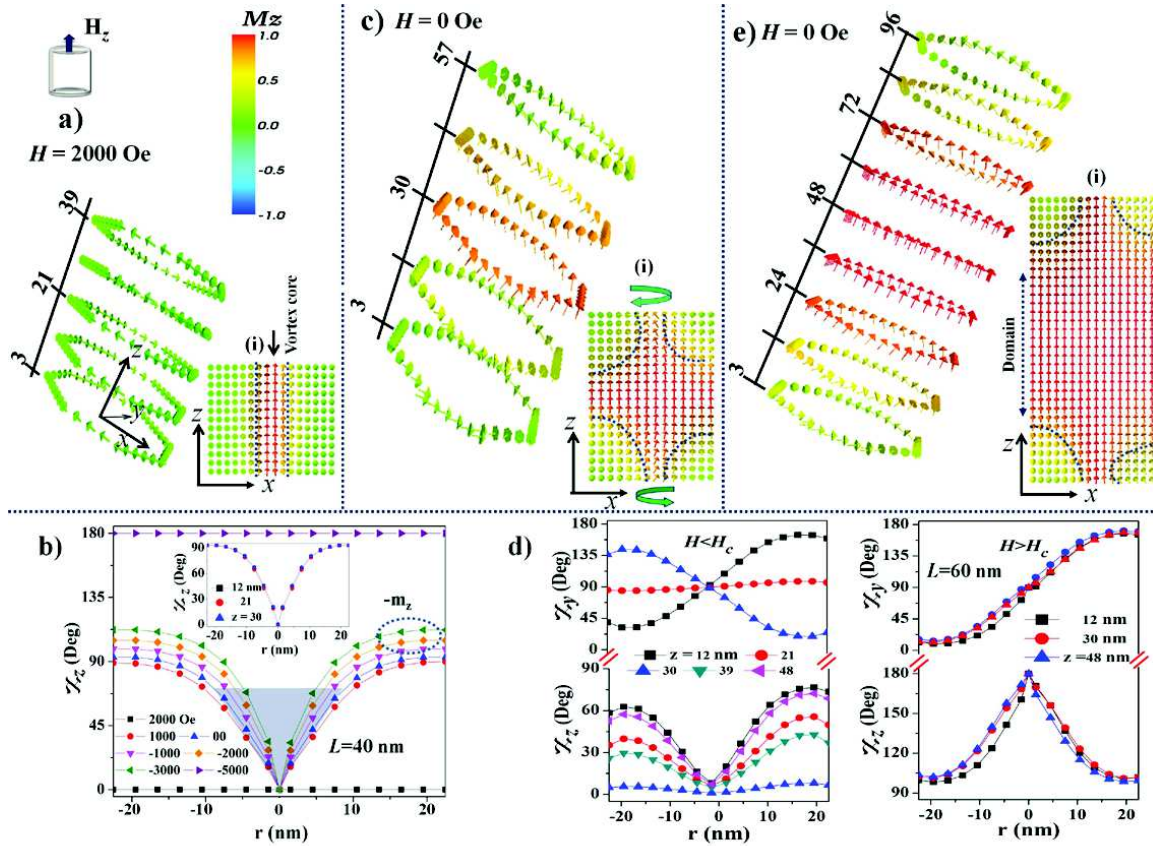


Figure 6.11: shows 3D view of z -component magnetic distribution as a function of nanorod length, a) for $L = 40$ nm at $H = H_n$, c) 60 nm at $H = 0$ Oe, and e) 100 nm at $H = 0$ Oe, respectively. The outer shell is only shown for better clarity of the image. The arrows schematically indicate the magnetization direction and the colors indicate the longitudinal magnetization, M_z . Inset (i) shows the 2D xz -plane at $y=0$, for a solid cylinder of the same rod. Dotted marked lines guided to eye for identifying the vortex core or the domain in the xz -plane. The external field applied here was parallel to the rod axis. The variation of χ_i vs r along the length of the rod in the xz plane with $y = 0$ (Here i represents y and z). (b) shows the values of χ_i , which were extracted for $L = 40$ nm at different field values and the inset shows the same for different z values at $H = H_n$. (d) shows the value of χ_i for different z values at fields of $H < H_c = 0$ Oe (left), and $H > H_c = -1200$ Oe, (right).

The reversal process for the former case is discussed above and the contribution in net m_z follows the similar procedure. In later case, for a set field, the intensity of vortices (i.e. the angular distribution of \mathbf{M} vector) decreases as it moves from top or bottom ends towards the center (~ 30 nm) and it diminishes at both sides of the domain wall having +ve m_z components as shown by variation of χ_z along the radial direction for different z values. However, with decreasing field till $H = H_c$ (see Fig. 6.11(d), left), the propagation of the vortex towards the center from both ends leads to reduce the width of the domain to minimum value along the z -direction. For $H > H_c$, the core spin flips to negative z -direction and the annihilation process starts in the whole nanorod through single vortex transition (Fig. 6.11(d), (right)).

For $L > 100$ nm, the reversal process begins at $H_n = 700$ Oe for L of 100 nm and -500 Oe for 200 nm, respectively. It forms two vortices at both the ends of the nanorod with a single domain state at the middle, as described above. It is to be noted that the size of this single domain state was increased to ~ 50 nm of the nanorod length, at $H = 0$, as depicted in Fig. 6.11(e) for $L = 100$ nm. This indicates the rod length determines the size of the domain, which arises from the increase in magneto-static interaction with respect to L , as described in our previous report (Sellarajan et al. 2013). Therefore, increase in net M_r^{\parallel} was observed as a function of L when the field is applied parallel to the nanorod axis, as shown in Fig. 6.9(d) and (e). However, for $L = 100$ nm, the spins of a nanorod in a hexagon seven nanorod array was flipped towards negative z axes near $H = H_c$.

For the field applied in parallel to nanorod axis, simulated $M(H)$ curves indicate an increase in M_r^{\parallel}/M_s as a function of rod length. This matches quite well with the values extracted from the experimentally measured $M(H)$ curves. In overall, with consideration of the shape of a nanorod, magnetostatic interaction among nanorods and magnetocrystalline anisotropies, the magnetization reversal process in Co nanorod arrays with fcc(111) structure were found to dominated by vortex structure and results in a crossover of the easy axis from in-plane to the out-of-plane direction in this system with a critical length of 77 nm. To reduce the discrepancy in the observed behavior of the $M(H)$ loops, one needs to consider the following factors: (i) increase in the number of nanorods (i.e., 10^8 for an area of 5×5 mm² as in real case) in an array while carrying the simulation, (ii) presence of imperfection within nanorods, especially for the shorter nanorods, and (iii) physical shape variations among the nanorods.

6.5 SIZE DEPENDENT STUDY ON MAGNETOSTATIC INTERACTION IN hcp (002) PHASE

From the experimental point of view, it should be remembered that Co nanowire arrays with hcp (002) crystalline structure were tailored by the synthesis process (i.e., pH (~ 6.7) of the electrolyte and deposition time). The quantification of the experimental result begins with the construction of the wire geometry (diameter, and inter-wire spacings) by using 3D OOMMF for seven hexagon array within the normalized area of $0.96 \times 0.78 \mu\text{m}^2$. In this case, two different I_p values were used and then each I_p values were identically modified with the use of two different wire diameters, as same as the experimental data (see Fig. 4.9 as discussed in section 4.5). It was shown by the earlier results that the magnetic properties of Co nanowires were sensitive with their crystalline phase, diameter, length. Therefore, in this case, the Co nanowire arrays were preferred to vary only with the inter-wire spacings by keeping these parameters constant, i.e., it has been achieved by tuning the pore diameters of porous AAO membrane with two different inter-pore distances as mentioned earlier in Chapter 4. During this investigation, the wire diameter was importantly controlled within the variation of two different I_p values; among this one of diameter in this two different I_p value has \sim same diameter (i.e., D_p of 50 nm in I_p of 66 nm and 105 nm, respectively). Importantly, for this case, the length (< 300 nm) of the nanowire has been controlled by the uniform deposition time that leads to exhibit the same demagnetization factor, i.e., the shape effect corresponds to $(D/L)^2$ see Eqn 4.3.2, and the corresponding Fig. 4.12 in Chapter 4. In principle, the above fabricated Co nanowires have been demonstrated for the variation of $M(H)$ loops which is significant with the magneto-static interaction between the nanowires arises from the neighboring wires.

3D-OOMMF package was used to perform the micromagnetic simulations for a 2D array of nanowires. Here, nanowires with variable diameters ($D_p=20-45$, and $50-80$ nm), and the inter-wire spacings ($I_p=65$ and 110 nm) were developed as same as the experimental results, shown in Fig. 4.10. For Co hcp (002) phase, the parameters were considered as: $A = 1.3 \times 10^{-11}$ J/m (the exchange constant), $M_s = 1.76$ T (the saturation magnetization), and $K = 4.5 \times 10^5$ J/m³ (the magneto-crystalline anisotropy constant) (Vivas et al. 2011). The direction of the easy axis in the hcp phase was considered to be parallel to the nanowire axis, i.e., hcp Co (002) phase. Here, the change in the magnetic properties of wires, i.e., the influence of the magnetostatic interaction between the arrays could be easily identified by the $M(H)$ loops when the field is applied parallel to the wire axis. Whereas, simulated results show the high anisotropic nature with zero remanent when the field is applied perpendicular to the wire axis for hcp Co (002)

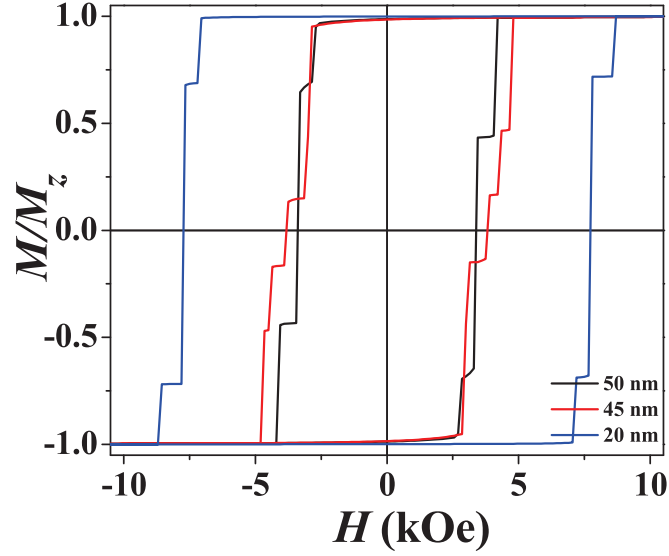


Figure 6.12: Simulated $M(H)$ loops for nanowires ordered in hexagonal array of seven nanowires with different diameters ($D_p = 25$ (65 nm), 45 (65 nm), and 50 nm (110 nm)), when the field is applied parallel to wire axis.

phase, i.e., it shows the hard magnetic axis. In addition to this, the negotiation of dipolar interaction was also reported for well-separated nanowires when the distance is larger than twice of its diameter. Therefore, we propose here to compare the static interaction between the wires with more or less dense of wires in 2D array by choosing two different I_p with the same diameter and a different diameter within the same I_p value. The system of variation with two different I_p in the same diameter has not been reported earlier for the magnetic behavior of magnetic Co nanowire arrays in both experimental or simulated, whereas, there were reports for different diameters within the I_p value. In this case, the magnetic properties of Co hcp (002) phase was investigated as a function of both diameter and inter-wire spacings in a 2D array of hexagonally ordered dense wires.

For an array of nanowires, the simulated results were mostly considered by the ordered arrangement of the hexagonal array of seven nanowires. Therefore, in this case, the magnetic properties of Co nanowires for different diameters and inter-wire spacings were simulated initially for an ordered array of hexagonally arranged seven nanowires. The simulated $M(H)$ loops were shown in Fig. 6.12 for nanowires of seven hexagon array with different diameters ($D_p = 25$ (65 nm), 45 (65 nm), and 50 nm (110 nm)), when the external field is applied parallel to the wire axis. The remanent state derived from this figure shows an alignment of the corresponding magnetic moments is oriented along a z axis. However, the switching field or the nucleation field is varied with respect to wire diameter. This indicates that irrespective of the I_p , the value of H_c is increased

while decreasing the diameter of the wire in the array. It is a well known fact that the coercive force will be enhanced for a smaller size than the larger particle size due to the coherent nature of the magnetic domain characteristics as a nanosize effect. Whereas, the interaction between the nanowire arrays should lead to influence the magnetization reversal processes, which are not identified in the current situation. Due to unveil the effect of inter-wire separation in the dipole-dipole interaction of magnetostatic interactions in arrays of nanowires, we had modified the structure of the array geometry to limit within the normalized area of $0.9 \times 0.8 \mu m^2$. Therefore, the arrangement of ordering within the area was approximately 7×9 no. of nanowires for I_p of 110 nm, which is equivalent to 15×13 no. of nanowires in I_p of 65 nm spacings. In fact, this suggests considering for less and more dense of nanowires within the same area (i.e., $0.96 \times 0.78 \mu m^2$), as suggested by the mean field theory with the inclusion of P in Eqns. 1.2.1 and 1.2.2, where P is the filling factor. Therefore, It is also expected that the increase in P , either by enlarge the diameter within the cell size or by decreasing the cell size for the same pore diameter of the alumina membrane, will decrease the M_r/M_s in arrays of nanowires.

The expected observations are made in other reports which available for Fe, Ni, and even for Co nanowire arrays with polycrystalline nature (Cheng-Zhang et al. 1990, Martin et al. 2003, Vázquez et al. 2004, Kartopu et al. 2008, Sánchez-Barriga et al. 2009). Moreover, the theoretical simulations have also been demonstrated by using the mean field theory using Monte-Carlo simulations for Ni nanowires (Vázquez et al 2004) and for Co nanowires without considering the magnetocrystalline anisotropy, term using Nmag micromagnetic modeling package (Zighem et al. 2011). Therefore, the important of this study is crucial to point out that here, we demonstrate the magnetostatic interaction between the nanowire arrays of hcp Co (002) crystalline phase as influenced by the filling factor (P) using 3D OOMMF package.

6.5.1 Effect of inter-wire spacing

For large (small) inter-wire separation, the magnetic properties of the above mentioned geometries are easily analyzed as one can neglect (interrogate) the dipole-dipole coupling between the nanowires. Figure 6.13 show the $M(H)$ loops of the four different geometry with two different I_p values, i.e., the variable diameters are a) 25 (65) nm, b) 45 (65) nm, c) 50 (110) nm and d) 80 (110) nm, respectively. It is clear that the observed hysteresis curve has no change in the behavior for seven hexagons or for large dense wires (15×13 for Fig. 6.13(a) and 7×9 in Fig. 6.13 (c)), as indicates the large separation between the nanowires due to the smaller diameter in the particular cell structure of the alumina membrane leads to having less impact on the dipole interaction between

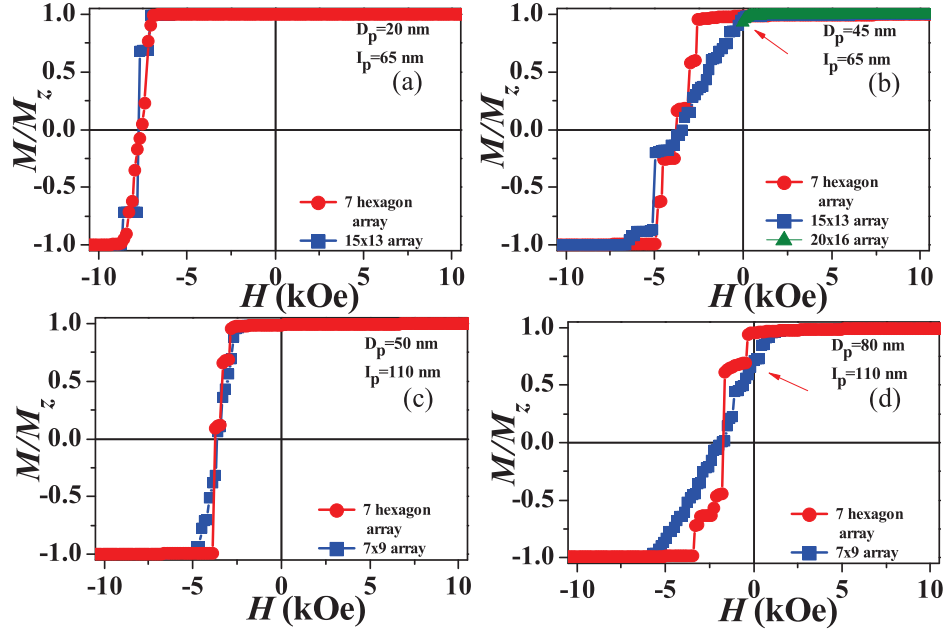


Figure 6.13: Simulated $M(H)$ loops of Co nanowires for four different geometry with two different I_p values, i.e., the variable diameters are: a) 25 (65) nm, b) 45 (65) nm, c) 50 (110) nm, and d) 80 (110) nm, when the field is applied parallel to wire axis. The NWs are ordered in hexagonal array of normalized area ($0.96 \times 0.78 \mu\text{m}^2$) that results two different wire densities in a array, i.e., 15×13 for I_p of 65 nm and 7×9 for 105 nm, respectively.

them. Whereas, for the case of larger diameter which intern reduce the inter-wire separation, which leads to showing different switching field in the array of nanowires with the large dense array in Fig. 6.13 (b and d). The switching field distribution in the array of the nanowires can be explained by using the Eqn. 6.3.3, as explained for hcp (002) structure. This reduction in the switching field distribution leads to reduce the M_r/M_s in the dense wires with less separation, as observed in our experimental results (see Fig. 4.12), as indicated with an arrow mark in Fig. 6.13 (b and d). However, the value of H_c is observed to be no change in the seven and dense arrays, which indicates that the value of H_c depends on the diameter of the nanowire and independent to the inter-wire separation and filling factor. The extracted magnetic parameters are tabulated and compared with our experimental data, in table 6.2.

6.5.2 Effect of filling factor in array of nanowires

While comparing the extracted magnetic parameters, if one can assume the D_p of 45 and 50 nm are approximately equal in geometry except the filling factor (i.e., two different

Table 6.2: Magnetic parameters of Co nanorods with hcp (002) phase.

Interwire separation (nm)	Diameter (nm)	Experimental			Simulated		Remarks
		H_c^{\parallel} (Oe)	H_c^{\perp} (Oe)	M_r^{\parallel}/M_s	H_c^{\parallel} (Oe)	M_r^{\parallel}/M_s	dipole interaction
65	25	2500	600	0.9	7500	1	×
	45	2240	300	0.68	3400	0.96	✓
110	50	2110	400	0.86	3600	1	×
	80	1500	250	0.41	1700	0.85	✓

density of the nanowires due to the variation in the inter-wire spacings). Then, this will lead to observe the magnetostatic interaction between the less and denser of the hcp Co (002) nanowires of the same diameter. As shown in Fig. 6.13 (b and c), the value of H_c is approximately equal in both the case, whereas, the squareness ratio (M_r/M_s) is gradually decreasing with increase in density of the nanowires in the array. For example, the array of 20×16 no. of wires show a further reduction in the M_r/M_s in Fig. 6.13 (b) (see arrow indication).

6.6 SUMMARY

- These simulations allow us to define magnetic states at different length segments of a nanowire having different crystallographic structures. Our results show that the dipolar interaction among the shorter nanowires with hcp (002) phase enhances the magnetostatic energy in the system. This magnetostatic energy reduces substantially for longer ones with the presence of hcp(100) phase as the anisotropy energy dominates in this segment. Therefore, the key to control both the shape of $M(H)$ curve and coercivity of the nanowires is to control the crystallographic orientation of easy axis together with the length segment ratio.
- We have investigated the evolution of magnetic properties of Co NWs associated with the formation of different phases along the NW axis at different length scales. In shorter wire length with hcp (002) structure, the reversal occurs via coherent process; whereas in longer one consisting of both hcp (002) and hcp (100) structure, a gradual crossover from a coherent state at lower segment to vortex state at upper segment was observed. It was also shown that in an array with hcp (002) structure, the dipole interactions among them effectively reduce the coercivity in the system by 50%. Moreover, with the addition of small percentage (15%) of hcp (100) structure at the top of the NW, the magnetostatic energy

arising due to dipolar interaction decreases dramatically, which in turn reduces H_c by 50%, keeping squareness ratio almost one. This might be due to initiation of the vortex state at one end of the NW. With further the addition of hcp (100) structure, the anisotropy field (H_K) was found to decrease, indicating a decrease in the uniaxial anisotropy in the system. Thus, by controlling the formation of different phases of hcp (002) and (100) along the Co NW length, it is possible to control the magnetic properties, such as H_c , squareness ratio, and magnetic anisotropy. Therefore, this study is very important to understand the physics of magnetic states towards the memory applications where the magnetic array with higher effective longitudinal anisotropy, lower H_c , and reduced interaction are required.

- For small diameter with fcc Co (111) phase, we have investigated the magnetic properties of Co nanorod array keeping the aspect ratio just below and above the unity. In this case, the experimental observation on the crossover of their easy axis of magnetization in Co nanorod arrays at a critical length, L_c , was well explained while considering the shape, magnetocrystalline anisotropies and magnetostatic interaction among nanorods. The origin of the discrepancy in L_c between analytical and simulated data was found to be due to the complicated nature of reversal magnetization processes as the rod length grow.
- The effect of magnetostatic interaction was also investigated in Co nanowire arrays with hcp (002) phase. During the investigation, the D_p of nanowire arrays were kept constant ~ 50 nm with two different density of the nanowires (i.e., due to the variation in the inter-wire spacings). Therefore, uniform mean field theory was an aid to provide the static influence within the normalized area for less and denser of nanowires with the same diameter. Magnetization loop indicates that no variation in the value of H_c , whereas, the squareness ratio (M_r/M_s) is gradually decreasing with increase in density of the nanowires in the arrays due to the static interaction.

Chapter 7

CONCLUSIONS

From the present study, it can be concluded that:

- The crystallographic structure of electrodeposited Co NW is highly dependent on the NW diameter, length, and the pH of the solution at a particular temperature.
- The electrodeposited Co NWs found to be phase sensitive to the diameter (D), such as textured growth of fcc Co (111) phase was observed for $D = 45$ nm, and hcp Co (002) phase for $D = 70$ nm, in pulse dc mode. However, above the critical length the transition of hcp (100) phase was observed to modify the longitudinal magnetic anisotropy in Co NW arrays. In addition to this, Co NWs at 70 nm diameter are found to be independent with pH of the electrolyte in pulse deposition process, i.e., the crystalline phase of Co are not influenced by the electrolyte pH. Whereas, the resultant change in the crystalline phases from hcp (100) to hcp (002) was observed for increasing the electrolyte pH (i.e., from 2 to 6.7) in continuous dc deposition.
- In hcp Co (002) phase, the highly uniaxial magnetic anisotropy was obtained with coherent magnetization reversal process in NW arrays, independent to NW length. Whereas the presence of hcp (100) structure in longer NWs shows a gradual crossover from a coherent state at lower segment to vortex state at upper segment, which in turn reduces H_c and squareness ratio. Therefore, controlling the bilayer lengths of hcp (002) and (100) in Co NWs found to decrease the anisotropy field (H_k), indicating a decrease in uniaxial anisotropy in the system.
- For fcc Co nanorods, keeping the aspect ratio just below and above the unity shows the crossover in their easy magnetization axis at a critical length, L_c , which is almost two times higher than its diameter. This is unexpected as the analytical formula derived based on the shape anisotropy and the magneto-static interaction among the nanorods yields L_c value of the order of its diameter. With consideration of shape, magnetocrystalline anisotropies and magnetostatic interaction among nanorods, micromagnetic simulation explained this crossover. The origin of this large L_c was found to be due to the complicated nature of reversal magnetization processes as the rod length grows.

- The influence of magnetostatic interaction in hcp Co (002) phase describe the importance of the filling factor of the NWs in the arrays, which results in a reduction in the squareness ratio.
- Surface patterning of Co nanodot arrays indicate in-plane magnetization with vortex formation.

7.1 FUTURE DIRECTIONS

Till now, our effort is to study the physics behind the remagnetization mechanism of magnetic Co nanostructures, which is prepared via electrodeposition or sputtering techniques through the pores of the mild-anodized AAO membrane. In this series, we have studied the importance of magnetocrystalline anisotropy and the magnetostatic interactions between the neighboring nanowires along with the shape anisotropy in arrays of Co NSs. The complexity of the remagnetization mechanism could be minimized while considering the same crystalline orientation or the removal of the magnetostatic interaction by keeping the NSs far away in nanoarrays. In view of this, recent anodization of Al is focused on the emerging area of hard-anodization (HA) processes. This process leads to varying the inter-pore distances of the neighboring pores in a wider range from nm to μm intervals as a function of the applied potentials. While, introduction of HA-AAO membrane may help to effectively reduce the magnetostatic interaction in arrays of magnetic NS, which will allow to investigate the domain wall propagation of single NS through magnetic switching or *current induced switching* of NS for their potential applications in various sensors and spintronic. The unique feature of the spin-polarized current induced domain-wall switching is called spin torque effect for the development of ultra-high-density magnetic memory device with low power consumption. Furthermore, the series of this work may include understanding the magnetic transport mechanism of multilayered nanowire arrays in the potential use of current perpendicular to plane-Giant Magnetoresistance (*CPP-GMR*) for high-density magnetic recording media or reading head applications. In addition to this, the spin transfer torque can switch the direction of magnetization in multilayer pillars, in which, it is possible to push the domain wall (boundary of two different magnetic domains with different magnetization directions) along the length of the nanowire. These observations may provide the basic understanding of the new type of domain wall based data storage device called *racetrack memory device* for ultra high-density magnetic media.

References

- Aerts, T. Dimogerontakis, Th. Graeve, I. De Fransaer, J. Terryn, H. (2007). "Influence of the anodizing temperature on the porosity and the mechanical properties of the porous anodic oxide film". *Surf. Coat. Technol.*, 201, 7310.
- Ahmad, N. Chen, J. Y. Iqbal, J. Wang, W. X. Zhou, W. P. and Han, X. F. (2011). "Temperature dependent magnetic properties of Co nanowires and nanotubes prepared by electrodeposition method". *J. Appl. Phys.*, 109, 07A331.
- Allen J. Bard, Gyorgy Inzelt, Fritz Scholz (Eds) (2008). "Electrochemical Dictionary", *Springer*, Chapter "Chronoamperometry", volume 95-96.
- Armyanov, S., (2000). "Crystallographic structure and magnetic properties of electrodeposited cobalt and cobalt alloys", *Electrochim. Acta*, 45, 3323-3335.
- Arora, S. K. ODowd, B. J. Ballesteros, B. Gambardella, P. and Shvets, I. V., (2012). "Magnetic properties of planar nanowire arrays of Co fabricated on oxidized step-bunched silicon templates", *Nanotechnology*, 23, 235702.
- Belwalkar, A. Grasing, E. Geertruyden, W. V. Huang, Z. Misiolak, W.Z. (2008). "Effect of Processing Parameters on Pore Structure and Thickness of Anodic Aluminum Oxide (AAO) Tubular Membranes". *J Memb. Sci.*, 319, 192.
- Bing, C. W. Gui, H. M. Hao, Z. Yu, O. and Jiang, D. L. (2010). "Micromagnetic simulation on the dynamic susceptibility spectra of cobalt nanowires arrays: the effect of magnetostatic interaction". *Chin. Phys. B*, 19(8), 087502.
- Brown W. F. Jr., (1978). "Micromagnetics". *Krieger*, New York, 1978.
- Cao, H. Wang, L. Qiu, Y. Wu, Q. Wang, G. Zhang, L. Liu, X. (2006). "Generation and Growth Mechanism of Metal (Fe, Co, Ni) Nanotube Arrays". *ChemPhysChem*, 7, 1500.
- Cavallotti, P. L. Galbiati, E. and Chen, T. Snyder, D. D. Landau, U. and Sard,

R. (1983). "ECS", NJ, 130.

Chang-Peng Li, Roshchin, Igor. V. Battle, X. Viret, M. Ott, F. and Schuller, Ivan. K. (2006). "Fabrication and structural characterization of highly ordered sub-100 nm planar magnetic nanodot arrays over 1 cm² coverage area". *J. Appl. Phys.*, 100, 074318.

Cheng-Zhang, L. and Lodder, J. C. (1990). "The influence of the packing density on the magnetic behaviour of aluminate media". *J. Magn. Magn. Mater.*, 88, 236-246.

Chung, S. H. McMichael, R. D. Pierce, D. T. and Unguris, J. (2010). "Phase diagram of magnetic nanodisks measured by scanning electron microscopy with polarization analysis". *Phy. Rev. B.*, 81, 024410.

Pletcher, D. Montenegro, M.I. Queiros, M.A. Daschbach, J.L. (Eds.) (1991). "Microelectrodes: Theory and Applications". *Kluwer Academic Publishers*, Dordrecht, 1991.

Darques, M. Encinas, A. Vila, L. and Piraux, L. (2004). "Tailoring of the c-axis orientation and magnetic anisotropy in electrodeposited Co nanowires". *J. Phys.: Condens. Matter*, 16, S2279.

Donahue M. J., and Porter D. G. (2012). "OOMMF User's Guide Version 1.0", Interagency report NISTIR 6376. *National Institute of Standards and Technology*, Gaithersburg, MD., <http://math.nist.gov/oommf/>.

Encinas-Oropesa, A. Demand, M. Piraux, L. Huynen, I. and Ebels, U. (2001). "Dipolar interactions in arrays of nickel nanowires studied by ferromagnetic resonance". *Phys. Rev. B*, 63, 104415.

Engel-Herbert, R. Hesjedal, T. Mohanty, J. Schaadt, D. M. and Ploog, K. H. (2006). "Magnetization reversal in MnAs films: Magnetic force microscopy, squid magnetometry, and micromagnetic simulations". *Phys. Rev. B*, 73, 104441.

Escrig, J. Altbir, D. Jaafar, M. Navas, D. Asenjo, A. and Vázquez, M. (2007). "Remanence of Ni nanowire arrays: influence of size and labyrinth magnetic

structure". *Phys. Rev. B*, 75, 184429.

Escrig, J. Bachmann, J. Jing, J. Daub, M. Altbir, D. and Nielsch, K. (2008). "Crossover between two different magnetization reversal modes in arrays of iron oxide nanotubes". *Phys. Rev. B*, 77, 214421.

Escrig, J. Daub, M. Landeros, P. Nielsch, K. and Altbir, D. (2007). "Angular dependence of coercivity in magnetic nanotubes". *Nanotechnology*, 18, 445706.

Franklin, A. D. Maschmann, M. R. DaSilva, M. Janes, D. B. Fisher, T. S. and Sands, T. D. (2007). "In-place fabrication of nanowire electrode arrays for vertical nanoelectronics on Si substrates". *J. Vac. Sci. Technol. B*, 25(2), 343-347.

Gao, X. Liu, L. Birajdar, B. Ziese, M. Lee, W. Alexe, M. and Hesse, D., (2009). "High-Density Periodically Ordered Magnetic Cobalt Ferrite Nanodot Arrays by Template-Assisted Pulsed Laser Deposition", *Adv. Funct. Mater.*, 19, 3450-3455.

García, J. M. Asenjo, A. Velázquez, J. García, D. Vázquez, M. Aranda, P. and Ruiz-Hitzky, E. (1999). "Magnetic behavior of an array of cobalt nanowires". *J. Appl. Phys.*, 85, 5480.

Goolaup, S. Singh, S. Adeyeye, A.O. Ng, V. and Jalil, M. B. A. (2005). "Transition from coherent rotation to curling mode reversal process in ferromagnetic nanowires". *Eur. Phys. J. B*, 44, 259264.

Han, G. C. Zong, B. Y. and Wu, Y. H. (2002). "Magnetic Properties of Magnetic Nanowire Arrays". *IEEE Trans. Magn.*, 38(5), 2562.

Han, G. C. Zong, B. Y. Luo, P. and Wu, Y. H. (2003). "Angular dependence of the coercivity and remanence of ferromagnetic nanowire arrays". *J. Appl. Phys.*, 93, 9202.

Han, X. F. Shamaila, S. and Sharif, R. (2010). "Electrodeposited Nanowires and their Applications". *InTech*, 2010. ISBN 978-953-7619-88-6.

Han, X. Y. Shen, W. Z. (2011) "Improved two-step anodization technique for ordered porous anodic aluminum membranes". *J. Electroanal. Chem.* 655 56.

Han, X. Liu, Q. Wang, J. Li, S. Ren, Y. Liu, R. and Li, F. (2009). "Influence of crystal orientation on magnetic properties of hcp Co nanowire arrays". *J. Phys. D: Appl. Phys.*, 42, 095005.

Harrison, R. J. and Feinberg, J. M. (2008). "FORCinel: An improved algorithm for calculating first-order reversal curve distributions using locally weighted regression smoothing". *Geochem. Geophys. Geosyst.*, 9, Q05016.

Henry, Y. Ounadjela, K. Piraux, L. Dubois, S. George, J. M. and Duvail, J. L. (2001). "Magnetic anisotropy and domain patterns in electrodeposited cobalt nanowires". *Eur. Phys. J. B*, 20, 35.

Hwang, S. K. Jeong, S. H. Hwang, H. Y. Lee, O. J. and Lee, K. H. (2002). "Fabrication of Highly Ordered Pore Array in Anodic Aluminm Oxide". *Korean J. Chem. Eng.*, 19(3), 467.

Jamet, M. Dupuis, V. Mélinon, P. Guiraud, G. and Pérez, A. (2000). "Structure and magnetism of well defined cobalt nanoparticles embedded in a niobium matrix", *Phys. Rev. B*, 62, 493.

Jeong, S.Y. An, M.C. Cho, Y.S. Kim, D.J. Paek, M. C. Kang, K. Y., (2009). "Preparation of anodic aluminum oxide templates on silicon substrates for growth of ordered nano-dot arrays", *Current Applied Physics*, 9, S101-S103.

Jessensky, O. Müller, F. and Gösele, U. (1998). "Self-organized formation of hexagonal pore arrays in anodic alumina". *Appl. Phys. Lett.*, 72, 1173.

Kartopu, G. Yalçın, O. Es-Souni, M. and Básaran, A. C. (2008). "Magnetization behavior of ordered and high density Co nanowire arrays with varying aspect ratio". *J. Appl. Phys.*, 103, 093915.

Keller, F. Hunter, M. S. and Robinson, D. L. (1953). "Structural Features of Oxide Coatings on Aluminum". *J. Electrochem. Soc.*, 100, 411-419.

Kim, C. Loedding, T. Jang, S. Zeng, H. Li, Z. Sui, Y. and Sellmyer, D. J. (2007). "FePt nanodot arrays with perpendicular easy axis, large coercivity, and extremely high density". *App. Phy. Lett.*, 91, 172508.

Kouklin, N. A. and Liang, J., (2006) "Ultradense GaN Nanopillar and Nanopore Arrays by Self-Assembly Nanopatterning", *Journal of Electronic Materials*, 35, 5, 1133.

Kulkarni, P. D. Sellarajan, B. Krishnan, M. Harish, C. Barshilia. and Chowdhury, P. (2013). "Anisotropic magnetic properties of bi-layered structure of ordered Co nanowire array: Micromagnetic simulations and experiments". *J. Appl. Phys.*, 114, 173905.

Landeros, P. Allende, S. Escrig, J. Salcedo, E. Altbir, D. and Vogel, E. E. (2007). "Reversal modes in magnetic nanotubes". *Appl. Phys. Lett.*, 90, 102501.

Lavin, R. Denardin, J. C. Escrig, J. Altbir, D. Cortès, A. and Gómez, H. (2009). "Angular dependence of magnetic properties in Ni nanowire arrays". *J. Appl. Phys.*, 106, 103903.

Lee, W. and Park, S. J. (2014). "Porous Anodic Aluminum Oxide: Anodization and Templated Synthesis of Functional Nanostructures". *Chem. Rev.*, 114(15), 7487-7556.

Lei, Y. and Chim, W. K. (2005). "Shape and Size Control of Regularly Arrayed Nanodots Fabricated Using Ultrathin Alumina Masks". *Chem. Mater.*, 17, 580.

Lei, Y. Cai, W. and Wilde, G. (2007). "Highly ordered nanostructures with tunable size, shape and properties: A new way to surface nano-patterning using ultra-thin alumina masks". *Prog. Mater. Sci.*, 52, 465.

Li, A. P. Muller, F. Birner, A. Nielsch, K. Gösele, U. (1999). "Polycrystalline nanopore arrays with hexagonal ordering on aluminum". *J. Vac. Sci. Technol. A*, 17, 1428.

Li, A.P. Müller, F. and Gösele, U. (2000). "Polycrystalline and monocrystalline pore arrays with large interpore distance in anodic alumina". *Electrochem. Solid-State Lett.*, 3, 131-134.

Li, A.P. Müller, F. Birner, A. Nielsch, K. and Gösele, U. (1998). "Hexagonal

pore arrays with a 50-420 interpore distance formed by self-organization in anodic alumina". *J. Appl. Phys.*, 84, 6023-6026.

Li, D. Thompson, Richard. S. Bergmann, G. and Lu, J. G. (2008). "Template-based Synthesis and Magnetic Properties of Cobalt Nanotube Arrays". *Adv. Mater.*, 20, 4575-4578.

Li, F. Zhang, L. and Metzger, R. M. (1998). "On the Growth of Highly Ordered Pores in Anodized Aluminum Oxide". *Chem. Mater.*, 10, 2470-2480.

Li, Y. Zheng, M. Li Ma and Shen, W. (2006). "Fabrication of highly ordered nanoporous alumina films by stable high-field anodization". *Nanotechnology*, 17, 5101-5105.

Lillo, M. Losic, D. (2009). "Pore opening detection for controlled dissolution of barrier oxide layer and fabrication of nanoporous alumina with through-hole morphology". *Journal of Membrane Science*, 327, 11-17.

López, J. M. Altbir, D. Romero, A. H. Batlle, X. Roshchin, Igor. V. Li, C. P. and Schuller, Ivan. K. (2006). "Vortex state and effect of anisotropy in sub-100 nm magnetic nanodots". *J. Appl. Phys.*, 100, 104319.

Maaz, K. Karim, S. Usman, M. Mumtaz, A. Liu, J. Duan, J. L. Maqbool, M. (2010). "Effect of Crystallographic Texture on Magnetic Characteristics of Cobalt Nanowires". *Nanoscale Res. Lett.*, 5, 1111-1117.

Martin, J. I. Nogues, J. Liu, K. Vicent, J. L. Schuller, Ivan. K. (2003). "Ordered magnetic nanostructures: fabrication and properties". *J. Magm. Magn. Mater.*, 256, 449501.

Martínez-Huerta, J. M. J De La Torre Medina, J. Piraux, L. and Encinas, A. (2013). "Configuration dependent demagnetizing field in assemblies of interacting magnetic particles". *J. Phys.: Condens. Matter*, 25, 226003.

Masuda , H. Matsui, Y. Yotsuya, M. Matsumoto, F. and Nishio, K. (2004). "Fabrication of Highly Ordered Anodic Porous Alumina Using Self-organized Polystyrene Particle Array". *Chemi. Lett.*, 33(5), 584.

Masuda, H. and Fukuda, K. (1995). "Ordered Metal Nanohole Arrays Made by a Two-Step Replication of Honeycomb Structures of Anodic Alumina". *Science*, 268, 1466.

Masuda, H. Hasegawa, F. and Ono, S. (1997). "Self-Ordering of Cell Arrangement of Anodic Porous Alumina Formed in Sulfuric Acid Solution". *J. Electrochem. Soc.*, 144, L127.

Masuda, H. Kanezawa, K. and Nishio, K. (2002). "Fabrication of ideally ordered nanohole arrays in anodic porous alumina based on nanoindentation using scanning probe microscope". *Chem. Lett.*, 12, 1218.

Masuda, H. Yada, K. and Osaka, A. (1998). "Self-Ordering of Cell Configuration of Anodic Porous Alumina with Large-Size Pores in Phosphoric Acid Solution". *Jpn. J. Appl. Phys.*, 37, L1340.

Masuda, H. Yamada, H. Satoh, M. Asoh, H. Nakao, M. Tamamura, T. (1997). "Highly ordered nanochannel-array architecture in anodic alumina". *Appl. Phys. Lett.*, 71, 2770.

Newell, A. J (2005). "A high-precision model of first order reversal curve (FORC) functions for single domain ferromagnets with uniaxial anisotropy". *Geochem. Geophys. Geosyst.*, 9, Q05010.

Spaldin N. A. (ed.) (2011). "Magnetic Materials Fundamentals and Applications". "Cambridge University Press", second edition.

Nielsch, K. Choi, J. Schwirn, K. Wehrspohn, Ralf B. and Gosele, U. (2002). "Self-ordering regimes of porous alumina: the 10 porosity rule". *Nano Lett.*, 2(7), 677.

Ono, S. and Masuko, N. (2003). "Evaluation of pore diameter of anodic porous films formed on aluminum". *Surf. Coat. Technol.*, 169, 139-142.

Ono, S. Saito, M. Ishiguro and M. Asoh, H. (2004). "Controlling Factor of Self-Ordering of Anodic Porous Alumina". *J Electrochem. Soc.*, 151(8), B473.

Ouchi, K. Honda, N. (2010). "Electrochemical Nanotechnologies, Number 113-129 in Nanostructure Science and Technology". *Springer* New York, 2010, Part II edition. ISBN 978-1-4419-1423-1.

Pan, H. Liu, B. Yi, J. Poh, C. Lim, S. Ding, J. Feng, Y. Huan, C. H. A. and Lin, J. (2005). "Growth of Single-Crystalline Ni and Co Nanowires via Electrochemical Deposition and Their Magnetic Properties". *J. Phys. Chem. B*, 109, 3094.

Pirota, K. R. Béron, F. Zanchet, D. Rocha, T. C. R. Navas, D. Torrejón, J. Vázquez, M. and Knobel, M. (2011). "Magnetic and structural properties of fcc/hcp bi-crystalline multilayer Co nanowire arrays prepared by controlled electroplating". *J. Appl. Phys.*, 109, 083919.

Ren, Y. Wang, J. Liu, Q. Dai, Y. Zhang, B. and Yan, L. (2011). "Tailoring coercivity and magnetic anisotropy of Co nanowire arrays by microstructure". *J. Mater. Sci.*, 46, 7545.

Roberts, A. P. Pike, C. R. and Verosub, K. L. (2000). "First-order reversal curve diagrams: A new tool for characterizing the magnetic properties of natural samples". *J. Geophys. Res.*, 105, 28461.

Sánchez-Barriga, J. Lucas, M. Radu, F. Martin, E. Multigner, M. Marin, P. Hernando, A. and Rivero, G. (2009). "Interplay between the magnetic anisotropy contributions of cobalt nanowires". *Phys. Rev. B*, 80, 184424.

Schlorb, H. Haehnel, V. Khatri, M.S. Srivastav, A. Kumar, A. Schultz, L. and Fahler, S. (2010). "Magnetic nanowires by electrodeposition within templates". *Phys. Status Solidi B*, 247(10), 2364-2379.

Scholz, W. Guslienko, K. Y. Novosad, V. Suess, D. Schrefl, T. Chantrell, R. W. Fidler, J. (2003). "Transition from single-domain to vortex state in soft magnetic cylindrical nanodots". *J. Magn. Magn. Mater.* 266, 155.

Sellarajan, B. Kulkarni, P. D. Krishnan, M. Harish, C. Barshilia. and Chowdhury, P. (2013). "Magnetic properties of ordered bi-layer nanowire arrays with different Co crystallographic structures". *Appl. Phys. Lett.*, 102, 122401.

Srivastava, A.K. Singh, R.S. Sampson, K.E. Singh, V.P. and Ramanujan, R.V. (2007). "Templated Assembly of Magnetic Cobalt Nanowire Arrays". *The Minerals, Metals and Materials Society and ASM International*, 38, 717.

Stoner, E. C. and Wohlfarth, E. P. (1948). "A Mechanism of Magnetic Hysteresis in Heterogeneous Alloys". *Phil. Trans. R. Soc. A*, 240, 599.

Strijkers, G. J. Dalderop, J. H. J. Broeksteeg, M. A. A. Swagten, H. J. M. and de Jonge, W. J. M. (1999). "Structure and magnetization of arrays of electrodeposited Co wires in anodic alumina". *J. Appl. Phys.*, 86(9), 5141.

Su, Z. Bühl, M. and Zhou, W., (2009). "Dissociation of Water During Formation of Anodic Aluminum Oxide". *J. Am. Chem. Soc.*, 131, (24), 8697-8702.

Sulka, G. D. (2008). "Nanostructured Materials in Electrochemistry". WILEYVCH, 2008. ISBN 978-3-527-31876-6.

Sulka, G. D. Stroobants, S. Moshchalkov, V. Borghs, G. Celis, J. P. (2002). "Synthesis of Well-Ordered Nanopores by Anodizing Aluminum Foils in Sulfuric Acid". *J. Electrochem. Soc.*, 149, D97-D103.

Sulka, G. D. Wojciech and Stepniowski, J. (2009). "Structural features of self-organized nanopore arrays formed by anodization of aluminum in oxalic acid at relatively high temperatures". *Electrochim. Acta*, 54, 3683-3691.

Valizadeh, S. George, J. M. Leisner, P. Hultman, L. (2001). "Electrochemical deposition of Co nanowire arrays; quantitative consideration of concentration profiles". *Electrochim. Acta*, 47, 865-874.

Vázquez, M. Nielsch, K. Vargas, P. Velázquez, J. Navas, D. Pirola, K. Vélez, M. H. Vogele, E. Cartese, J. Wehrspohn, R. B. Gösele, U. (2004). "Modelling hysteresis of interacting nanowires arrays". *Physica B*, 343, 395402.

Vázquez, M. Pirola, K. Torrejón, J. Navas, D. Hernández-Vélez, M., (2005). "Magnetic behaviour of densely packed hexagonal arrays of Ni nanowires: Influence of geometric characteristics". *J. Magn. Mater.*, 294, 174-181.

Vivas, L. G. Escrig, J. Trabada, D. G. Badini-Confalonieri, G. A. and Vázquez, M. (2012). "Magnetic anisotropy in ordered textured Co nanowires". *Appl. Phys. Lett.*, 100, 252405.

Vivas, L. G. Ivanov, Y. P. Trabada, D. G. Proenca, M. P. Chubykalo-Fesenko, O. and Vázquez, M. (2013). "Magnetic properties of Co nanopillar arrays prepared from alumina templates". *Nanotechnology*, 24, 105703.

Vivas, L. G. Vázquez, M. Escrig, J. Allende, S. Altbir, D. Leitao, D.C. and Araujo, J. P. (2012). "Magnetic anisotropy in CoNi nanowire arrays: Analytical calculations and experiments". *Phys. Rev. B*, 85, 035439.

Vivas, L. G. Vázquez, M. Vega, V. Garcia, J. Rosa, W. O. del Real, R. P. and Prida, V. M. (2012). "Temperature dependent magnetization in Co-base nanowire arrays: Role of crystalline anisotropy". *J. Appl. Phys.*, 111, 07A325.

Vivas, L. G. Yanes, R. Chubykalo-Fesenko, O. and Vázquez, M. (2011). "Coercivity of ordered arrays of magnetic Co nanowires with controlled variable lengths". *Appl. Phys. Lett.*, 98, 232507.

Wang, X. W. Fei, G. T. Tong, P. Xu, X. J. Zhang, L. D. (2007). "Structural control and magnetic properties of electrodeposited Co nanowires". *J. Cryst. Growth*, 300, 421.

WSxM, *Nanotec Electronica SL*, Spain,, <http://www.nanotec.es>.

Wu, M. Wen, L. Lei, Y. Ostendorp, S. Chen, S. and Wilde, G., (2010). "Ultrathin Alumina Membranes for Surface Nanopatterning in Fabricating Quantum-Sized Nanodots". *Small*, 6,(5), 695-699.

Xu, J. Huang, X. Xie, G. Fang, Y. Liu, D. (2005). "Fabrication and magnetic property of monocrystalline cobalt nanowire array by direct current electrodeposition". *Mater. Lett.*, 59, 981-984.

Yang, S. G. Zhu, H. Ni, G. Yu, D. L. Tang, S. L. and Du, Y. W. (2000). "A study of cobalt nanowire arrays". *J. Phys. D: Appl. Phys.*, 33, 23882390.

Yang, Y. Chen, Y. Wu, Y. Chen, X. and Kong, M. (2010). "Diameter Controllable Magnetic Properties of Co Nanowire Arrays by Pulsed Electrodeposition". *Journal of Nanomaterials*, 793854.

Ye, Z. Liu, H. Luo, Z. Lee, H. G. Wu, W. (2009). "Changes in the crystalline structure of electroplated Co nanowires induced by small template pore size". *J. Appl. Phys.*, 105, 07E126.

Yin, A. J. Li, J. Jian, W. Bennett, A. J. and Xu, J. M. (2001). "Fabrication of highly ordered metallic nanowire arrays by electrodeposition". *Appl. Phys. Lett.*, 79(7), 1039-1041.

Zhang, J. Grenville, A. Jones. Tiehan, H. Shen. and Steve, E Donnelly. and Li, G. (2007). "Monocrystalline hexagonal-close-packed and polycrystalline face-centered-cubic Co nanowire arrays fabricated by pulse dc electrodeposition". *J. Appl. Phys.*, 101, 054310.

Zhu, X. F Song, Y. Liu, L. Wang, C. Y. Zheng, J. Jia, H. B. and Wang, X. L. (2009). "Electronic currents and the formation of nanopores in porous anodic alumina". *Nanotechnology*, 20, 475303.

Zighem, F. Maurer, T. Ott, F. and Chaboussant, G (2011). "Dipolar interactions in arrays of ferromagnetic nanowires: a micromagnetic study". *J. Appl. Phys.*, 109, 013910.

Zou, M. Wang, H. Larson, P. R. Hobbs, K. L. Johnson, M. B. and Awitor, O. K., (2009). "Ni nanodot-patterned surfaces for adhesion and friction reduction". *Tribology Letters*, 24(2), 137-142.

PUBLICATION DETAILS:

Published in Peer Review Journals:

- **Sellarajan, B.** Kulkarni, P. D. Nagaraja, H. S. Harish C. Barshilia, and Chowdhury, P. (2016) "Size dependent magnetic properties of Co nanorod arrays prepared by pulse deposition" *J. Synth. React. Inorg. Met.-Org. Chem.* (submitted).
- **Sellarajan, B.** Megha Sharma, Ghosh, S. K. Nagaraja, H. S. Harish C. Barshilia and Chowdhury, P. (2016) "Effect of Temperature on The Formation of Highly Ordered Nanoporous Alumina Template", *Microporous Mesoporous Mater.* 224, 262.
- **Sellarajan, B.** Nagaraja, H. S. Harish C. Barshilia and Chowdhury, P. "Effect of shape and magnetocrystalline anisotropies in ordered Co nanorod array with smaller pore diameter", *J. Magn. Magn. Mater.* 404, 197.
- **Sellarajan, B.** Kulkarni, P. D. Krishnan, M. Harish C. Barshilia, and Chowdhury, P. (2013), "Magnetic properties of ordered bi-layer nanowire arrays with different Co crystallographic structures", *Appl. Phys. Lett.* 102, 122401.
- Kulkarni, P. D. **Sellarajan, B.** Krishnan, M. Harish C. Barshilia, and Chowdhury, P. (2013), "Anisotropic magnetic properties of bi-layered structure of ordered Co nanowire array: Micromagnetic simulations and experiments", *J. Appl. Phys.* 114, 173905.

CONFERENCES ATTENDED:

- **Sellarajan, B.** P. D. Kulkarni, H. S. Nagaraja, Harish C. Barshilia, and P. Chowdhury, "Size dependent magnetic properties of Co nanorod arrays prepared by pulse deposition", *International Conference on Nanomaterials and Nanotechnology (NANO15)* will be held at K.S.R College of Technology, Tiruchengode on 7-10, December 2015 (oral presented).
- **Sellarajan, B.** P. D. Kulkarni, M. Krishnan, H. S. Nagaraja, Harish C. Barshilia, and P. Chowdhury, "Effective magneto-crystalline anisotropy in ordered Co nanowire array", *IUMRS ICA 2013* held at IISc, Bangalore during 16-20, December 2013 (poster presented).

VITA



Boominathasellarajan S.

Dept. of Phys. PhD cand.

rayarajan2005@gmail.com

Mobile: +91 99766 21390

Personal Information

Date of Birth 05 June 1984
Place of Birth Melachokkanathapuram, Theni, Tamilnadu, India
Marital Status Married
Nationality Indian

Experience

May 2012- Senior Research Fellow (CSIR), Surface Engineering Division,
 May 2015 National Aerospace Laboratories (CSIR), Bangalore, India.
Sep. 2011- Project Assistant, Surface Engineering Division,
 May 2012 National Aerospace Laboratories (CSIR), Bangalore, India.
Aug. 2010- Project Post Graduate Trainee, Surface Engineering Division,
 Aug. 2011 National Aerospace Laboratories (CSIR), Bangalore, India.
Sep. 2007- Lecturer, Dept. of Physics, Bharath Niketan Engineering College
 July 2008 (Affiliated to Anna University), Aundipatty, Tamilnadu, India.
Nov. 2006- PG Assistant in Physics, Sree Vaijayanthee Vidyalaya Matriculation
 May 2007 Higher Secondary School, Srirangam, Tamilnadu, India.

Education

2016 Doctor of Philosophy in Physics
 National Institute of Technology Karnataka, Surathkal, India.
2010 Master of Technology in Nanotechnology
 Vellore Institute of Technology University, Vellore, India.
2007 Master of Philosophy in Physics
 Bharathidasan University (DDE), Tiruchirapalli, India.
2006 Master of Science in Physics
 Madurai Kamaraj University, Madurai, India.
2004 Bachelor of Science in Physics
 Madurai Kamaraj University, Madurai, India.

Area of Research Interest

- Template-assisted growth of multi-segment magnetic nanostructures, thermoelectric nanoarrays, and application of optical switching,
- Magnetoresistance (GMR & AMR & TMR) based Spintronics,
- Spin-valve materials,
- Nanoscale PVD multilayer coatings,
- Carbon Nanotubes and Graphene,
- Nano-dimensional magnetic thin films and sensors,
- Electro-chemistry,
- Super-capacitor and its applications.

Other Publications

- Chowdhury, P. **Sellarajan, B.** Krishnan, M. Raghuvaran, K. Harish C. Barshilia, and Rajam, K. S. (2012), "In Situ Electrochemical Thinning of Barrier Oxide Layer of Porous Anodic Alumina Template", *Adv. Sci. Lett.* 4, 253.
- Chowdhury, P. **Sellarajan, B.** Krishnan, M. Harish C. Barshilia, (2012), "Fabrication of magnetic nanodot arrays using ultrathin alumina membrane (UTAM)", *Solid State Physics: Proceedings of the 56th DAE Solid State Physics Symposium 2011. AIP Conference Proceedings*, 1447, 357-358.
- Balaji, J. **Sellarajan, B.** Sasikala, N. T. and Bala praveen chakkavarthy, R. (2011), "Electrophoretic Deposition Of ZnO Nanorods and Nanoparticles", *Int. J. Nanosci.* 10, 787.
- Sasikala, N. T. **Sellarajan, B.** Bala Praveen Chakkavarthy, R. (2011), "Fabrication of Nanostructures using Porous Anodic Alumina (AAO) Template", *Int. J. Nanosci.* 10, 783.

Languages

Tamil	Native	Kannada	Limited working proficiency
English	Full professional proficiency	German	Entry level